Sensitivity Analysis for Dark Matter Indirect Detection with SWGO

José Ignacio Rivadeneira Rojas

Science Faculty
Physics Department
Universidad Católica del Norte, Chile
February 2025

Sensitivity Analysis for Dark Matter Indirect Detection with SWGO

José Ignacio Rivadeneira Rojas

Thesis submitted as a partial requirement for the degree of:
Master of Science (MSc), mention in Physics

Advisor:
Dr. Roberto Lineros
Physics Department
Science Faculty
Universidad Católica del Norte

Co-Advisor:
Dr. Sebastian Tapia
Physics Department
Universidad Técnica Federico Santa María

Evaluation Committee:
Dr. Cesar Bonilla
Universidad Católica del Norte
Dr. Andreas Reisenegger
Universidad Metropolitana de Ciencias de la Educación
Dr. Alessio Porcelli
Universidad de Antofagasta

Universidad Católica del Norte
Science Faculty
Physics Department
February 2025

‘Preoccupied with a single leaf... you won’t see the tree. Preoccupied with a single tree... you’ll miss the entire forest. Don’t be preoccupied with a single spot. See everything in it’s entirety... effortlessly. That is what it means to truly see.’

Takuan Sōhō

Acknowledgements

I thank my family, who have always given me their unconditional support throughout this journey, especially during its most challenging moments. I am also grateful to my friends, classmates, and everyone I have met during these years of study, especially to everyone on the 5th floor, with whom I have shared wonderful experiences that made this stage truly special.

I extend my deep gratitude to my professors, especially to my advisors, Dr. Roberto Lineros and Dr. Sebastian Tapia, for their invaluable help, dedication, and willingness, always offering support with a smile and a positive attitude. Their knowledge was of great importance to me in carrying out this research.

Lastly, I would like to express my gratitude to every member of the SWGO collaboration, who provided a helping hand while navigating through the (quite abstract) required libraries and packages used in this investigation.

Abstract

Given its high **Dark Matter** (DM) content and relative proximity, the **Galactic Center** region is expected to be the brightest **source of gamma rays** from DM annihilation or decay in the sky by several orders of magnitude with respect to other regions of the sky.

In this context, gamma-ray observatories are particularly promising for the search for DM at masses above ~ 1 TeV, due to their high sensitivity and sufficient angular resolution.

The Southern Wide-field Gamma-ray Observatory (SWGO) stands out as an ideal platform for detecting gamma-ray signals from dark matter, especially in astrophysically observed regions of high dark matter density. SWGO's large field of view, combined with its excellent location in the **Atacama Desert**, will enable a robust search for consistent dark matter signals from multiple classes of sources across the sky, including extended emissions such as the decay or annihilation of dark matter particles in the galactic halo.

This work presents a sensitivity study based on **simulations of particle showers** generated by gamma rays and protons using the SWGO detector design, aiming to evaluate the future effectiveness of such an observatory in detecting Dark Matter signals from the Galactic Center. For this purpose, simulations of the showers generated in the atmosphere were performed using the CORSIKA package, with initial particle properties obtained from DM gamma-ray spectra previously simulated for all annihilation channels using the Pythia Event Generator. Subsequent simulations of the detector response to the particles generated by these showers were carried out using Geant4-based software.

The necessary curves to estimate the effectiveness of this detector in reconstructing the initial properties of the incident particles were obtained, the **Instrument Response Functions (IRF)**, which are a set of functions used to compare expected and observed gamma-ray showers and background (protons or another hadron) showers, and to estimate the gamma-ray detection sensitivity of this detector. These IRF's includes curves such as the **Effective Area**, **Angular Resolution**, **Energy Resolution and Bias**, **Background Rejection** or **Proton Efficiency** and the **Sensitivity** of the detector array to the simulated DM gamma-ray flux. Finally, preliminary **sensitivity estimates and constraints** were found for different **annihilation channels** at several **DM masses**.

Resumen

Dada su alta concentración de **Materia Oscura** (DM) y su relativa proximidad, se espera que la región del **Centro Galáctico** sea la fuente más brillante de **rayos gamma** producidos por la aniquilación o decaimiento de DM en el cielo, superando a otras regiones por varios órdenes de magnitud.

En este contexto, los observatorios de rayos gamma son especialmente prometedores para la búsqueda de DM con masas superiores a 1 TeV, debido a su alta sensibilidad y resolución angular adecuada.

El Southern Wide-field Gamma-ray Observatory (SWGO) se destaca como una plataforma ideal para la detección de señales de rayos gamma provenientes de la materia oscura, especialmente en regiones astrofísicamente observadas con alta densidad de DM. Su amplio campo de visión, combinado con su excelente ubicación en el **Desierto de Atacama**, permitirá una búsqueda robusta de señales consistentes de materia oscura en diversas clases de fuentes celestes, incluidas emisiones extendidas como el decaimiento o aniquilación de partículas de DM en el halo galáctico.

Este trabajo presenta un estudio de sensibilidad basado en **simulaciones de lluvias de partículas** generadas por rayos gamma y protones, utilizando el diseño del detector SWGO, con el objetivo de evaluar la efectividad futura de este observatorio en la detección de señales de Materia Oscura provenientes desde el Centro Galáctico. Para ello, se realizaron simulaciones de lluvias en la atmósfera con el paquete CORSIKA, donde las propiedades de las partículas generadoras de estas lluvias fueron obtenidas a partir de espectros de rayos gamma de DM previamente simulados para todos los canales de aniquilación mediante el generador de eventos Pythia. Posteriormente, se llevaron a cabo simulaciones de la respuesta del detector a las partículas generadas en estas lluvias utilizando software basado en Geant4.

Se obtuvieron las curvas necesarias para evaluar la capacidad del detector en la reconstrucción de las propiedades iniciales de las partículas incidentes, las **Instrument Response Functions (IRF)**, un conjunto de funciones utilizadas para comparar las lluvias de rayos gamma esperadas y observadas, así como las lluvias de fondo (protones u otros hadrones), con el fin de estimar la sensibilidad del detector a la detección de rayos gamma. Estas IRF incluyen curvas como el **Área Efectiva**, la **Resolución Angular**, la **Resolución y Sesgo de Energía**, la **Eliminación del ruido de Fondo** o **Eficiencia para Protones**, y la **Sensibilidad** del arreglo de detectores al flujo simulado de rayos gamma de DM. Finalmente, se obtuvieron **estimaciones preliminares de sensibilidad y restricciones** para diferentes **canales de aniquilación** en varias **masas de DM**.

Contents

1 Introduction

The nature of Dark Matter is one of the fundamental questions in modern physics. Numerous observations, from galaxy rotation curves [1] to fluctuations in the cosmic microwave background [2], provide strong evidence for the existence of DM. However, its fundamental nature remains unknown and, despite extensive search efforts, no direct signal has been detected yet. Among the most promising candidates are Weakly Interacting Massive Particles (WIMPs), non-baryonic particles with masses in the GeV-TeV range and interaction strengths at the weak scale.

The search of WIMPs has been extensively done by different experiments based on direct detection via nuclear recoil [3; 4; 5] and also by collider experiments through missing transverse momentum [6; 7; 8].

If DM particles have masses well above the TeV scale, astrophysical observations may provide the only viable discovery avenue in the near future. These particles would lie beyond the mass range accessible via production in terrestrial particle colliders and would have number densities too low for direct detection searches. These indirect detection mechanisms would look at the stable products of the DM annihilation or decay. To measure these known products, Cherenkov Radiation emerges as a promising tool to tackle this challenge, as it can be used to detect gamma-rays associated with possible dark matter interactions. This would provide valuable insights into its properties and characteristics. There exists several experiments already looking at these mechanisms [9; 10; 11].

For this reason, a gamma-ray observatory in the TeV scale, with a sufficiently wide field of view is a promising approach for detecting highly extended, low-surface brightness emissions associated with the DM halo of our galaxy. There are several of these experiments already in operation in the Northern Hemisphere, in particular LHAASO [12] and HAWC [13], utilizing arrays of particle detectors at high-altitude sites.

A similar facility in the Southern Hemisphere would offer high sensitivity to DM gamma-ray signals from the Galactic Center region, particularly due to the location of the GC near the zenith of such a detector.

In this work, we evaluate the sensitivity of the Southern Wide-field Gamma-ray Observatory (SWGO), a future gamma-ray observatory to be built in the Atacama Desert, Chile. We investigate the potential capabilities of this observatory to detect a Dark Matter (DM) signal originating from the Galactic Center (GC).

To achieve this, Extensive Air Showers (EAS) were simulated using a previously processed DM gamma-ray spectrum, followed by Monte Carlo simulations of the detector response, considering the latest detector configuration proposed by the SWGO collaboration. Performance curves for the detector were obtained, leading to sensitivity limits for DM particle annihilation in the Galactic halo.

This document is structured as follows:

First, we introduce gamma-ray astronomy, including the necessary definitions to understand the behavior and properties of Extensive Air Showers produced in Earth's atmosphere, along with the fundamental principles used for their detection. This includes a description of gamma-ray fluxes generated by dark matter particles in the Galactic Center.

Next, we provide an overview of SWGO, detailing the detector design used in our simulations, along with a brief review of the reconstruction strategies adopted by the collaboration to recover the properties of the primary particle responsible for the shower.

Following this, we present a step-by-step review of the simulation process leading to the generation of Instrument Response Functions (IRFs), which characterize the detector's performance. We also describe the methodology used to construct the DM gamma-ray spectrum employed in the simulations.

Finally, in Chapter 6, we analyze the detector's performance, comparing our results with the latest preliminary findings presented by SWGO. This is followed by a discussion on the sensitivity limits and constraints derived for DM cross-sections across multiple annihilation channels.

2 Gamma-ray Astronomy

In the observable universe, violent astrophysical phenomena give rise to the emission of highly energetic radiation, such as **gamma rays**. These gamma rays, originating from various stellar and interstellar scenarios, span energies ranging from Mega-electronvolts (MeV) to, according to the latest research, a few Peta-electronvolts (PeV) [14]. Alongside gamma radiation, these events also produce other forms of cosmic radiation and neutrinos collectively known as **cosmic rays**. Cosmic rays include protons, electrons, and heavy atomic nuclei, among other particles.

The discovery of cosmic rays dates back to 1912, when Viktor Hess first observed them [15]. This groundbreaking discovery led to the establishment of numerous experiments aimed at studying the cosmic radiation that reaches Earth. These observations culminated in the definition of the *all-particle cosmic ray energy spectrum*, as shown in **Figure 2.1**:

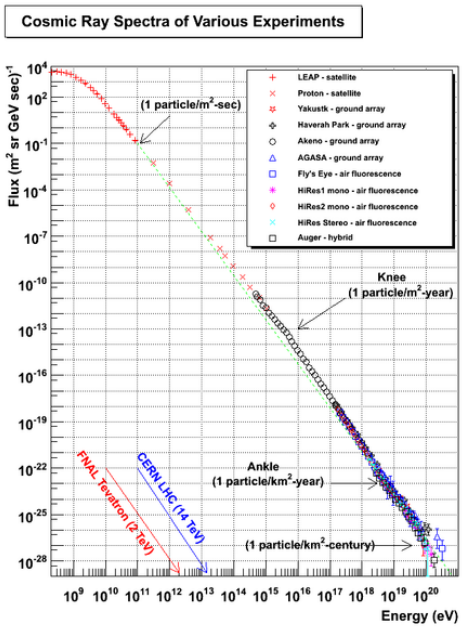

Figure 2.1 – Cosmic Ray Energy Spectrum compiled from multiple ground-based and satellite experiments. Key features of the spectrum, such as the 'knee' ($\sim 10^{15}$ eV) and the 'ankle' ($\sim 10^{18}$ eV), are marked. For comparison, the energy scales of Tevatron (7 TeV) and LHC (14 TeV) are also indicated. Taken from [16].

This spectrum reveals that the (differential) flux of particles reaching Earth approximately follows a power-law behavior of $\approx E^{-\alpha}$, where $\alpha \approx 2{,}7$ [17]. The x-axis spans many orders of magnitude in energy, extending up to the EeV scale.

A closer examination of the spectrum shows that at lower energies (< GeV), the flux appears nearly flat due to the shielding effect of Earth's magnetic field. Around an energy of 3 PeV, the spectrum features a characteristic ''knee'', beyond which the slope steepens. This energy range is widely believed to correspond to cosmic rays that originate from within our galaxy. At even higher energies, around 3 EeV, another distinct feature appears, known as the ''ankle'', further deviating from a simple power law.

At energies exceeding 10^{15} eV, the flux of cosmic rays becomes so low—falling below one particle per square meter per year—that direct measurements are no longer feasible. At these extreme energies, cosmic rays are detected indirectly through the cascades of secondary particles they produce in the atmosphere, known as **Extensive Air Showers** (EAS).

Understanding the origins of these characteristic features in the cosmic-ray flux is crucial for identifying their galactic and extragalactic sources, as well as the acceleration and propagation mechanisms these particles undergo.

The field of gamma-ray astronomy emerged in the 1950s, prompted by predictions of diffuse gamma-ray emission arising from the decay of π^0-mesons generated in cosmic ray interactions with the interstellar medium [18]. The first experiments in this field were space-based, beginning with the satellite Explorer XI, which successfully detected 22 extraterrestrial gamma rays [19]. These satellite instruments operate in the energy range of approximately 20 MeV to 300 GeV. However, their limited detection area poses a significant drawback. For example, the Fermi Large Area Telescope (LAT), consisting of 16 tracker modules, has a combined detection area of less than 1 m^2 [20], making it unsuitable for exploring the highest energy gamma rays.

In recent decades, significant advancements have been made in the exploration of the gamma-ray sky at Very High Energies (VHE; ∼100 GeV - ∼100 TeV). Photons in this energy range are detected indirectly from the ground by observing the particle cascades they produce in the atmosphere. However, since all cosmic rays produce EAS, they create a background that must be effectively discriminated from gamma-ray-induced showers. In order to begin with this discrimination, it is imperative to understand the principal differences between these particle cascades when they are originated by a gamma ray or a cosmic ray.

2.1 Extensive Air Showers

The Earth is constantly bombarded by various types of particles originating from activity in the Universe, such as cosmic rays and gamma rays. Cosmic rays are primarily composed of 90 % protons, 8 % helium nuclei, 1 % electrons, and a small fraction of heavier elements, such as carbon, oxygen and iron nuclei [17], while gamma rays are high-energy photons that can originate from different astrophysical sources, which will be reviewed with more detail in section 2.2. These particles reaching the Earth's atmosphere are called **primary particles**.

When a primary particle enters the atmosphere, it has a high probability of colliding with a nitrogen or oxygen nucleus, the main components of the atmosphere, during its journey. A collision occurs only if the interaction between the particle and the nucleus is sufficiently strong. The initial collision produces new particles, known as **secondary particles**, which have lower energy than the primary particle but are still highly energetic. These secondary particles can, in turn, collide with other atmospheric nuclei, generating further particles with even lower energies. This chain reaction results in large-scale cascades of particles, known as particle showers, which can be detected. The composition of these particle showers depends on the nature of the primary particle that initiated the process upon colliding with the atmosphere.

2.1.1 Electromagnetic Showers

The initial point in an atmospheric cascade, that is, the primary particle that generates the particle shower, can either be a photon or a charged particle. Charged particles, unlike photons, exhibit strong interactions with atomic nuclei present in the atmosphere. As a result, photons, on average, undergo their first collision at greater depths within the atmosphere, closer to the Earth's surface.

Photons interact with matter through the electromagnetic force. As a result, photons can only create particle-antiparticle pairs, primarily electrons and positrons. These particles, in turn, can produce new photons, for instance, when they move through the electric field of an atomic nucleus or when the positron annihilates upon encountering an electron.

The main constituents of showers initiated by gamma rays are photons, electrons, and positrons. These showers are therefore referred to as **Electromagnetic Showers**. Muons can also be found in these showers, but since the muon is approximately 200 times heavier than an electron, it requires significantly more energy to produce a $\mu^-\mu^-$ pair than is needed to produce an e^-e^+ pair.

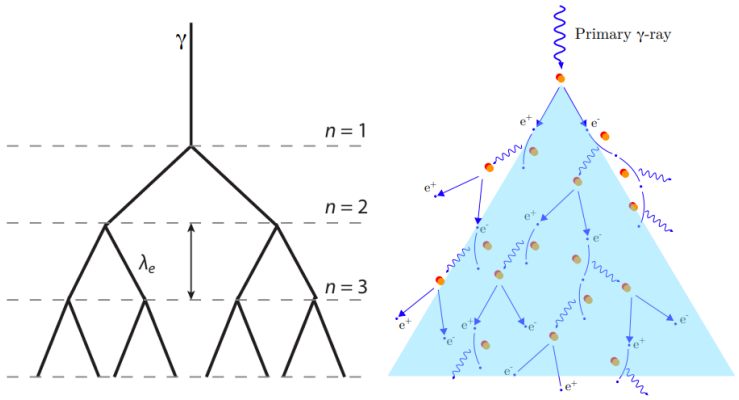

Figure 2.2 – Electromagnetic Shower Development: A high-energy gamma-ray initiates a particle shower, producing e^-e^+ pairs and secondary photons through successive interactions developing in new generations n of the shower. Adapted from [17].

The basic properties of electromagnetic showers are derived from the scale invariance of the dominant particle production processes: e^-e^+ pair production due to the presence of photons and bremsstrahlung, which produces photons due to the presence of e^-e^+ pairs [21]. However, electrons are subject to energy loss through ionization. This energy loss can be expressed as:

$$dE/dX = -\alpha(E) - E/X_0 \tag{2.1}$$

where $\alpha(E)$ is the ionization energy loss and X_0 is the radiation length in air ($X_0 \approx 37\text{gcm}^{-2}$).

The density of particles generated by an electromagnetic shower can be characterized as a function of its depth in the atmosphere, known as the **longitudinal profile**. Its basic properties can be studied using the Heitler model [22], a simple scaled approach. This model considers only one type of particle with energy E, where each interaction results in the creation of two new particles, each carrying energy $E/2$. These interactions occur after a particle has traversed a depth of λ_e (Figure 2.2). Denoting the number of generations in the shower as n, i.e., consecutive interactions. The number of particles at a given depth $X = n \cdot \lambda_e$ can be expressed as $N(X) = 2^n = 2^{X/\lambda_e}$, and the energy E of a particle in the n-th generation is determined as:

$$E(X) = \frac{E_0}{2^{X/\lambda_e}} \tag{2.2}$$

where E_0 represents the energy of the primary particle at $n = 0$. The particle multiplication process continues until energy losses due to ionization dominate over radiative losses (bremsstrahlung). This transition occurs at the critical energy E_c. The number of particles in the shower reaches its maximum when $E = E_c$, resulting in the following relationships:

$$N_{max} = \frac{E_0}{E_c} \quad \text{and} \quad X_{max}^{EM}(E_0) \sim \lambda_e \ln\left(\frac{E_0}{E_c}\right) \tag{2.3}$$

This means that the number of particles at the shower maximum is proportional to E_0, and the depth at which this occurs depends logarithmically on the energy of the primary particle. For example, for photon-induced showers one obtains [23]

$$\langle X_{max}^{(EM)} \rangle \approx X_0 \ln\left(\frac{E_0}{E_c}\right) + \frac{1}{2} \tag{2.4}$$

The spread of particles generated by the shower relative to its core is known as the **lateral profile**. In the case of electromagnetic showers, due to their nature, the lateral profile primarily depends on the Coulomb scattering caused by cascade electrons interacting with air atoms in the atmosphere. The scale of the lateral distribution for low-energy particles in a shower is characterized by the Molière unit, $r_1 = (21\text{MeV}/E_c)X_0 \approx 9{,}3\ \text{gcm}^{-2}$.

2.1.2 Hadronic Showers

Similar to electromagnetic showers, it is possible to formulate a set of equations for showers produced by hadrons. However, the complexity of multiple hadronic particle production, combined with the need to account for particle decays, prevents the derivation of analytical expressions for this type of showers. Nevertheless, some understanding of the characteristics of hadronic showers can be gained by generalizing the Heitler model, as demonstrated by James Matthews [24].

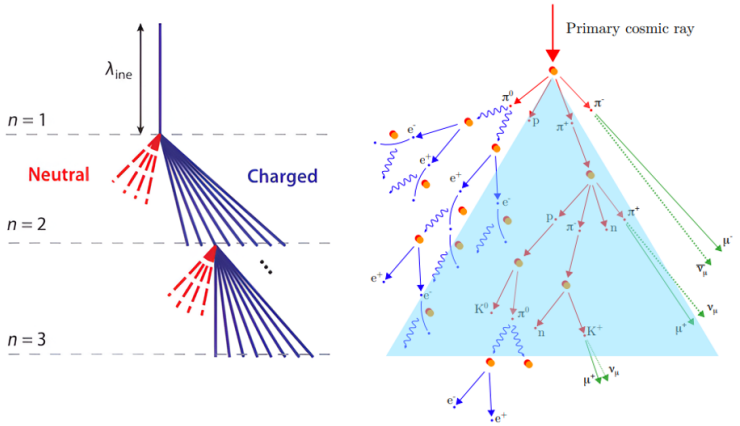

Figure 2.3 – Hadronic Shower Development: A primary cosmic ray interacts in the atmosphere, producing a cascade of secondary particles. The development of the shower through the atmosphere includes the production of hadrons, muons and electromagnetic sub-showers. Adapted from [17].

In this model, it is assumed that the interaction of a hadron with energy E will produce $n_{\rm tot}$ new particles, each with energy $E/n_{\rm tot}$. Of these, 2/3 will be charged particles ($n_{\rm ch}$), corresponding to charged pions, and 1/3 will be neutral particles, specifically neutral pions. The neutral particles decay immediately into electromagnetic particles ($\pi^0 \to 2\gamma$), while the charged particles, after traveling a distance corresponding to the mean interaction length $\lambda_{\rm int}$, interact again with the atmospheric nuclei, generating new particle cascades, as illustrated in Figure 2.3. Once the energy of the charged hadrons falls below a certain decay threshold $E_{\rm dec}$, these particles decay, producing one muon per hadron.

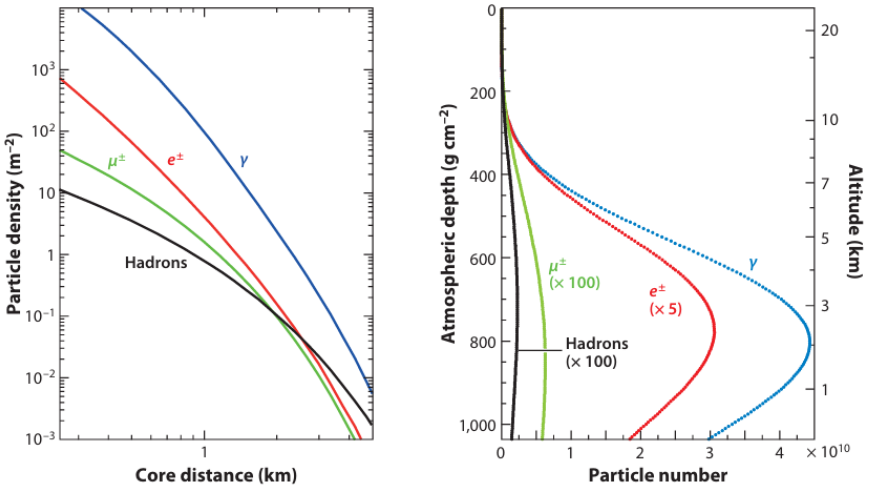

Figure 2.4 – Average (left) lateral distribution and (right) longitudinal profile for proton-induced showers at 10^{19}eV. Taken from [17].

In each hadronic interaction, one third of the energy is transferred via π^0 decay to the electromagnetic shower component. After n generations, the energies in the hadronic and electromagnetic components of the shower are given by, respectively

$$E_{\rm had} = \left(\frac{2}{3}\right)^n E_0 \quad \text{and} \quad E_{\rm EM} = \left[1 - \left(\frac{2}{3}\right)^n\right] E_0 \tag{2.5}$$

The depth of the shower maximum of a hadronic shower, i.e. its longitudinal profile (Figure 2.4), is determined by the electromagnetic particles that outnumber all the other contributions. Considering only the electromagnetic subshowers produced in the first hadronic interaction we can write

$$X_{\rm max}^{\rm (had)}(E_0) \approx \lambda_{\rm ine} + X_{\rm max}^{\rm (EM)}\left[\frac{E_0}{2n_{\rm tot}}\right] \sim \lambda_{\rm ine} + X_0 \ln\left(\frac{E_0}{2n_{\rm tot}E_c}\right) \tag{2.6}$$

where $\lambda_{\rm int} = \lambda_{\rm ine}$ is the hadronic interaction length.

The expression for the number of electrons at the shower maximum of a hadronic shower is the same as the one found before for the electromagnetic showers but with reduced energy. The number of muons in the Heitler-Matthews model follows from that of charged hadrons

$$E = \frac{E_0}{(n_{\rm tot})^n} = E_{\rm dec} \quad \text{and} \quad N_\mu = n_{\rm ch}^n \tag{2.7}$$

By eliminating the number of generations we get

$$N_\mu = \left(\frac{E_0}{E_{\text{dec}}}\right)^\alpha, \quad \text{where} \quad \alpha = \frac{\ln n_{\text{ch}}}{\ln n_{\text{tot}}} \approx 0{,}82 \ldots 0{,}94 \tag{2.8}$$

The number of muons generated by a hadronic shower depends on the energy of the primary particle, the atmospheric density (through E_{dec}), the multiplicity of charged particles and the total number of particles generated in the shower (through α).

The lateral profile of hadronic showers is broader compared to that of electromagnetic showers. Secondary hadrons produced in the cascade are generated with a typical transverse momentum (p_t) of approximately 350 - 400 MeV, which is almost independent of the primary particle's energy. This results in a wide angular distribution (with respect to the shower core) for low energy hadrons. Lastly, the lateral distribution of muons is even broader, as these muons are primarily produced in the decay of low energy pions, which are generated at later stages of the shower.

2.2 Gamma-ray Sources

Gamma rays are produced by some of the most violent phenomena in the Universe. Due to their high energies, they can travel vast distances before being detected on Earth. Since photons are electrically neutral, gamma rays are not influenced by magnetic fields along their path, allowing them to retain their original direction. As a result, detecting gamma rays provides valuable insights into the sources of these highly energetic particles.

The sources of gamma rays (and cosmic rays in general) can be divided in two categories:

- **Galactic Sources:** Found within our galaxy, of particular interest due to their proximity to Earth. Some of these sources include Supernova Remnants (SNR), Type Ia, Ib/c, or Type II. Shock waves in young SNR are promising candidates for the acceleration of cosmic rays up to the ''knee'' of the spectrum. After a type II supernova explosion, the remnant core can collapse into either a neutron star or a black hole, depending on the remaining mass. Neutron stars typically have masses between ∼1.2 and 2.5 solar masses [25]. Some neutron stars, known as pulsars, emit periodic radio pulses when their magnetic axis is misaligned with their rotation axis, producing a beam of particles and radiation that may periodically point towards Earth. The Crab, a pulsar, is one of the most studied objects in the sky, due to its high luminosity in the whole electromagnetic spectrum (Figure 2.5), has been used for decades as a calibration tool for different experiments [26], including gamma-ray observatories [27].

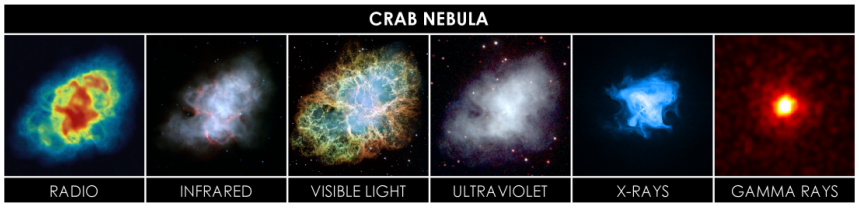

Figure 2.5 – The Crab Nebula seen in multiples wavelengths. Taken from [28].

The Galactic Center has a supermassive black hole, Sagittarius A, along with a high concentration of massive stars and other celestial bodies of interest which can be gamma-ray emitters. We will review this region in more detail in the next section, as it will be the central source region of gamma-rays for this work.

- **Extragalactic Sources:** These sources lie beyond the Milky Way and involve energies exceeding those of galactic phenomena. They include Active Galactic Nuclei (AGN)—such as blazars and quasars—alongside stellar and non-stellar black holes, extragalactic pulsars, galaxy clusters, gamma-ray bursts (GRBs), and other astrophysical objects [29].

2.2.1 Production Processes of Gamma Rays

This section briefly outlines some of the primary mechanisms responsible for gamma-ray production in the sources discussed above. These mechanisms include Synchrotron Radiation, Bremsstrahlung, Inverse Compton Scattering, and Neutral Pion Decay. Figure 2.6 illustrates an example of the spectral flux of gamma rays across different energy ranges, highlighting the typical energy domains where these production processes occur.

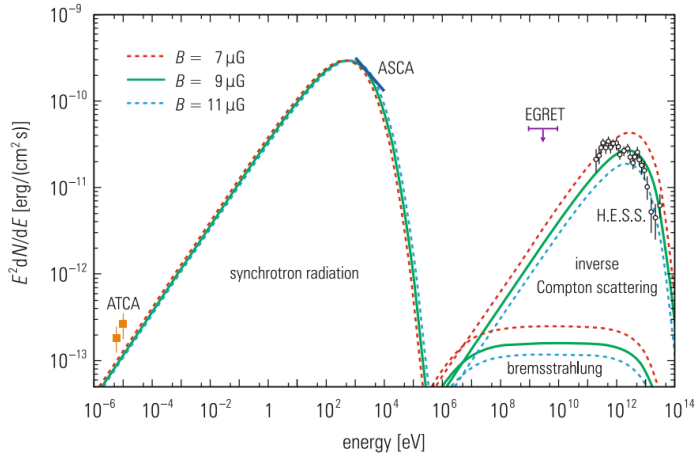

Figure 2.6 – Spectrum of photons with the contribution of different emission processes and measurements from different experiments. Taken from [30].

Synchrotron Radiation:

If a charged particle travels through a magnetic field in the direction of its field lines, it propagates in a spiral motion and undergoes acceleration. During this motion, the charged particle loses energy by emitting photons in the form of *synchrotron radiation* [30]. This type of radiation is predominantly produced by electrons interacting with cosmic magnetic fields. This process is depicted in Figure 2.7.

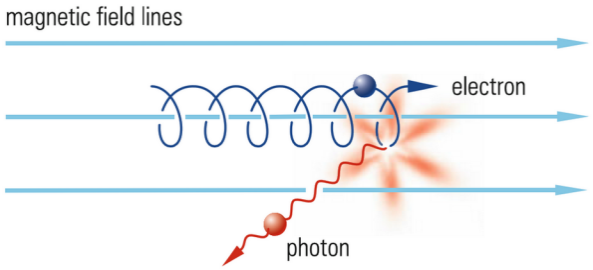

Figure 2.7 – Scheme of the production of synchrotron radiation by the deflection of an electron travelling in a magnetic field. Taken from [30].

The contribution of this process to the photon spectrum (Figure 2.6) lasts up to energies in the order of 10^5 eV.

Bremsstrahlung:

When a charged particle is deflected in the Coulomb field of a charge (atomic nucleus or electron), emits bremsstrahlung photons. This mechanism is to a certain extent similar to synchrotron radiation, only that in this case the deflection of the particle occurs in the Coulomb field of a charge rather than in a magnetic field.

For an electron, the energy that is lost after a certain distance can be calculated using [31]

$$\frac{\mathrm{d}E_e}{\mathrm{d}x} = \frac{4nZ^2\alpha^3(\hbar c)^2 E_e}{m_e^2 c^4} \cdot \ln\left(\frac{a(E)}{Z^{1/3}}\right) \tag{2.9}$$

where E_e is the kinetic energy of the electron, c is the speed of light, the number density of nuclei n, Z the charge of the atom which interacts with the electron and $\alpha = e^2/(4\pi\epsilon_0\hbar c)$ is the fine-structure constant. The parameter a takes into account the minimal distance between the electron and the atom necessary to still make deflection possible. As it is shown in Figure 2.6, the energy range in which the Bremsstrahlung contributes to the energy spectrum of the gamma rays stretches from around 10^6 eV to 10^{13} eV approximately.

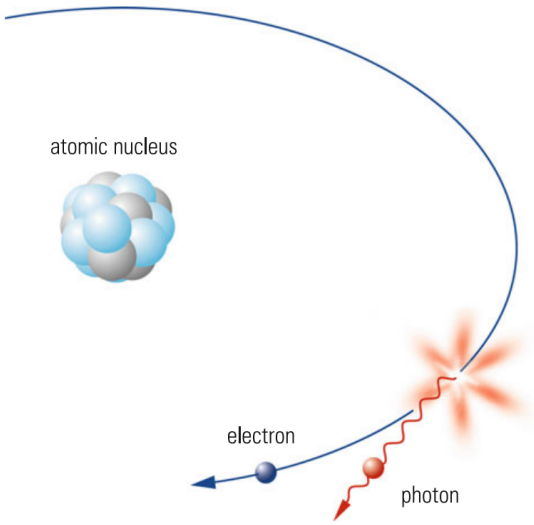

Figure 2.8 – Scheme of the production of bremsstrahlung by the deflection of an electron travelling in a electric field. Taken from [30].

Inverse Compton Scattering:

Electrons accelerated to high energies in the source collide with the numerous photons of the blackbody radiation, or with starlight photons, which are both low energy photons ($E_\gamma \approx 250$ µeV and $E_\gamma \approx 1$eV respectively). The electron transfers a part of its energy to the photon, resulting in a lower energy electron and a high energy photon. Inverse Compton scattering contributes to the gamma ray spectrum in an energy

range between 10^6eV and 10^{14}eV.

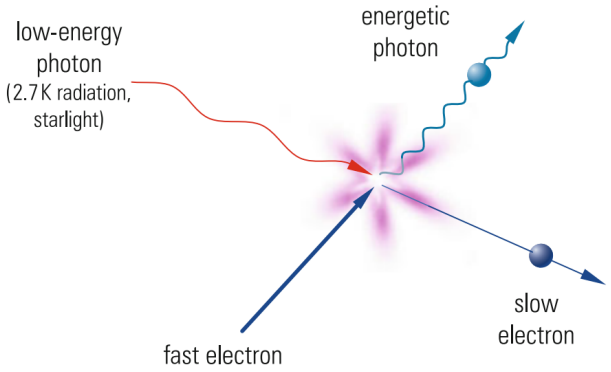

Figure 2.9 – Inverse Compton scattering of a low energy photon with a high energy electron. Taken from [30].

π^0 Decay:

The production of gamma rays is also possible through the eventual decay of neutral pions. Protons accelerated in the interstellar medium can produce charged π^{+-} and neutral pions π^0 (with equal probability) in proton-proton or proton-nucleus interactions (Figure 2.10). A possible process is

$$p + \text{nucleus} \rightarrow p' + \text{nucleus}' + \pi^0 + \pi^- + \pi^+ \tag{2.10}$$

and

$$\pi^0 \rightarrow \gamma + \gamma \tag{2.11}$$

If the neutral pion decays at rest, both photons are emitted back to back and with the same energy, which amounts to half of the rest mass of the pion $m_{\pi^0} = 135$ MeV [30]. In motion, the two gamma rays will have a different energy from each other that will be defined by the energy of the pion.

Matter-Antimatter Annihilation:

In the same way as photons can produce particle pairs, charged particles can annihilate with their antiparticles into energy. The dominant sources for this production mechanism are electron-positron and proton-antiproton annihilations

$$e^+ + e^- \rightarrow \gamma + \gamma \tag{2.12}$$

Momentum conservation requires the production of at least two photons. In e^-e^+ annihilation at rest, each photon gets 511 keV, corresponding to the rest mass of the electron/positron. In proton-antiproton annihilation, the resulting neutral pions decay into two photons, with their energy depending on the energy of the decaying pions.

$$p + \bar{p} \rightarrow \pi^+\pi^- + \pi^0 \tag{2.13}$$

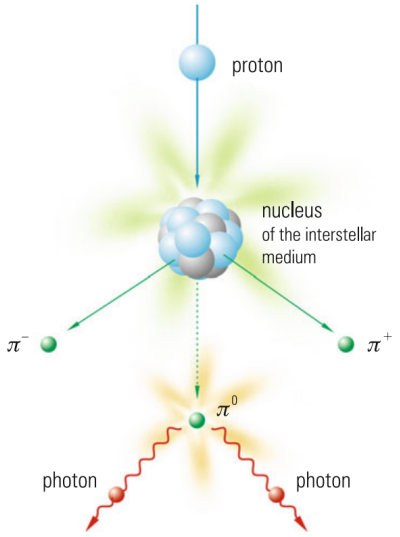

Figure 2.10 – Scheme showing the production of gamma rays through the decay of neutral pions. Taken from [30].

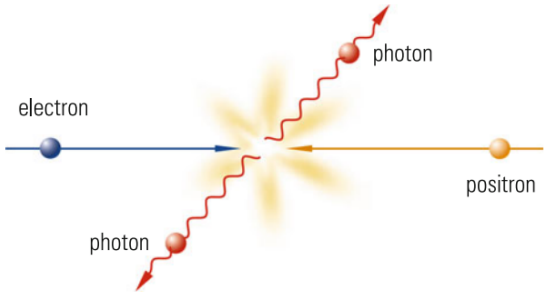

Figure 2.11 – Production of gamma rays through matter-antimatter annihilation. Taken from [30].

2.3 Gamma-ray fluxes from Dark Matter in the Galactic Center

Collider experiments [32] and large passive calorimeters [3] are probing the mass range of potential Dark Matter (DM) candidates up to hundreds of GeV. However, if DM consists of particles with masses above the TeV scale, astrophysical observations could represent the only viable discovery method in the near future. A key area in DM research is the indirect detection of weakly interacting massive particles (WIMPs), whose mass is estimated in the GeV-TeV range and which exhibit interaction strengths at the weak scale.

Gamma-ray observatories offer a particularly effective approach for DM searches at masses above 1 TeV, thanks to their high sensitivity and sufficient angular resolution. Among the possible targets, the Galactic Center (GC) stands out as the most prominent predicted source of gamma rays from DM annihilation or decay, due to its substantial matter content and relative proximity. This makes it several orders of magnitude brighter than any other expected sources. Despite potential background contamination from astrophysical sources, the GC remains one of the most promising locations for identifying new massive DM particles and serves as the primary focus of this study. DM candidates with masses exceeding 1 TeV can be investigated via the indirect detection of their annihilation or decay products.

The gamma-ray flux from annihilations ($d\Phi_{Ann}/dE_\gamma$) and decays ($d\Phi_{Dec}/dE_\gamma$) of dark matter particles of mass $M_{\rm DM}$ in a DM halo can be expressed as the product of a particle physics term (left parenthesis) and an astrophysical term (right term)

$$\frac{\mathrm{d}\Phi_{\rm Ann}(\Delta\Omega, E_\gamma)}{\mathrm{d}E_\gamma} = \left(\frac{1}{2}\frac{1}{4\pi}\frac{\langle\sigma v\rangle}{M^2_{\rm DM}}\frac{\mathrm{d}N}{\mathrm{d}E_\gamma}\right) \times J(\Delta\Omega) \tag{2.14}$$

$$\frac{\mathrm{d}\Phi_{\rm Dec}(\Delta\Omega, E_\gamma)}{\mathrm{d}E_\gamma} = \left(\frac{1}{4\pi}\frac{1}{\tau_{\rm DM} M^2_{\rm DM}}\frac{\mathrm{d}N}{\mathrm{d}E_\gamma}\right) \times D(\Delta\Omega) \tag{2.15}$$

The particle physics term (left parenthesis) contains the mass of the dark matter candidate M_{DM}, the velocity-weighted annihilation cross section $\langle\sigma v\rangle$, DM lifetime τ_{DM} and the differential spectrum of gamma rays in a specific annihilation or decay channel dN/dE_γ.

The astrophysical factors (right parenthesis), also called J-factor for annihilations and D-factor for decays, are integrated over a given region of interest (ROI) of solid angle size $\Delta\Omega$ along the line of sight (l.o.s.). They are defined as

$$J(\Delta\Omega) = \int_{\Delta\Omega}\int_{\mathrm{l.o.s.}} \mathrm{d}\Omega\,\mathrm{d}s\,\rho^2_{\mathrm{DM}}[r(s,\Omega)] \tag{2.16}$$

$$D(\Delta\Omega) = \int_{\Delta\Omega}\int_{\mathrm{l.o.s.}} \mathrm{d}\Omega\,\mathrm{d}s\,\rho_{\mathrm{DM}}[r(s,\Omega)] \tag{2.17}$$

where ρ_{DM} is the DM density distribution, which will be assumed as an spherical halo surrounding the galaxy. This DM density distribution of the Galactic halo varies greatly between possible functional forms. The Einasto and Navarro-Frenk-White (NFW) profiles are characterized by a steep increase in density of DM towards the galactic center; these distribution types are called *'cuspy'* profiles. According to these models, a high concentration of dark matter is expected in the core regions of galaxies. On the other hand, the Burkert profile is one of the *'cored'* types, which suggest that the dark matter density could be smoother or less dense at the galactic center compared to cuspy-type densities.

In order to estimate the predicted DM flux, it is important to consider different classes of halos. In this work two models are assumed, a peaked Einasto profile (Equation 2.18) [33] and a cored Burkert profile (Equation 2.19) [34], respectively parametrized as

$$\rho_E(r) = \rho_0 \exp\left\{-\frac{2}{\alpha}\left[\left(\frac{r}{r_s}\right)^{\alpha} - 1\right]\right\} \tag{2.18}$$

$$\rho_B(r) = \frac{\rho_c r_c^3}{(r + r_c)(r^2 + r_c^2)} \tag{2.19}$$

Here, r_s and ρ_0 represent the radius and density where the logarithmic slope of the density equals -2, respectively. The parameter α characterizes the curvature of the profile, while ρ_c denotes the central density, and r_c corresponds to the core radius. For the purposes of this study, we explicitly adopt the following values: $r_s = 20$ kpc and $\alpha = 0{,}17$ [33], $r_c = 12{,}67$ kpc [35], with ρ_0 and ρ_c adjusted such that the local DM density is $\rho_{DM} = 0{,}39$ GeV/cm^3 [36; 37]. **Table 2.1** shows the numerical values for both the J-factor and the D-factor with a region of interest (ROI) in the inner 10° of the Galaxy.

The calculated values for the astrophysical factors will later be used in this work to estimate gamma-ray fluxes for different dark matter masses. These fluxes will be used to evaluate the sensitivity of the SWGO detector array. The methodology will be explained in detail later (**4.3**) in this document.

i-th ROI	$\Delta\theta_i = [\theta_{\min}, \theta_{\max}]$	$\Delta\Omega_i$ [10^{-4} sr]	$J(\Delta\Omega_i)$ [10^{19} GeV^2 cm^{-5}]		$D(\Delta\Omega_i)$ [10^{19} GeV cm^{-2}]	
			Einasto	Burkert	Einasto	Burkert
$\Delta\theta_1$	[0.3°, 0.5°]	0.68	75.78	0.17	1.91	0.31
$\Delta\theta_2$	[0.5°, 0.7°]	1.53	129.11	0.38	4.06	0.70
$\Delta\theta_3$	[0.7°, 0.9°]	2.31	154.19	0.58	5.83	1.06
$\Delta\theta_4$	[0.9°, 1.1°]	3.08	168.57	0.78	7.43	1.41
⋮	⋮	⋮	⋮	⋮	⋮	⋮
$\Delta\theta_{45}$	[9.1°, 9.3°]	34.33	110.84	8.10	36.86	15.33
$\Delta\theta_{46}$	[9.3°, 9.5°]	35.09	109.28	8.25	37.23	15.65
$\Delta\theta_{47}$	[9.5°, 9.7°]	35.84	107.76	8.41	37.59	15.97
$\Delta\theta_{48}$	[9.7°, 9.9°]	36.60	106.27	8.46	37.94	16.29
$\Delta\theta_{\text{total}}$	[0.3°, 9.9°]	899.5	7032.9	218.3	1190.0	405.7

Table 2.1 – Definitions of the ROIs with their corresponding inner (θ_{min}) and outer (θ_{max}) radii, the solid angle of each ROI, and values of J-factors and D-factors calculated [38] for both Einasto and Burkert profiles.

2.4 Gamma-ray Detection

When a primary particle enters the atmosphere with high energy, traveling at a velocity close to the speed of light, the collision products with atmospheric nuclei generally continue moving in the same direction as the primary particle. However, as discussed in previous sections, these secondary particles exhibit some degree of lateral dispersion relative to the shower core. During the cascade, the secondary particles produce a diffused flash of light in a cone-shaped pattern directed forward, primarily due to **Cherenkov radiation**. Additionally, isotropic fluorescence light is emitted as a result of nitrogen molecule excitation.

Extensive air showers are detected using various methods and techniques designed to capture and analyze the secondary particles generated by the interaction of cosmic rays with the atmosphere. Below is a brief summary of some of the most commonly used techniques:

- **Fluorescence Telescopes**: These instruments detect ultraviolet light emitted by atmospheric nitrogen molecules when they are excited by the particles in an EAS. These telescopes are capable of observing the particle cascade along its trajectory through the atmosphere.
- **Radio Telescopes**: Extensive Air Showers can generate radio pulses due to the separation of charges in the atmosphere. Radio detectors capture these signals, offering a complementary technique to optical and particle-based methods. Unlike optical techniques, radio detection can operate continuously throughout the day and is not limited to dark, clear nights.
- **Scintillator Detectors**: These detectors use materials that emit light when traversed by charged particles produced in the cascade. The emitted light is then collected by photomultiplier tubes or photodiodes, enabling the detection and analysis of the secondary particles.
- **Cherenkov Telescopes**: These telescopes detect Cherenkov radiation, which is produced when a charged particle travels faster than the speed of light in the atmosphere. The telescope consists of a large segmented mirror that focuses the Cherenkov radiation onto an array of photomultiplier tubes (PMTs), enabling the detection and analysis of this phenomenon.
- **Water Cherenkov Detectors (WCD)**: These detectors use large volumes of pure water to detect Cherenkov radiation produced by charged secondary particles traversing the medium. Typically, they consist of water volumes ranging from one to thousands of cubic meters, equipped with one or more photomultiplier tubes (PMTs) placed inside to capture the Cherenkov light.

It is worth noting that the last two methods, Cherenkov Telescopes and Water Cherenkov Detectors, rely on the detection of Cherenkov radiation. This radiation occurs when a charged particle moves faster than the speed of light in a given medium, such as the atmosphere or water. The principles and characteristics of Cherenkov radiation will be explored in greater detail in the following section.

2.4.1 Cherenkov Radiation

The creation of Cherenkov light is a physical phenomenon that serves as the cornerstone for understanding the indirect gamma-ray detection method used in this work.

This phenomenon occurs when a charged particle travels through a dielectric medium (such as water or air) with a speed higher than the speed of light in that medium. As the charged particle moves, it causes a net polarization in the dielectric medium because the surrounding atoms and molecules will move in order to compensate for its presence, therefore, a net dipole field arises, which disappears when the particle has passed, emitting electromagnetic (EM) radiation in the process.

There are two scenarios in which this EM radiation appears:

- For a charged particle traveling non-relativistically ($v < c/n$ with n the refraction index of the medium) this net polarisation superposes destructively allowing the perturbation to relax as the particle moves on. All dipoles cancel each other out, and no Cherenkov radiation is emitted. This scenario is shown in the left panel of figure 2.12.
- If the speed of the charged particle is higher than the phase velocity of light in the medium ($v \geq c/n$), the perturbation can no longer decay, since the reaction time of the medium is not high enough and the perturbation remains. In this scenario no forward polarisation is present to cancel out the polarised atoms behind the moving particle, creating a conical wavefront of EM radiation according with the Huygens principle. This scenario is depicted in the middle and right panels of figure 2.12.

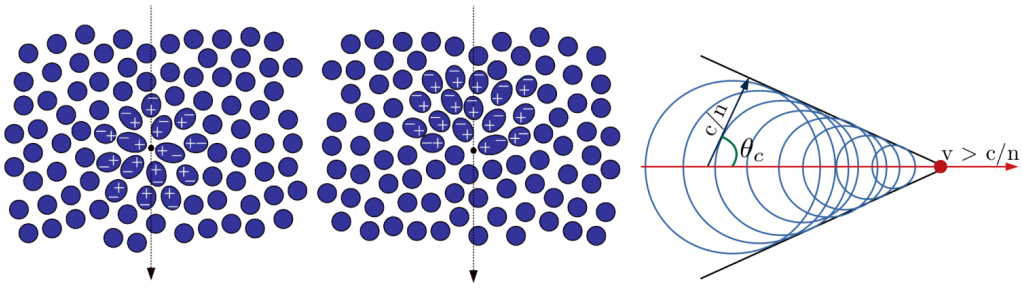

Figure 2.12 – The left diagram illustrates the polarization of the medium as a charged particle travels non-relativistically through it. The middle and the right panels show the emission of Cherenkov radiation when the particle's velocity exceeds the speed of light in the medium ($v > c/n$), forming a characteristic cone with angle θ_c. Taken from [39].

The Cherenkov radiation, which appears as blue light, is emitted in a cone-like form. Its opening angle θ_{cone} can be calculated as

$$\theta_{\text{cone}} = \arccos\left(\frac{c}{nv}\right) \tag{2.20}$$

The threshold energy to produce Cherenkov radiation for a particle of mass m_0 can be written as

$$E_{\min} = \gamma_{\min} m_0 c^2 = \frac{m_0 c^2}{\sqrt{1 - n^{-2}}} \tag{2.21}$$

Since Cherenkov radiation is visible light, it can be measured with the help of photomultipliers and gives information about the characteristics of the original particle (the one which produced the radiation) such as its energy and direction.

2.4.2 Ground-based Gamma-ray Detection Experiments

The detectors used to measure Cherenkov light vary widely in type. On one hand, we have distributions of *Imaging Atmospheric Cherenkov Telescopes* (IACT) deployed. These arrays consist of multiple mirror telescopes that reflect photons from the Cherenkov cones produced by the EAS into cameras for recording. By analyzing the number of detected photons and the area covered by the telescopes, important properties of the primary gamma rays can be determined. Examples of observatories currently using this technique include the *High Energy Stereoscopic System* (H.E.S.S.) [40] located in Namibia, the *Very Energetic Radiation Imaging Telescope Array System* (VERITAS) [41] located in the United States, and the *Major Atmospheric Gamma Imaging Cherenkov* (MAGIC) telescopes [42] located in the Spanish island of La Palma. Additionally, the *Cherenkov Telescope Array Observatory* (CTAO) [43], an ambitious project with observation sites planned for both the Northern (currently under construction) and Southern Hemispheres (to be constructed in Chile), aiming to provide complete sky coverage.

Another approach to measure gamma rays using the Cherenkov technique is through *Water Cherenkov Detectors* (WCD). In these detectors, photo sensors are submerged within large water tanks. Secondary particles from an EAS interact with water nuclei, generating Cherenkov radiation similar to that detected by IACTs. The light is then measured by the photo sensors, followed by the reconstruction of the direction and energy of the incident particle. Examples of experiments employing WCD include the *High-Altitude Water Cherenkov Gamma-Ray Observatory* (HAWC) [13] in Mexico and the *Large High Altitude Air Shower Observatory* (LHAASO) [12] located in China. Unlike IACTs, where Cherenkov light is generated in the atmosphere, WCDs require the light to be produced inside the detector itself, consequently, WCD observatories must be located at higher altitudes compared to IACT sites, typically between 4 km- 5 km above sea level, in order that they are able to detect the greatest amount of secondary particles, which will correspond to the height in which the longitudinal profile of the shower is maximum (right panel on figure 2.4).

In general, IACTs are preferred for spectral and morphological observations due to their superior angular and energy resolution. However, WCDs offer several advantages: they have a high duty cycle of nearly 100 % and a large field of view. Unlike IACTs, WCDs are not restricted to nighttime observations and are less affected by weather conditions. Since WCDs are enclosed, they enable continuous measurements under all conditions. These characteristics make WCDs particularly well-suited for investigating extended sources [39] and to detect variability, particularly unexpected transients such as gamma-ray bursts.

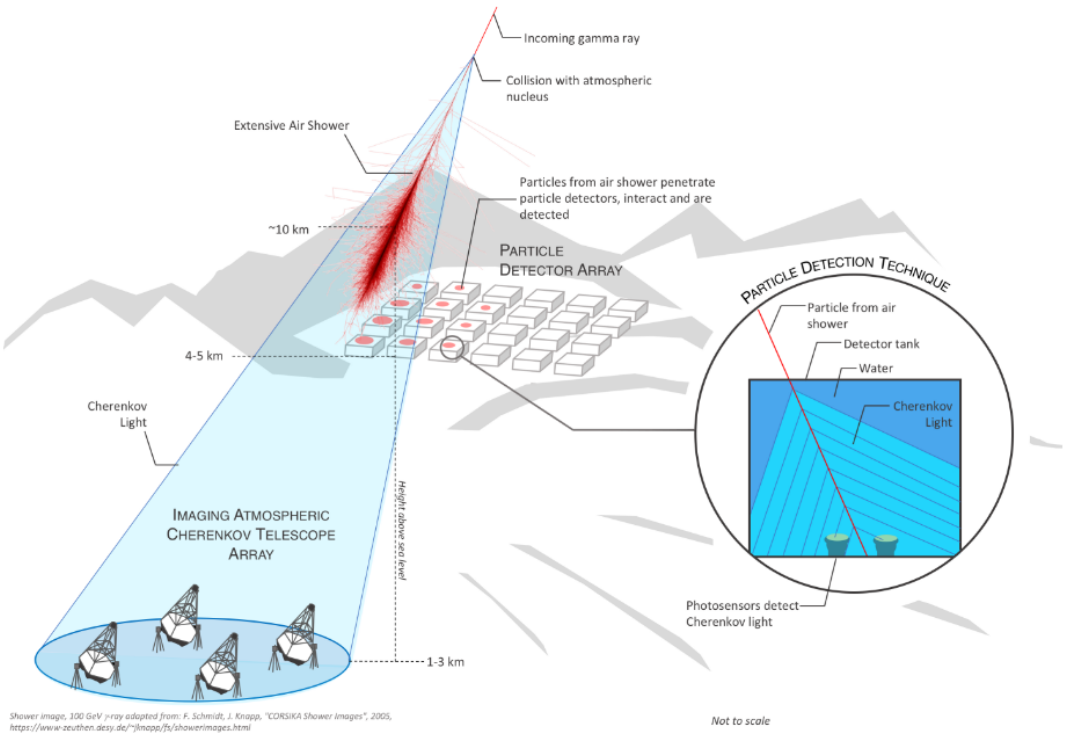

Figure 2.13 – Different detection techniques for ground-based gamma-ray astronomy. The inset shows the internal process of the WCD in collecting Cherenkov radiation. Taken from [44].

Figure 2.13 illustrates both and IACT setup and a WCD array. The right panel zooms in on the interior of a WCD, showing how secondary particles from an air shower penetrate the water tank and generate a Cherenkov cone, which is then detected by the photo sensors.

3 The Southern Wide-field Gamma-ray Observatory (SWGO)

The scientific potential of a ground-based gamma-ray detector with a wide field of view and a high-duty cycle has already been demonstrated by observations of existing collaborations such as HAWC [13], the ARGO-YBJ Experiment [45], and LHAASO [12]. To date, no such instrument exists in the southern hemisphere, where there is significant potential to map large-scale emissions [44]. The main objective of SWGO can be summarized in four key pillars: unveiling the nature of galactic and extragalactic particle accelerators (galactic center, Fermi bubbles, supernova remnants, pulsar wind nebulae, active galactic nuclei and star forming regions), monitoring high-energy transient phenomena (active galactic nuclei and gamma ray bursts), exploring particle physics beyond the Standard Model (dark matter, primordial black holes and axion-like particles), and characterizing the cosmic ray flux in regard to its spectrum and composition as well as its anisotropy.

The measurements conducted by SWGO will serve both to verify previous observations made by HAWC and LHAASO and to investigate new sources, particularly in regions of the sky that are currently inaccessible to these instruments. These regions are highlighted in Figure 3.1. Furthermore, this observatory will complement the future CTA-South [43] facilities, planned for construction in the Southern Hemisphere due to their proximity, as both will be built in the same region.

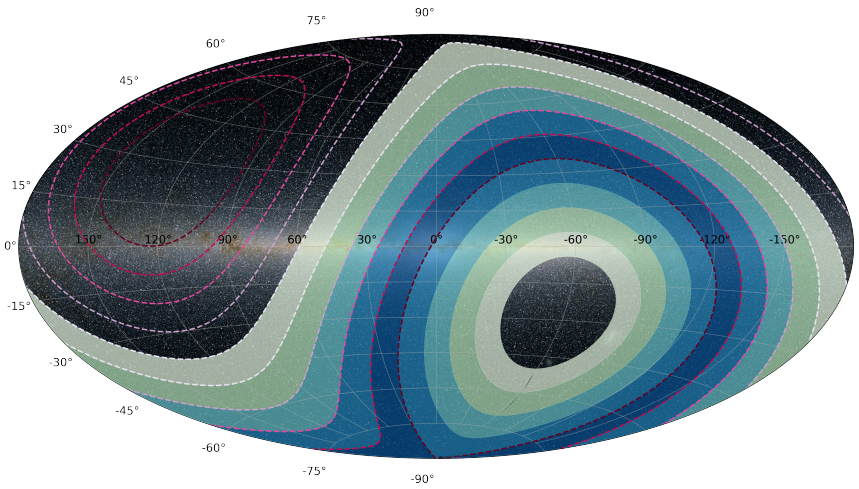

Figure 3.1 – Aitoff projection of the Milky Way in galactic coordinates. The colored region represents the area observable by SWGO, while the dashed lines outline the current region observable by HAWC. [1]

[1] `https://gitlab.com/swgo-collaboration/sandboxes/harmscho/field-of-view`

As its southern hemisphere counterpart, the structure and operation of SWGO will be strongly inspired by HAWC, which is composed of many Water Cherenkov Detectors (WCD) distributed over a wide perimeter, designed to cover the largest possible area. In addition, it will be located at a high altitude in order to capture the maximum number of particles. In general, the main features of the future observatory are as follows [46]:

- It will be located in the Atacama Astronomical Park, Chile, at an altitude of 4770m above sea level, with coordinates 22°S, 67°W.
- It will cover an energy range from ∼100 GeV to the PeV scale.
- It will have a field of view of approximately 90° and a duty cycle close to 90 %.
- It will have a high density of detectors near the core of the distribution, surrounded by two concentric rings with lower detector density, covering a surface area significantly larger than HAWC, which spans approximately 20000m^2 with its array of 300 WCDs.

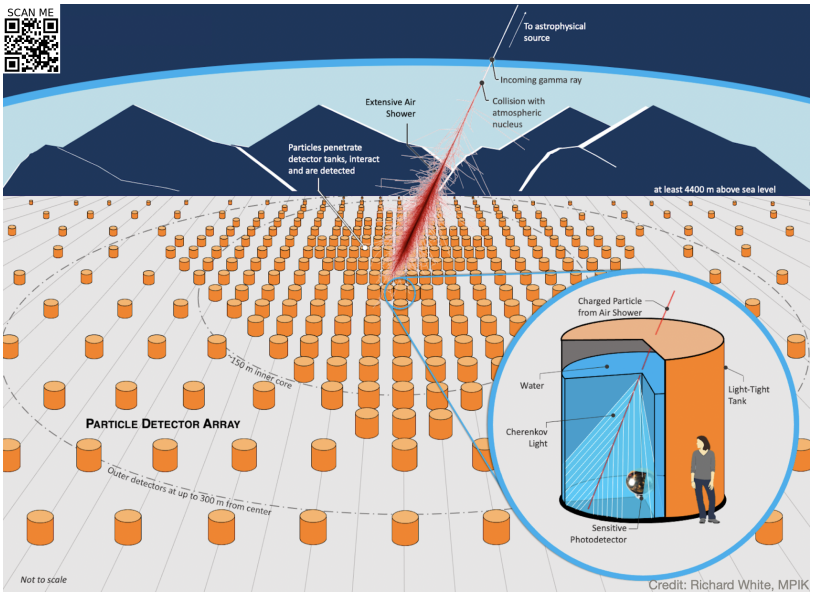

Figure 3.2 – Scheme of the array distribution for SWGO. The inset shows the interior of the WCD [46].

Throughout the development of SWGO, various tank designs and surface distributions have been proposed. These configurations have been thoroughly studied and compared by the collaboration through computational simulations, a methodology that will be explained in greater detail in the next chapter (**4**). For this work, not all configurations will be considered; our simulations have been performed using the main design selected by the collaboration as of the date of this document, referred to as the '**D8**' configuration.

3.1 Technical Overview

The configuration used for the simulations in this work consists of a set of 3763 Water Cherenkov Detectors. The design selected for each unit, referred to by the collaboration as '**Design D**', consists of a cylindrical water tank with a diameter of 5.2 meters. This tank has the distinctive feature of being a dual-layer design: The upper layer serves as a detector for electromagnetic particles, while the lower layer acts as a detector for penetrating muons. Each layer is equipped with a photomultiplier tube (PMT), responsible for collecting photoelectrons generated by Cherenkov radiation. In the upper layer, the PMT is located at the center of the base, pointing upwards, whereas in the lower layer, the PMT is mounted on the ceiling, pointing downward. Figure 3.3 shows a schematic of this tank design, created with Geant4.

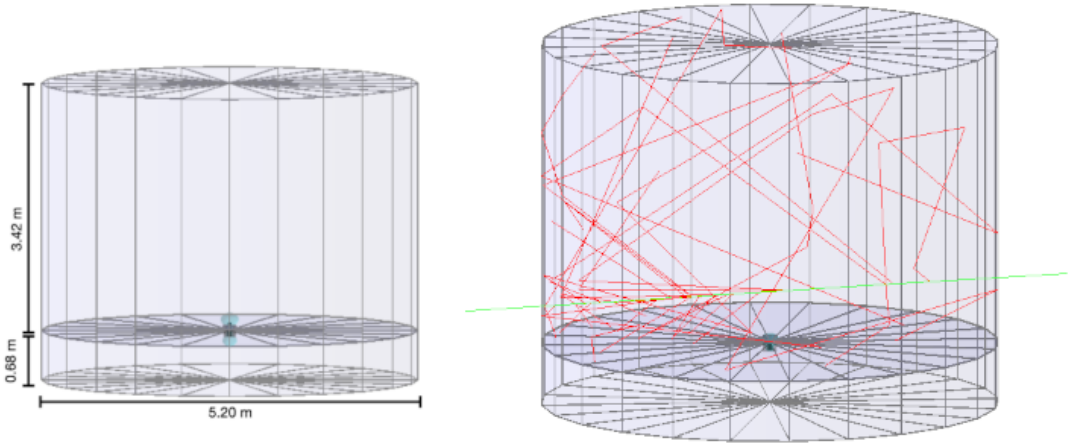

Figure 3.3 – Illustration of the detector design 'D' generated with Geant4. The right panel shows a muon (green) traveling through the detector from left to right with the scattered Cherenkov photons (red) inside the WCD.

The distribution of these 3763 detectors on the surface corresponds to the design referred to by the collaboration as ´**Layout 8**'. This design consists of a circular area with a variable density of tanks, decreasing as the distance from the center increases. These zones and their respective densities are characterized by the so-called ´fill factor (FF)', which represents the percentage of the area covered by detectors in each zone.

For layout 8, three zones are defined:

1. **Zone 1**, located at the center, is a disk with a radius of 156m and a fill factor of 70.0 %, containing the majority of detectors (2587 tanks).
2. **Zone 2** corresponds to a concentric ring around Zone 1, with an inner radius of 156m and an outer radius of 400m, a fill factor of 4.0 %, and 792 tanks.
3. **Zone 3** is the outermost ring, with an inner radius of 400 m and an outer radius of 560m, a fill factor of 1.7 %, and 384 detectors distributed within this region.

This configuration covers a total area of approximately $\sim 10^6$ m^2, significantly larger than the 2×10^2m^2 covered by HAWC.

The zoned distribution with varying detector densities enables SWGO to achieve a wide energy range. The inner zone collects low-energy events (due to their limited lateral spread), while the outer zones capture high-energy events (which trigger a larger number of detectors).

The combination of Design D and Layout 8 results in the **D8** configuration used in these simulations, selected for this work as it represents one of the most recent configurations studied by the collaboration at the time of this analysis.

Figure 3.4 shows a schematic representation of layout 8, while Table 3.1 provides a summary of all the mentioned characteristics of the **D8** configuration used in this work.

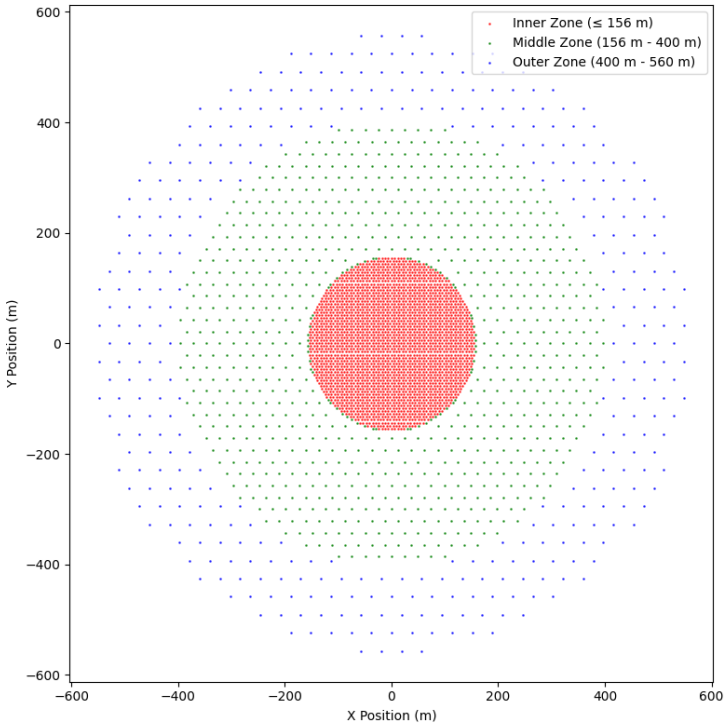

Figure 3.4 – Distribution of the WCDs used in the simulations, referred to as 'Layout 8'. The red dots represent the inner dense zone (Zone 1), while the green (Zone 2) and blue regions (Zone 3) correspond to the outer rings with lower detector density.

Config.	**Zone 1**			**Zone 2**			**Zone 3**		
	FF(%)	Radius (m)	Units	FF(%)	Radius (m)	Units	FF(%)	Radius (m)	Units
D8	70.0	156	2587	4.0	400	792	1.7	560	384

Table 3.1 – Summary of the different zone configurations for the D8 detector design.

3.2 Event Reconstruction

To evaluate the capabilities of the detector through simulations, it is essential to first reconstruct the properties of the primary particle that collided in the atmosphere based on the characteristics of the secondary particles detected by the PMTs on the Earth's surface. These properties include the type of primary particle, its energy, and its direction. For example, the properties of a reconstructed event: 'Type: photon, Energy: 35 GeV, Momentum: px, py, pz' etc.

This section will provide a brief description of the methodology used by SWGO to reconstruct these properties, which is strongly inspired by that developed by HAWC. In the following chapter we will delve into how these reconstructed properties are used to subsequently evaluate the efficiency of the detector.

3.2.1 Direction Reconstruction

Based on the method currently used in HAWC, the reconstruction of the primary particle's direction involves fitting a plane to the shower's wavefront. This is not a trivial problem, as the nature of interactions in the atmospheric cascade causes the wavefront to deviate from a plane and curve as the distance from the shower core increases, as illustrated in Figure 3.5.

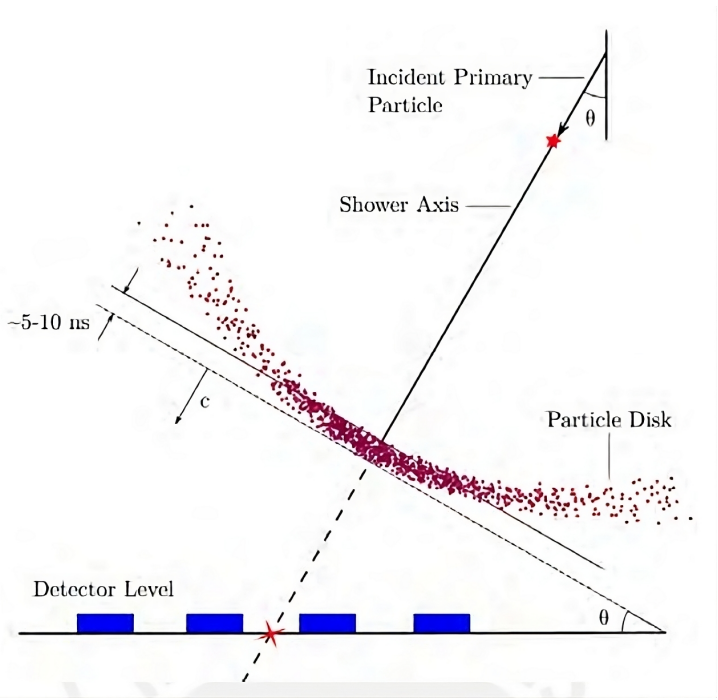

Figure 3.5 – Air shower front (red dots) with higher particle density near the shower axis defined by the primary particle. Marked with a red star, the reconstructed shower core location from the intersection of the shower axis and the surface. Taken from [47].

The reconstruction process begins with a preliminary estimation of the shower core position, based on the center of mass of the charge distribution in the detector array, the so called 'COMCoreFit'. Subsequently, a plane is fitted to the shower wavefront. The construction of this plane relies on the temporal differences of the impacts measured by different tanks for a given event. As a first approximation, this plane is considered to have an initial thickness of approximately 5 ns, which increases by 0.15 ns for every meter of distance from the shower core [47]. Finally, using these approximations and the temporal correction, a more precise measurement of the shower core is performed using a maximum likelihood method with respect to some pre-generated templates, revealing the final information about the direction of the incident particle (θ, ϕ).

3.2.2 Energy Reconstruction

For the reconstruction of the primary particle's energy, a method is employed that compares the Lateral Distribution Function (LDF) of an event with **templates** previously generated using Monte Carlo (MC) simulations.

These templates, which can be defined as three dimensional histograms that visualize the probability $log(P)$ that a certain number of photoelectrons $log(n_{\mathrm{PE}})$ are triggered at a distance r to the shower core in response to an EAS that falls within a set of given energy, zenith angle θ and depth of the shower maximum $X_{\mathbf{max}}$ [48]. For each combination of bins, one template is generated and filled with MC shower data. The Probability Density Functions (PDF) generated by this method are later compared to the LDF of a 'real' event by minimizing the following negative log-likelihood function

$$\log L = -2 \sum_i \log \left(F \left(\log_{10}(N_{\mathrm{PE}})_i, r_i, X_{\mathrm{max}}, E \mid \theta, \phi \right) \right) \tag{3.1}$$

where the function F describes the probability that a certain detector unit i measures a certain number of photoelectrons PE at a distance r_i from the shower core for an event with set X_{max}, E, θ and ϕ values [49].

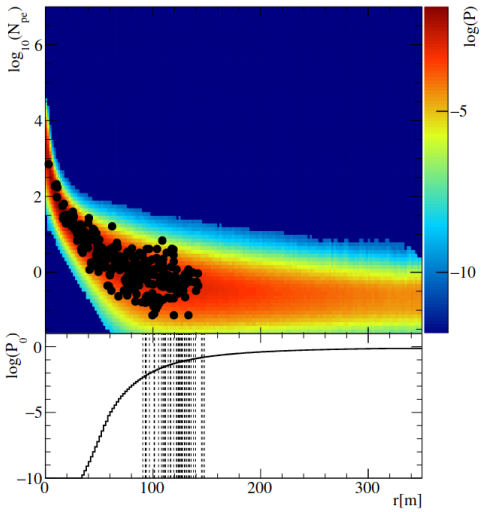

Figure 3.6 – Template fit for an event with true energy $\sim$ 16TeV, reconstructed energy of $\sim$ 17TeV, true $X_{max} \sim$ 400g/cm^2 and reconstructed $X_{max} \sim$ 423g/cm^2. This plot shows the probability (P) distribution as a function of the number of photoelectrons log(N_{pe}) and impact distance (r). The colorbar represents the probability in logarithmic scale. The black dots shows the LDF for non-zero N_{pe} and observed zeros are shown as the dashed lines on the histogram below with their corresponding probability. Taken from [48].

Figure 3.6 shows an example of this fitting process performed by Joshi et al. [48]. This figure presents the LDF of a simulated event overlaid on the PDF of one of the previously generated templates. In this example, the true energy of the event is approximately 16 TeV, while the reconstructed energy is approximately 17 TeV. Similarly, the true $X_{\max}$ value is $\sim$ 400 g/cm^2, and the reconstructed $X_{\max}$ value is $\sim$ 423 g/cm^2.

Finally, the parameters obtained from the minimization provide an estimate of the true energy of the primary particle that caused the EAS, the position of its core described by the coordinate pair (x_c, y_c) in the detector array plane, and the position of the shower maximum, $X_{\max}$.

One of the main advantages of this method is that it can be applied to distributions with different types of detectors. This is achieved by summing the log-likelihood functions of each detector type in the distribution to obtain the total function to minimize. This approach is particularly important for SWGO due to the dual-layer design (with different geometries) of the WCDs, where each cell must be modeled as a separate detector.

$$\log L_{\text{tot}} = \log L_{\text{det},1} + \log L_{\text{det},2} + \dots \tag{3.2}$$

3.2.3 Gamma-Hadron Separation

In previous sections it was mentioned that the EAS produced by protons (hadrons) propagates differently through the atmosphere than those produced by gamma rays.

One of the main differences between the showers produced by these two types of primary particles is that gamma rays do not deviate in their trajectory from their source to the Earth. Therefore, identifying the type of primary particle is essential for correctly characterizing the sources under study.

Currently, SWGO uses various tools to classify the primary particles that generate the EAS, with new tools under development. This section will discuss the main parameters that enable the identification of the primary particle type, while the details of the tools used for classification will be covered in the next chapter.

The first estimator used to identify the type of primary particle is based on the previously generated templates, as these are generated assuming gamma-ray showers. This enables an initial classification using the associated likelihood value. Next, we have the three main classifiers used, which are called *LCm*, *PINCness*, and *LDFChi2*:

LCm Parameter

This discriminator uses the total number of events measured by the PMTs of the WCD station (total signal) to evaluate the level of azimuthal fluctuations in the shower footprint. Cosmic-ray-induced showers produce 'clumps' of charges in their shower footprint, whereas gamma-ray-induced showers exhibit a much smoother distribution. These asymmetries are computed from the 'C_k profile' [50], which is a function of the distance to the shower core. This quantity is computed in successive circular rings centered at the shower core with a radius r_k in the shower transverse plane, where essentially, it measures how unequal the signals are between station pairs within ring r_k, normalized by the average signal in that ring

$$C_k = \frac{2}{n_k(n_k-1)} \frac{1}{\langle S_k \rangle} \sum_{i=1}^{n_k-1} \sum_{j=i+1}^{n_k} (S_{ik} - S_{jk})^2 \tag{3.3}$$

where n_k is the number of stations in ring k, $\langle S_k \rangle$ is the mean signal in the stations of the ring k, and S_{ik}, S_{jk} are the collected signals in the stations i and j of the ring k respectively.

From the C_k distribution as a function of r_k, the gamma/hadron discriminating variable **LCm** is defined as the value $\log(C_k)$ distribution at a given $r_k = r_m$

$$LC_m \equiv \log\left(C_k\right)\big|_{r_k=r_m} \tag{3.4}$$

In extensive air showers, the azimuthal distribution of signals (represented by C_k) varies with the distance from the shower core (r_k), due to the subcomponents of the hadronic showers. However, the parameter LC_m allows the selection of an optimal radius r_m where the difference between gamma-ray and proton showers is maximized.

PINCness (Parameter for IdeNtifying Cosmic rays)

As mentioned before, gamma-ray induced showers produce a much smoother distribution compared to the hadronic ones. The PINCness parameter quantifies this smoothness by defining concentric rings around the shower core and calculating the average charge in each of them. The charge of a PMT at a given distance from the core is then compared to the average charge of the corresponding ring using a χ^2 fit.

$$PINC = \frac{1}{N}\sum_{i=0}^{N}\frac{\left(\log_{10}(q_i) - \langle\log_{10}(q_i)\rangle\right)^2}{\sigma^2} \tag{3.5}$$

where N is the number of PMT's hit (above some pre-defined threshold), $\log_{10}(q_i)$ is the log of the charge in the *ith* PMT and $\langle\log_{10}(q_i)\rangle$ is the average of all charges measured within a 10m annulus of the *ith* PMT. Finally this parameter is divided by the degrees of freedom (DOF), which is the number of PMTs hit in a given event to get the χ^2 statistics

$$\chi^2 = \frac{PINC}{DOF} \tag{3.6}$$

A low PINCness value indicates a smooth LDF, consistent with gamma-ray events, while a high PINCness value suggest a more dispersed LDF, consistent with hadronic events.

LDFChi2

The LDFChi2 gamma/hadron separator utilizes a likelihood fit to the Lateral Distribution Function to separate gamma events from hadron events. This parameter is the reduced χ^2 obtained from fitting the $\tilde{\text{N}}$DF with the expected shape given by the NKG (Nishimura-Kamate-Greisen) [51] function

$$NKG = A\rho^{s-3}\left(1+\rho\right)^{s-4,5} \tag{3.7}$$

where ρ is the distance from the shower core (r_{axis}) to the PMT under analysis at the observation level, expressed in units of the Molière radius ($\rho = r_{\text{axis}}/R_m$); A is the amplitude (normalization parameter) and s is the shower generation (**Figure 2.2**).

A maximum likelihood fit is performed to determine the amplitude and shower age of the modified NKG function. The best-fit values from the likelihood fit are then used to calculate the expected logarithm of the charge in a PMT, $\log(q_{\text{LDF}})$. This expected charge is compared to the experimental charge measured in the PMT, $\log(q_i)$, using a χ^2 test statistic.

$$\chi^2_{\text{sum}} = \sum_{i=0}^{N}\frac{\left(\log_{10}(q_i) - \log_{10}(q_{\text{LDF}})\right)^2}{\sigma^2} \tag{3.8}$$

where N is the number of PMTs hit in a given event. Finally, the result is divided by the degrees of freedom to obtain the final statistic.

$$\chi^2 = \frac{\chi^2_{\text{sum}}}{DOF} \tag{3.9}$$

Due to the more homogeneous nature of gamma-ray events, the model will generally fit better for gamma-ray showers than for hadronic ones.

4 Shower Simulations

To accurately evaluate the efficiency of a detector against various gamma-ray signals, it is essential to obtain the Instrument Response Functions (IRF) which define the relationship between reconstructed and true properties of incoming gamma rays. These functions are crucial for determining the detection capabilities, data acquisition efficiency, and reconstruction accuracy of SWGO (and every detector). In general, they are used to compare expected (simulated) gamma-ray showers with observed (detected) ones, and further contrast them with the hadronic shower background to estimate SWGO's gamma-ray detection sensitivity. The main IRFs to be calculated, which will be explained in detail in this chapter, include the effective area (A_{eff}), the Point Spread Function (PSF), associated with the detector's angular resolution, the Energy Dispersion Function (EDF), related to energy resolution, and the sensitivity curves.

Table 4.1 provides a summary of the steps involved in obtaining these curves, this is the so-called 'Reconstruction Chain', which range from simulating atmospheric showers, modeling detector responses to these showers, reconstructing the properties of each primary particle, and their subsequent classification and selection for use in the IRFs.

Program/Library	Description	Language
CORSIKA	Particle shower simulations.	Fortran
HAWCSim	Simulation of detector response to shower secondary particles.	C++
swgo-reco	▪ Simulates PMT response. ▪ Reconstructs primary particles properties.	C++
pyswgo-make-event-level	▪ Reduces output of swgo-reco to only event level parameters. ▪ Adds certain variables useful for IRF generation.	Python
pyswgo-classify-events	▪ Adds (final) single variable for gamma/hadron separation. ▪ Generate cut values for IRF.	Python
pyswgo-make-irfs	Generates all the IRFs based on the previously classified events according to the cut values.	Python

Table 4.1 – General summary of the reconstruction chain.

4.1 Detector Simulation

The detector simulation consists of two main steps: the simulation of atmospheric showers using the CORSIKA program [52], and the simulation of the detector response using the HAWCSim application, which is based on the GEANT program [53] developed by CERN.

4.1.1 CORSIKA: Air Shower Simulations

CORSIKA (COsmic Ray SImulations for KAscade) is a Monte Carlo-based program used to study the evolution and properties of extensive air showers [54]. It was originally developed for the KASCADE experiment [55] in Karlsruhe, Germany, to measure the elemental composition of primary cosmic radiation in the energy range of 3×10^{14} to 1×10^{17} eV. The first version of CORSIKA was released on October 26, 1989, and has since been continuously expanded and improved.

This program simulates the interactions and decays of nuclei, hadrons, muons, electrons, and photons in the atmosphere, handling energies up to approximately 10^{20} eV. It provides detailed information on the type, energy, location, direction, and arrival times of all secondary particles produced in an air shower.

CORSIKA consists of four main components. The first handles data input and output, performs the decay of unstable particles, and tracks particles while accounting for energy loss due to ionization, deflection by multiple scattering, and the Earth's magnetic field. The second component deals with high-energy hadronic interactions of nuclei and hadrons with air nuclei. The third simulates hadronic interactions at lower energies, and the fourth describes the transport and interaction of electrons, positrons, and photons.

The atmospheric showers simulated in this work were performed using version 7.7500 of the CORSIKA package. The software was configured to use the *QGSJET II* model [56] for high-energy hadronic interactions and the *URQMD* model [57] for low-energy interactions, in accordance with the parameters established by the collaboration. A detector distribution in a plane was selected, allowing the coordinate system used by CORSIKA to position the incident particle, as shown in **Figure 4.1**.

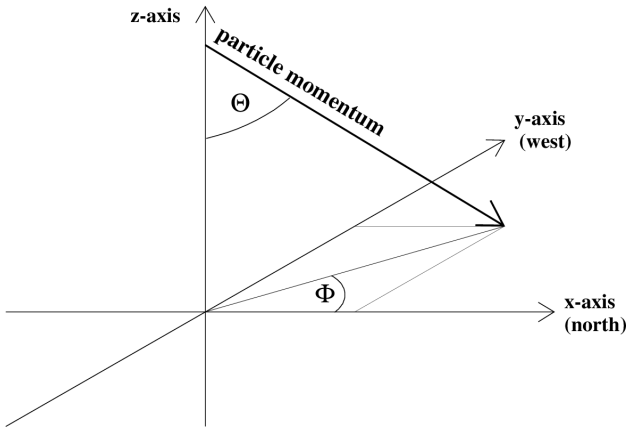

Figure 4.1 – The coordinate system used by CORSIKA is defined with the x-axis pointing to magnetic north, the y-axis to the west, and the z-axis upwards. The origin of the system is set at sea level [54].

Further details on the full parameters of the shower simulations will be reviewed in the following chapter.

4.1.2 HAWCSim: Detector Response

The detector response simulations were performed using the HAWCSim package, adopted from HAWC and later customized for SWGO.

HAWC software, called the Analysis and Event Reconstruction Integrated Environment (**AERIE**), provides a framework for event processing and subsequent analysis. It is structured as a set of interdependent C++ projects connected by a central framework that offers: an execution cycle for batch data analysis, libraries for integrating custom algorithms, data classes to store simulated and reconstructed data and libraries for handling common tasks such as storing geometric or temporal data. One of the core components is HAWCSim, which uses the external Geant4 package to simulate detector responses under the selected SWGO configuration.

HAWCSim takes as input the showers generated by CORSIKA, which are stored in its output files. These showers are injected 10 m above ground level.

Field	Description	Unit
Evt.Num	Number of generated showers.	
Evt.nEMParts/nMuParts/nHadParts	Number of electromagnetic(EM)/muonic(Mu)/hadronic(Had) particles arriving at the detector.	
Evt.nPE	Total number of photoelectrons (PE) detected by the PMTs	
Evt.nWHit	Total number of particles that hits the water.	
Evt.Energy	Primary particle energy.	GeV
Evt.pType	Primary particle type.	
Evt.Theta/Phi	Zenithal/Azimuthal angle of the primary particle impacting the atmosphere.	deg
Evt.firstTime	Arrival time of the first particle detected in each event.	ns
Evt.EM/Mu/Had/Ene	Total energy of the EM/Mu/Had arriving particles.	GeV
Evt.X/Y	Event core position for each event.	cm
WH.XNE/YNE/ZNE	X, Y, Z position of each water hit.	cm
WH.Theta	WH zenithal angle.	deg
WH.TankID	ID of the tank impacted by the WH.	
WH.Energy	WH energy.	GeV
PE.PMTID	ID of the PMT which detects a PE.	
PE.Time	Time at which a PE arrives at a PMT.	ns
PE.Radius	Radius from the center of the PMT where the photoelectron hit.	cm
PE.Phi	Azimuthal angle where each PE impacts.	deg
PE.Energy	Energy of each photoelectron.	eV
PE.origPartType	Particle type of the particle responsible for the PE.	

Table 4.2 – Summary of the most relevant HAWCSim parameters. 'Evt' refers to initial shower properties, 'WH' refers to particles impacting the water tank and 'PE' refers to the simulated photoelectrons detected by the PMTs.

Table 4.2 presents the most relevant variables stored by HAWCSim during event processing. The prefix `Evt` refers to the original shower information from the CORSIKA simulation, the prefix `WH` indicates when shower particles penetrate the water in the tanks, and the prefix `PE` corresponds to the photoelectrons generated within the tank that activate the PMTs.

The HAWCSim output file records the arrival times of photons detected by the PMT at its photocathode. Since a low-energy electron can produce thousands of photons, which are tracked until absorption (either by the water volume or the walls), photon tracking performed by HAWCSim is the most computationally demanding stage in the entire reconstruction chain.

4.2 AERIE: Event Reconstruction

The executable responsible for shower reconstruction is **swgo-reco**, which chains a sequence of services that perform various tasks. The input files, in **.xcd* format, correspond to the output files produced by HAWCSim after simulating the detector response.

Below is a list with a brief summary of the most important services executed during the reconstruction process with swgo-reco, remembering that the details behind some of them was already explained:

- **DAQSim**: It collects the arrival times and charges of the photoelectrons in the photodetector, storing them in the so-called **hits**.
- **COMCoreFit**: First estimation of the shower core based on the center of mass of the detected hit charges.
- **GaussPlaneFit**: Plane fit to the shower front to accommodate the curvature produced by the particle propagation.
- **LHLatDistFit**: This module uses the template method to reconstruct the core location and the energy of the primary particle. This module also works as a first gamma/hadron separator.
- **PINCCalculator**: Gamma/hadron separator. Corresponds to the PINCness parameter already defined.
- **LatDist**: Gamma/hadron separator. Corresponds to the LDFChi2 parameter already defined.
- **LCm**: Gamma/hadron separator. Corresponds to the LCm parameter already defined.
- **SummarizeRec**: Selects which reconstructed parameters go to the output file.
- **PMTSignalTimeTrace**: Saves the signal time trace of each detector unit with a given time bin.

4.3 pyswgo: Event Classification and IRF Generation

The pyswgo package is a python based code repository that is designed to perform event classification and posterior production of the instrument response functions. As the final step in the reconstruction chain, it processes the ROOT format outputs delivered by swgo-reco in three sequential steps.

1. Event Level

The output of swgo-reco contains information on the measurements performed by the PMTs, as well as event-level data related to the reconstructed primary particle. The first task of **pyswgo** consists on the executable `pyswgo-make-event-level`, where the data is first binned, in order to study and optimize the performance for different event classes. The binning of the reconstructed events is based on the location of the shower core within the distribution, specifically in zones 1, 2, or 3 for the D8 configuration. Additionally, events are binned by the zenith angle of the primary particle into two groups: low zenith and high zenith. Finally, they are also binned according to the reconstructed energy of the primary particle. Table 4.3 shows a summary of the specific bins used in this work.

Binning type	**Ranges**	**Units**
Zenith Binning	[0, 30, 52]	deg
Core Binning	[0, 156, 400, 560]	m
Energy Binning	[1.0, 2.0, 2.5, 3.0, 3.5, 4.0, 4.5, 6.0]	$\log(E_{Reco})$

Table 4.3 – Complete set of binnings performed to the reconstructed events.

This executable keeps a selection of event-level parameters obtained by swgo-reco while several new variables are calculated according to some selection cuts based on the binning scheme. Some of the most important parameters calculated are new gamma/hadron separators, where the following three (independent) algorithms are currently included in the package:

- **Muon Tagger**: This classifier takes as input a set of features extracted from simulated detector data, including charge measurements from the PMTs, time differences between signals, reconstructed energy and zenith angle, and the detector's distance from the shower core. The Multilayer Perceptron (MLP) is trained to distinguish muon signals from non-muon signals by leveraging these features, producing probabilities for each detector unit that indicate the likelihood of detecting a muon. The training process involves data pre-processing, where features are normalized and the dataset is balanced by duplicating rare muon events to address class imbalance. The MLP architecture consists of two hidden layers with ReLU activation, trained using the Adam optimizer with binary cross-entropy as the loss function.

- **Graph Neural Networks (GNN)**: The process begins by transforming simulated event data into 2D point clouds, where each point represents a triggered detector station. To construct the graph representation, a *k-next neighbors* (KNN) clustering approach is applied, connecting each station to its six closest neighbors based on spatial proximity. The features used for analysis include the x and y coordinates of the stations, particle arrival times, and the charge recorded by the PMTs. These features undergo normalization, with timing data standardized using z-score normalization and charge values log-scaled to improve model stability. Once the graph is constructed, the GNN model processes the event data using convolutional layers, which capture local spatial relationships by learning patterns based on the neighboring station features. The network architecture consists of multiple convolution layers followed by global pooling and fully connected layers, allowing the extraction of both local and global event features. The GNN model is trained to optimize performance for two key tasks: gamma/hadron separation and energy reconstruction.
- **DeepEASTER**: 'Deep learning for Extensive Air Shower Targeted Event Reconstruction' is a module first implemented in HAWC for gamma/hadron separation, applying the attention-based deep learning method [58]. Attention layers allow the model to learn holistically the relationship between PMTs and the vector representing the shower. The shower representation vector is updated by the attention layers and is the input to the final layer, the MLP head. The MLP head computes the target variables: 'Gammaness' for event classification, and direction, energy, and core position for event reconstruction.

One can choose to activate all three algorithms to achieve a more robust calculation of gammaness and reconstruction parameters at the expense of increased computational cost. For this work, only the first two algorithms were used.

Table 4.4 provides a summary of the relevant output of the first executable calculated for our simulations.

Parameter	Description
fBin	Bin label for the event.
event.AFQ	Angle Fit Quality.
event.LHQ	Likelihood Fit Quality.
event.nMuHE	Number of high efficiency muons (higher false positive rate).
event.nMuHC	Number of high confidence muons (lower false positive rate).
event.gnnGammaness	Gamma-ness predicted by a graph neural network analyzing the shower footprint.

Table 4.4 – Relevant outputs given by `pyswgo-make-event-level` necessary as inputs for the next step in the reconstruction chain.

2. Event Classification

The output of the previous step will be evaluated by the next executable *pyswgo-classify-events*. The objective of this package is to obtain values on which events can be selected as suitable for the production of IRFs. The selection criteria are related with the quality of the geometry and energy reconstruction, and the 'gamma-ray likeness' of each event.

The cut values used to assess the quality of the reconstruction are based on the previously generated parameters, **event.LHQ** (likelihood cut) and **event.AFQ** (direction cut), with event selection performed for each **fBin** according to the following criteria:

1. The top 50 % of events with the best angular reconstruction in the analyzed bin are selected by evaluating the variable **mc.delAngle**.
2. Within this selected set, the mean $\overline{X}$ and standard deviation σ_X of the variable X (event.LHQ or event.AFQ) are calculated.
3. Finally, event selection is performed using the cut value $C_X = \overline{X} + k_X \sigma_X$, where k_X is configurable. The default cut values are 1.8 for AFQ and 2.1 for LHQ.

To select events with 'gamma-ray likeness', the parameters generated by **swgo-reco** are combined with the variables obtained in *pyswgo-make-event-level*, along with other relevant variables for classification, such as the zenith angle or the number of hits in the detector. These data are then used to build a MLP neural network. The output of this network represents the probability of an event being a gamma ray and is stored in the variable **rec.probaMLP**.

The new output file is divided into a training dataset and a test dataset, with the latter being used in the next step of the sequence.

3. IRF Generation

The final step involves generating the Instrument Response Functions (IRFs) required to assess the detector's performance against the simulated signal. These curves reflect different aspects of the overall performance of the distribution. The IRFs presented in this work are the following: Effective Area, Angular Resolution, Energy Resolution, Background Rejection, and Sensitivity, which will be defined below.

- **Effective Area**:

  The effective area represents the detector's collection area and characterizes the detection efficiency of a given instrument or detector system for incident particles. It depends on the true energy of the photons and the observation zenith angle. It is one of the key components for obtaining the event count per energy bin and subsequently estimating the detector's sensitivity.

  The effective area is calculated using two key components: the spectrum used to simulate gamma-ray events and the list of gamma-like events that remain after reconstruction and classification.

  The formula for computing this value establishes a connection between the total number of simulated shower events and the number of simulated events that trigger the instrument and can be successfully reconstructed, meeting all the selection criteria applied in previous cuts. The effective area (A_{eff}) for observing a source transiting between θ_{low} and θ_{up} is estimated as:

$$A_{\text{eff}}(E) = \frac{1}{2\pi \left(\cos(\theta_{\text{low}}) - \cos(\theta_{\text{up}})\right)} \times \frac{\sum_k \omega_k^E \omega_k^R}{n_{\text{thrown}} dE} \tag{4.1}$$

  where w^{E} denotes the energy event weight, related to the gamma-ray simulated spectrum, w^{R} denotes the radius weight, n_{thrown} the number of simulated events, and the sum k runs over the selected events after cut, per energy bin dE.

- **Angular Resolution**:

  The angular resolution represents the accuracy of reconstructing the direction of the incident gamma-ray. It depends on the true energy of the photons and the zenith angle. Assumed to be radially symmetric, it is closely related to the Point Spread Function (PSF) of the analyzed event.

  The PSF is calculated by binning the reconstructed events into zenith bands and determining the difference between the true and reconstructed positions, $\theta = |X_{\text{true}} - X_{\text{reco}}|$, as a function of E_{true}. The PSF is then normalized along the θ axis for each zenith and energy bin, ensuring that the resulting quantity represents a probability. Then, the radius of the PSF will represent the angular resolution of the detector.

- **Energy Resolution**:

  The energy resolution represents how well the detector can reconstruct the true energy of a given event. It is represented as a 2D histogram of the events with true energy E_{MC} reconstructed as events with energy E_{R}.

  Another way to assess reconstruction quality is through the Energy Bias, which quantifies the difference between the reconstructed energy and the true (Monte Carlo) energy in logarithmic space (per energy bin), defined as the mean of the following Δ distribution:

$$\Delta = \log_{10}\left(\frac{E_R}{\text{GeV}}\right) - \log_{10}\left(\frac{E_{MC}}{\text{GeV}}\right) \tag{4.2}$$

  The energy resolution can also be represented as half the difference between the 15.9 % percentile and the 84.1 % percentile of the energy bias distribution.

- **Background Rejection**:

  Represents the expected remaining hadronic background after gamma/hadron separation due to misclassified events. To evaluate this rejection performance, it is necessary to examine the background rejection through the proton efficiency $\epsilon_p = N_{(Reco\_p)}/N_{(MC\_p)}$ (false positive rate) as a function of energy for a fixed gamma efficiency (true positive rate) of $\epsilon_\gamma = 80\,\%$.

  It is important to notice that the background rate is not derived from the gamma-ray simulations but for the hadronic ones, and the procedure to estimate this rate is analogous to the one followed to estimate the expected counts from a gamma-ray source.

- **Sensitivity**:

  The differential sensitivity of a gamma-ray observatory defines the minimum flux required for a statistically significant detection of gamma-ray events over the hadronic background. Sensitivity is a crucial metric as it directly impacts the ability to observe faint astrophysical sources.

  The sensitivity of SWGO to Dark Matter annihilation or decay can be found by comparing the number of observable gamma rays with the expected background. This residual background is essentially composed of protons that are misidentified as gamma rays. The statistical tool used to derive limits is a 4D (energy and space) joint-likelihood method, where the comparisons between DM and background fluxes are performed in different energy and spatial bins [59]. The number of observable gamma-ray events by a detector is computed by folding the considered gamma-ray flux with the IRFs, then, the expected signal in a spatial region of interest i and an energy bin j will be given by

$$S_{ij} = T_{\text{obs}} \int_{\Delta E_j} d\hat{E} \int_0^\infty dE \frac{d\Phi_\gamma(\Delta\Omega_i, E)}{dE} \times A_{\text{eff}}(E) \times \text{PDF}(E, \hat{E}) \tag{4.3}$$

where T_{obs} is the observation time, E is the true energy of the primary particle, $\hat{E}$ is the reconstructed energy of the primary particle, A_{eff} is the detector's effective area, $PDF(E, \hat{E})$ represents the energy resolution as a probability density function $P(\hat{E}|E)$, which describes the likelihood of observing an event with reconstructed energy $\hat{E}$ given a true energy E, and $d\Phi/dE$ is the DM produced gamma ray flux, which is calculated using equations 2.14 and 2.15 as seen on previous chapters.

Assuming that the number of detected events follows a Poisson distribution, the likelihood functions can be calculated in each individual bin and then be combined into an unique joint likelihood function:

$$\mathcal{L}(M_{\mathrm{DM}}, \langle\sigma v\rangle \vee \tau_{\mathrm{DM}}) = \prod_{ij} \mathcal{L}_{ij} \tag{4.4}$$

with

$$\mathcal{L}_{ij} = \frac{(B_{ij} + S_{ij})^{N_{ij}} \exp(-B_{ij} + S_{ij})}{N_{ij}!} \tag{4.5}$$

where N_{ij} is the total number of observed events and B_{ij} is the number of detected background events.

Using this information and applying the 'Log-likelihood Ratio Test', it is possible to derive constraints for $\langle\sigma v\rangle$ or (τ_{DM}) as follows

$$TS = -\ln\left(\frac{\mathcal{L}_0(M_{\mathrm{DM}}, \langle\sigma v\rangle \mid \tau_{\mathrm{DM}})}{\mathcal{L}_{\mathrm{máx}}(M_{\mathrm{DM}}, \langle\sigma v\rangle \mid \tau_{\mathrm{DM}})}\right) \tag{4.6}$$

where $\mathcal{L}_0$ represents the hypothesis with no DM presence, and $\mathcal{L}_{max}$ represents the hypothesis with DM presence [38]. This function is evaluated at the cross-section (or decay time) values that maximize it.

Finally, we can compute the overall performance of a detector unit or array layout by evaluating the flux sensitivity to a steady point source. For the SWGO simulations, the collaboration picked a source at a declination of -20deg with the detector placed at the current selected location on Pampa La Bola, then calculated the sensitivity for 1 year of observations to a source with a power-law energy spectrum with an index of -2, and a reference flux of $1 \times 10^{-11}\mathrm{TeV}^{-1}\mathrm{cm}^{-2}\mathrm{s}^{-1}$ at 1 TeV.

5 Gamma-ray spectra from Dark Matter annihilation

To generate atmospheric showers using CORSIKA, a set of parameters must be provided to define the initial conditions of the shower. These include the type of primary particle (photon or proton in our case), the energy range in which it will be generated, and the zenith and azimuthal angle ranges according to the coordinate system mentioned above.

However, one of the most crucial parameters is the spectral index, which is directly related to the cosmic-ray or gamma-ray spectrum that will generate the primary particles. As shown in **Figure 2.1**, this spectrum generally follows a power-law behavior:

$$\frac{d\Phi}{dE} = AE^{-\gamma} \tag{5.1}$$

where the energy exponent, γ, is the spectral index that must be specified in CORSIKA.

In this work, we aim to evaluate the detector's sensitivity to a gamma-ray flux produced by Dark Matter annihilation in the Galactic Center. Therefore, CORSIKA must be configured to generate particles following a spectrum that meets these characteristics. The most direct way to achieve this is by defining the spectral index of the gamma-ray flux. Thus, the first step in our study was to generate this spectrum, using previously generated events produced using the Monte Carlo software PYTHIA.

PYTHIA is a general purpose Monte Carlo event generator in high-energy physics [60]. Its primary focus is on multiparticle production in collisions between elementary particles. The software aims to accurately represent fundamental properties across a wide range of processes and reactions, both within and beyond the Standard Model.

The program includes theoretical models for various physics aspects, such as total and partial cross sections, hard and soft interactions, parton distributions, initial- and final-state parton showers, matching and merging of matrix elements with showers, multiparton interactions, hadronization/fragmentation, and decays.

The event simulations used in this work were generated within the PYTHIA 6.4 framework. These simulations include annihilation processes for various Dark Matter masses and all possible annihilation channels within the Standard Model.

The output files contain information such as the collision energy, the total number of generated particles, and the photon differential spectra per energy bin. From this data, we can build our full gamma-ray spectrum.

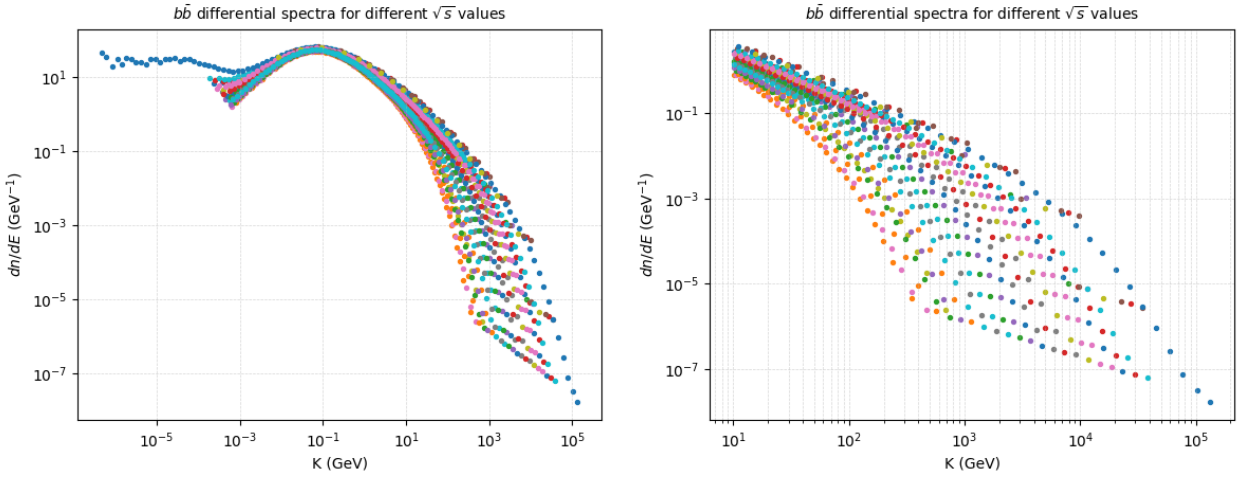

Figure 5.1 – Differential gamma ray spectra for the $b\bar{b}$ annihilation channel. Left panel shows the full Pythia simulated spectra for different DM masses, while the right panel shows these spectra for the SWGO energy range.

Figure 5.1 illustrates the first step of the process. The left panel displays the differential spectra for the $b\bar{b}$ annihilation channel across the full energy range for different collision energies. Essentially, this plot represents the number of gamma rays per energy bin produced by decays in the selected channel that will eventually reach the Earth's atmosphere.

However, SWGO will not be able to detect gamma rays over the entire energy range, so a data cut is necessary. The right panel of **Figure 5.1** shows this cut. Theoretically, SWGO will be capable of detecting gamma rays from hundreds of GeV to the PeV scale [59]. To obtain a more representative spectrum, we consider only data points within the range of 10 GeV – 1 PeV. An important detail is that the lower limit was set to 1 GeV due to the lack of simulated PYTHIA events at higher energies (this is especially troublesome for other annihilation channels), which could affect the overall behavior of the full spectrum.

To determine the spectral index of each spectrum, we take advantage of the power-law nature of the flux (**Equation 5.1**). Since we plot the logarithmic form of this expression, we are essentially representing an equation of the form:

$$\log(\frac{dn}{dE}) = \log(A) - \gamma \log(E) \tag{5.2}$$

This expression corresponds to a linear equation. Therefore, to obtain the spectral index, we simply need to determine the slope of each individual spectrum.

$$\gamma = \frac{(dn/dE)_2 - (dn/dE)_1}{E_2 - E_1} \tag{5.3}$$

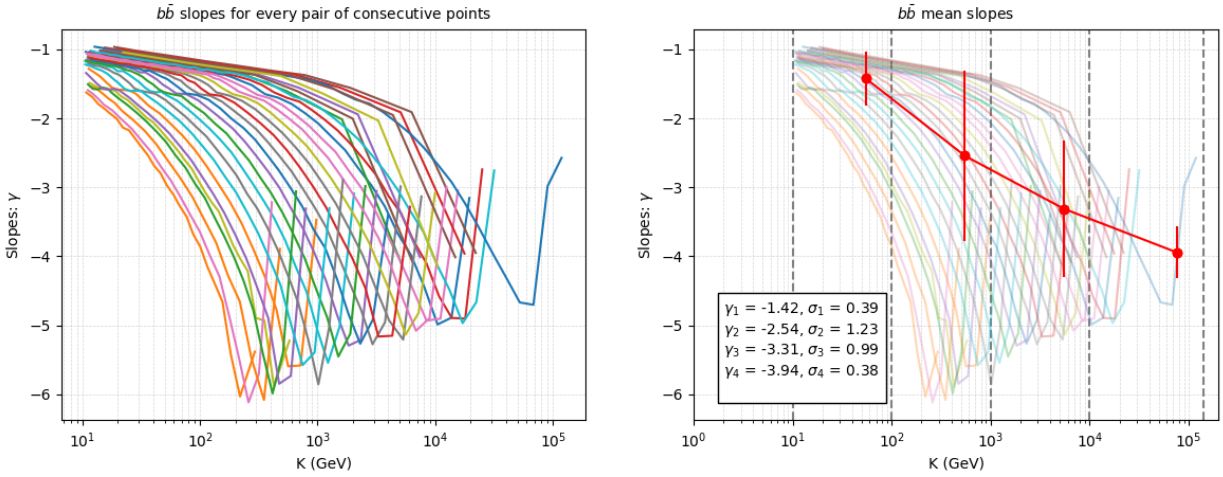

Figure 5.2 – Left: Slopes for each pair of consecutive points in every spectrum plotted against the energy. Right: Segmented energy intervals with the mean slope for each segment.

The next step was to obtain these slopes for every spectrum in every annihilation channel. In order to do that we calculated the slope for each pair of consecutive data points and proceeded to plot it against the energy range, as shown in **Figure 5.2**.

The left panel of **Figure 5.2** illustrates these calculated slopes. For the $b\bar{b}$ annihilation channel, we observe significant variations with energy. To account for this, we divided the energy range into smaller sub-intervals and calculated the mean slope within each, as shown in the right panel of **Figure 5.2**.

These steps were then performed over all the remaining 11 annihilation channels, with the aim of collecting these mean slopes for every channel in each energy interval.

Table 5.1 shows the list of all the calculated mean slopes, and on the following page, the full process is shown for the two other most common annihilation channels.

Energy (GeV)	**Mean Slopes**: γ											
	$b\bar{b}$	$u\bar{u}$	$t\bar{t}$	$s\bar{s}$	$c\bar{c}$	$d\bar{d}$	e^-e^+	$\tau^-\tau^+$	$\mu^-\mu^+$	W^+W^-	ZZ	gg
$10^1 - 10^2$	-1.42	-1.42	-1.49	-1.41	-1.41	-1.42	-0.99	-0.70	-1.01	-0.88	-0.91	-1.59
$10^2 - 10^3$	-2.54	-2.22	-2.58	-2.50	-2.36	-2.30	-1.09	-1.14	-1.12	-2.01	-2.09	-2.91
$10^3 - 10^4$	-3.31	-2.93	-3.76	-3.47	-2.92	-3.27	-1.21	-1.82	-1.26	-3.28	-3.38	-4.37
$10^4 - 10^5$	-3.94	-3.49	-4.79	-4.28	-3.12	-4.20	-1.41	-2.43	-1.38	-4.33	-4.47	-5.10
$10^5 - 10^6$	---	---	---	---	---	---	-1.54	-3.38	-1.57	-5.87	-5.99	---

Table 5.1 – Segmented mean slopes for every annihilation channels.

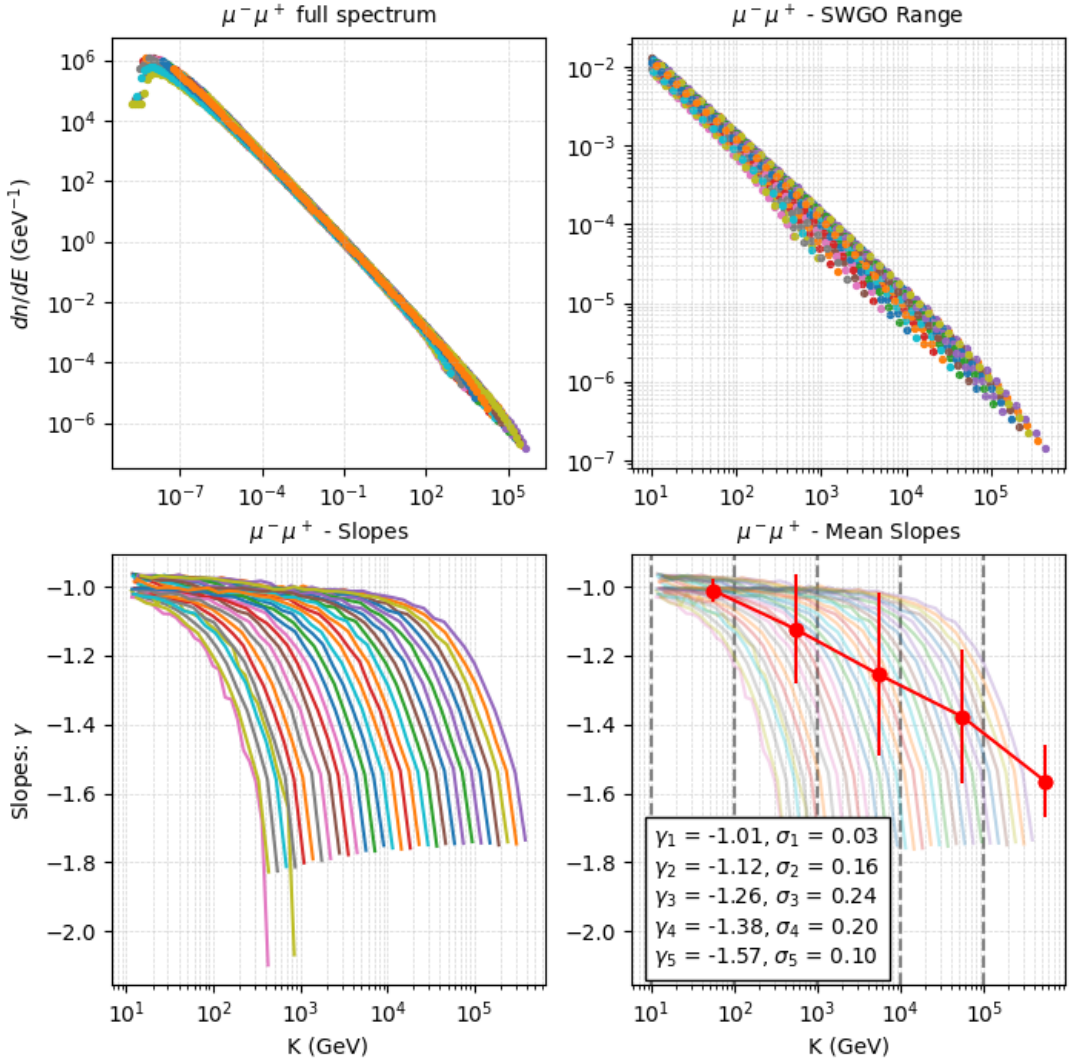

Figure 5.3 – Gamma-ray differential spectrum from the $\mu^-\mu^+$ annihilation channel. Full process of the mean slopes calculation.

The $\mu^-\mu^+$ spectrum exhibits a smooth power-law behavior, with an almost constant slope, this is primarily driven by bremsstrahlung radiation from the final-state muons [61]. Since muons do not hadronize, the energy distribution of secondary photons follows a continuous falloff without significant spectral features or enhancements at specific energies.

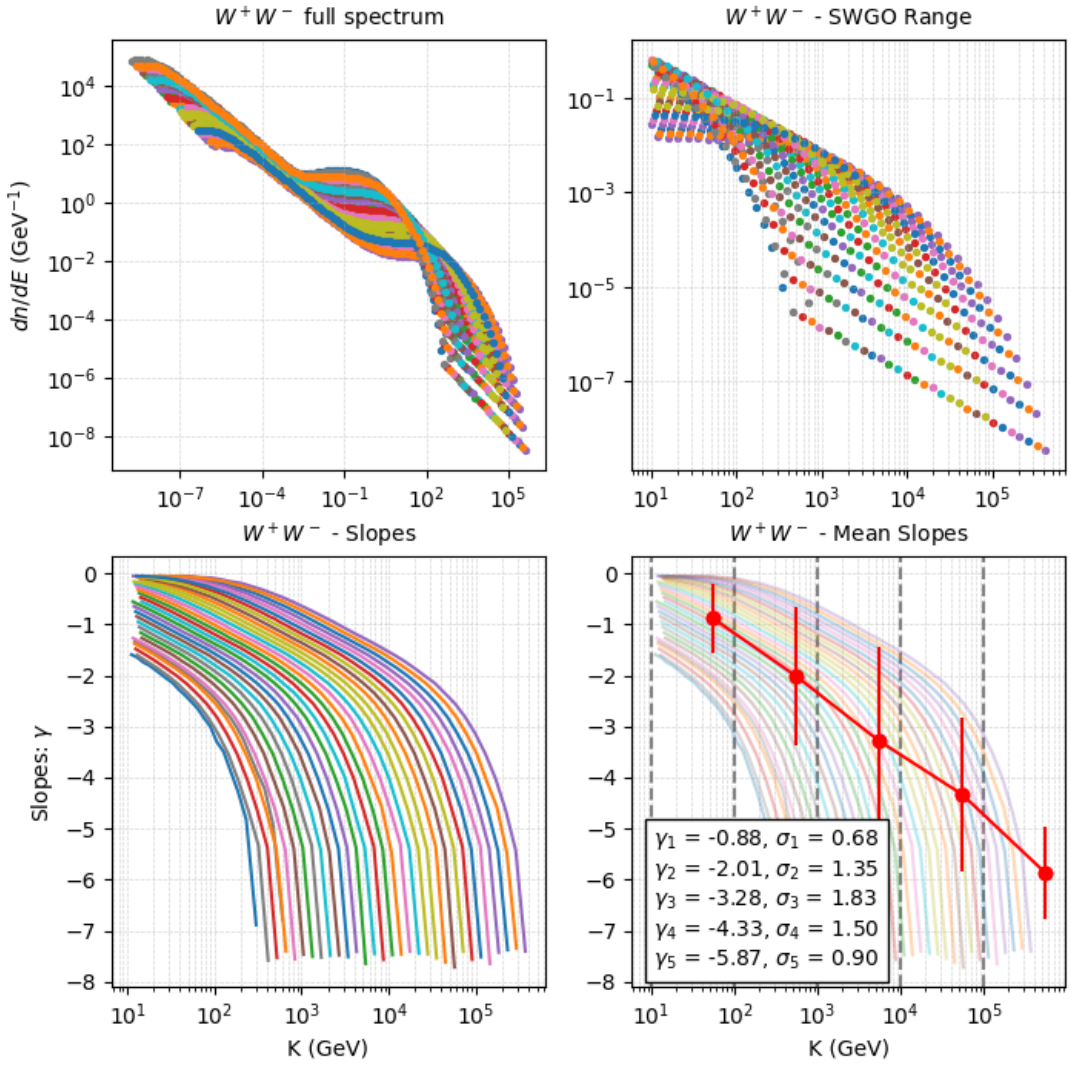

Figure 5.4 – Gamma-ray differential spectrum from the W^+W^- annihilation channel. Full process of the mean slopes calculation.

Unlike the previous case, the W^+W^- spectrum shows deviations from a pure power law, including a characteristic 'bump' around 10^{-1} GeV. This feature likely originates from hadronic decays of the W bosons, which produce neutral pions (π^0) that subsequently decay into photon pairs [35]. The presence of multiple decay channels results in a more complex spectral shape with additional energy redistribution compared to that of the muon channel.

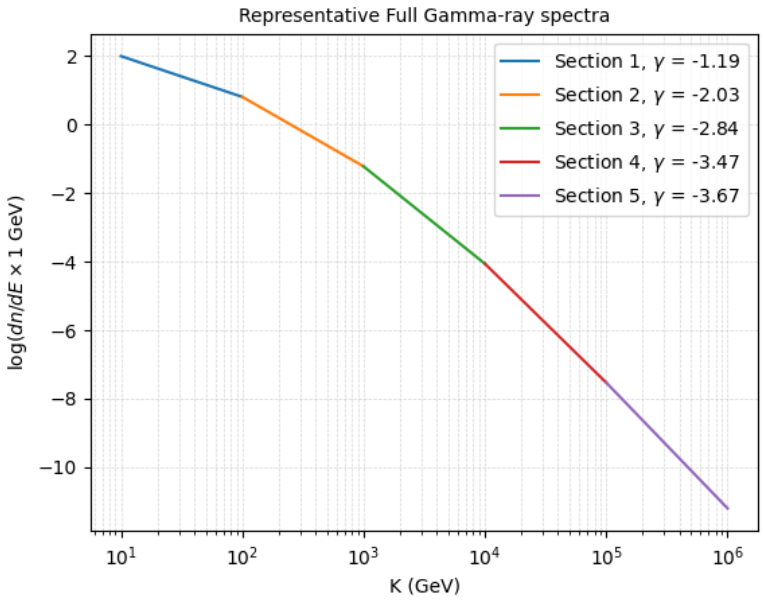

Figure 5.5 – Full gamma-ray spectrum constructed using the mean slopes of each energy segment. This representative curve is intended to generate a more precise set of simulation files.

The final step involves using the mean slopes per energy range, calculated for each annihilation channel, to construct the full gamma-ray spectrum based on the global mean slope of each energy segment. To achieve this, we plotted straight lines with the corresponding slopes for each segment, as shown in **Figure 5.5.**

At the time of this study, SWGO had performed 2000 CORSIKA gamma-ray runs for the D8 detector configuration, each containing 50000 events, all with a spectral index of -2.00. This amounts to a total of 10^8 gamma-ray showers simulated by the collaboration. Since our analysis considers a dark matter-produced gamma-ray spectrum with different slopes across energy segments, we opted to generate our CORSIKA simulations in batches corresponding to these energy segments.

To better characterize this spectrum and its power-law behavior in the simulations, we integrated this curve to estimate the number of events per energy bin and obtained the normalized number of events in each segment. These percentages allowed us to refine our segmented CORSIKA input files for greater precision.

Finally, using these parameters, we simulated approximately 20 million gamma rays, distributed across 621 simulation files, with the number of events per file distributed as follows

Energy (GeV)	**Number of Files**	**Number of Photons**	**Spectral Index**	%
$10^1 - 10^2$	300	15×10^6	-1.19	70
$10^2 - 10^3$	106	$5{,}3 \times 10^6$	-2.03	24
$10^3 - 10^4$	95	$9{,}5 \times 10^5$	-2.84	4
$10^4 - 10^5$	70	$7{,}0 \times 10^4$	-3.47	0.3
$10^5 - 10^6$	50	10^3	-3.67	0.002

Table 5.2 – Total number of gamma rays distributed over their corresponding number of simulation files and spectral index for each energy segment.

6 Performance Evaluation and Discussion of Results

All the Instrument Response Functions shown in this chapter are **preliminary results**, pending the generation of additional simulations to significantly increase the number of reconstructed events. The high computational cost in the later stages of the reconstruction chain presents the greatest challenge to obtaining a more robust statistical sample.

Effective Area

Figure 6.1 illustrates the comparison between the effective area curves, showing a similar collection area on the detector array for **our simulations** (labeled as `D8`) at low energies, compared to the preliminary **results of the collaboration** (labeled as `D8_SWGO`), both exhibiting a characteristic rise with the energy of the primary gamma rays.

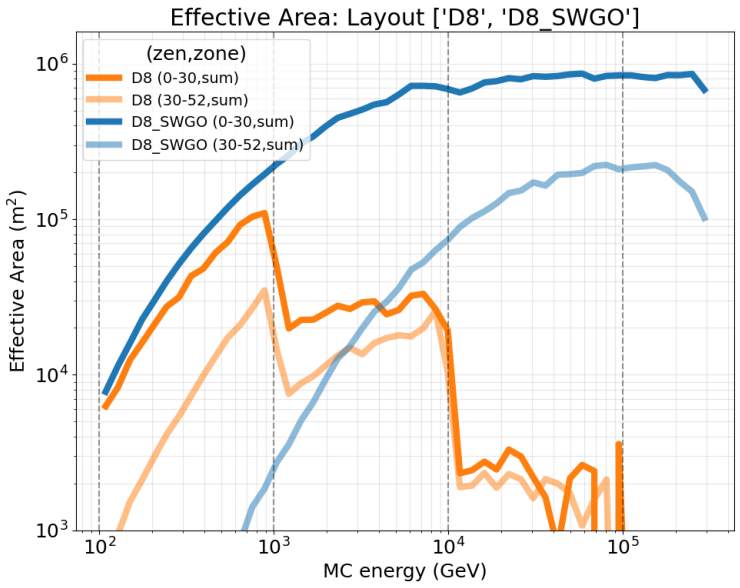

Figure 6.1 – Effective area as a function of MC (true) energy for both datasets `D8` and `D8_SWGO`. The collaboration dataset was obtained from shower simulations with an spectral index of -2 across the full energy range. Results are shown for two zenith angle ranges: 0-30° and 30-52°. The curves are constructed as the total signal measured in the three radial zones (see table **3.1**).

The dashed lines indicate the lower and upper limits of the predefined energy segments used to generate the CORSIKA simulations. We observe that the overall behavior within each energy segment of our function closely matches the general behavior of that calculated by the collaboration. However, at these energy limits, a drop in the effective area curve for the `D8` configuration is noticeable.

This drop is likely due to a normalization issue. Upon further inspection of the reconstruction chain, in Equation 4.1, which defines this IRF:

$$A_{\text{eff}}(E) = \frac{1}{2\pi\left(\cos(\theta_{\text{low}}) - \cos(\theta_{\text{up}})\right)} \times \frac{\sum_k \omega_k^E \omega_k^R}{n_{\text{thrown}} dE}$$

we see that the reconstructed energy and core location are represented by the weight functions ω_k^E and ω_k^R, respectively. Since the distribution of the events in the XY plane (r-distribution) is not physical, we expect more events at large r than at small r simply due to the greater phase space available. However, events are drawn from a flat r-distribution, artificially increasing the number of events generated near the detector. Additionally, the energy bias arises from the spectral index of the energy distribution.

These weights are applied to the simulated events to model the physical fluxes of particles, effectively correcting the biases introduced during simulation generation. The weights are calculated according to [62] as follows

$$w(E, r) = \frac{2\pi^2}{N_{\text{thrown}}}(R_f - R_i)\left(\frac{1}{E_i} - \frac{1}{E_f}\right) \cdot (\cos^2\theta_i - \cos^2\theta_f)\, r\, E^2 \tag{6.1}$$

This function accounts for both the position and energy bias, with particular importance given to the energy bias, which appears as E^2 in **Equation 6.1**, directly related to the spectral power-law.

For the SWGO effective area, all simulation files share the same initial parameters (except for some random seed variations), using a spectral index of -2 across the entire energy range. In contrast, our simulation files are generated in batches, each with a different spectral index per energy range, and the reconstructed events are combined in the final stages of the reconstruction chain. As a result, our effective area curve has a varying normalization depending on the energy interval, explaining the drop at the first energy limit near 10^3. It is important to note that in the $10^2 - 10^3$ GeV energy interval, our calculated mean slope is -2.03, making this segment the most similar in shape to the SWGO function.

The calculation of these weights is hard-coded into the HAWCSim package, making it unclear how to compensate for these normalization differences. This issue primarily arises from our simulation methodology, where we independently simulate all showers, detector responses, and reconstruction according to energy segments and later combine all files for the IRFs generation step, as required for training the classification MLPs. Further work is needed to achieve a more accurate representation of the effective area curve.

Finally, it is also worth discussing the irregularities in the curve that appear at high energies. These could be explained by a lack of statistics due to the low number of simulated high-energy events and the even lower number of reconstructed events in these energy ranges. This issue will be examined in more detail in the next set of IRFs.

Energy Resolution

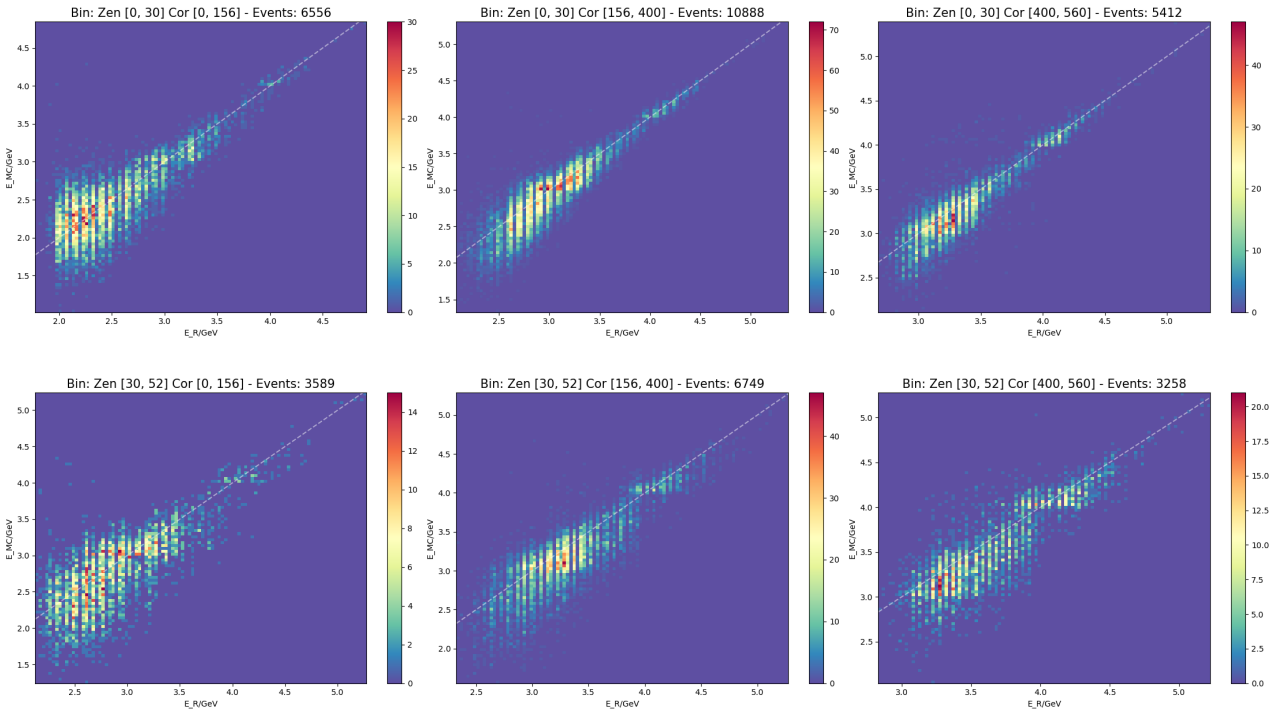

Figure 6.2 – Energy resolution for different zenith angle and core distance bins for our simulations `D8`. The top row corresponds to zenith angles in the range 0-30°, while the bottom row represents 30-52°. Each panel shows a different core distance bin, where each bin corresponds to the radius (m) of one of the zones in the detector array, with the number of events indicated. The color scale represents event density, highlighting the distribution and deviations from the diagonal (ideal reconstruction).

Figure 6.2 shows the Energy Resolution as a 2D histogram for each zenith and core bin, illustrating the quality of energy reconstruction in these bins. Compared to the reconstruction of the collaboration data shown in Figure 6.3, we observe that our reconstruction is sufficiently accurate across all bins. This confirms that the previously defined reconstruction algorithms (3.2) correctly characterize the energy of our simulated primary particles.

For comparisons between detectors, SWGO generally considers only the reconstructed events in the low zenith range (0–30°), assuming that most showers originate directly above the detector array. The first key distinction between these two sets of plots is the zenith binning. In our simulations, we considered only two bins: the low zenith bin (0–30°) and the high zenith bin (30–52°), whereas the collaboration used three bins. The election of this binning scheme for our simulations is a consequence of the low number of reconstructed events in certain energy/core/zenith regions, giving a very low number of points to plot , hence the selection of this binning structure.

In both cases, the number of reconstructed events after selection cuts decreases as the zenith angle increases. Due to our limited statistics, we cannot afford to divide the data into three bins, which is the reason for this difference. This reduction in reconstructed events with increasing zenith angle is expected, as a greater number of secondary particles miss detectors at larger zenith angles.

We observe a higher density of events at low energies, correctly reflecting the behavior of the simulated spectrum. Since our simulations are performed in separate energy segments, the number of events in each of the energy resolution plots appear less uniform as energy increases compared to the SWGO plots. However, they still preserve the fundamental characteristic of the power-law spectrum: fewer events at higher energies.

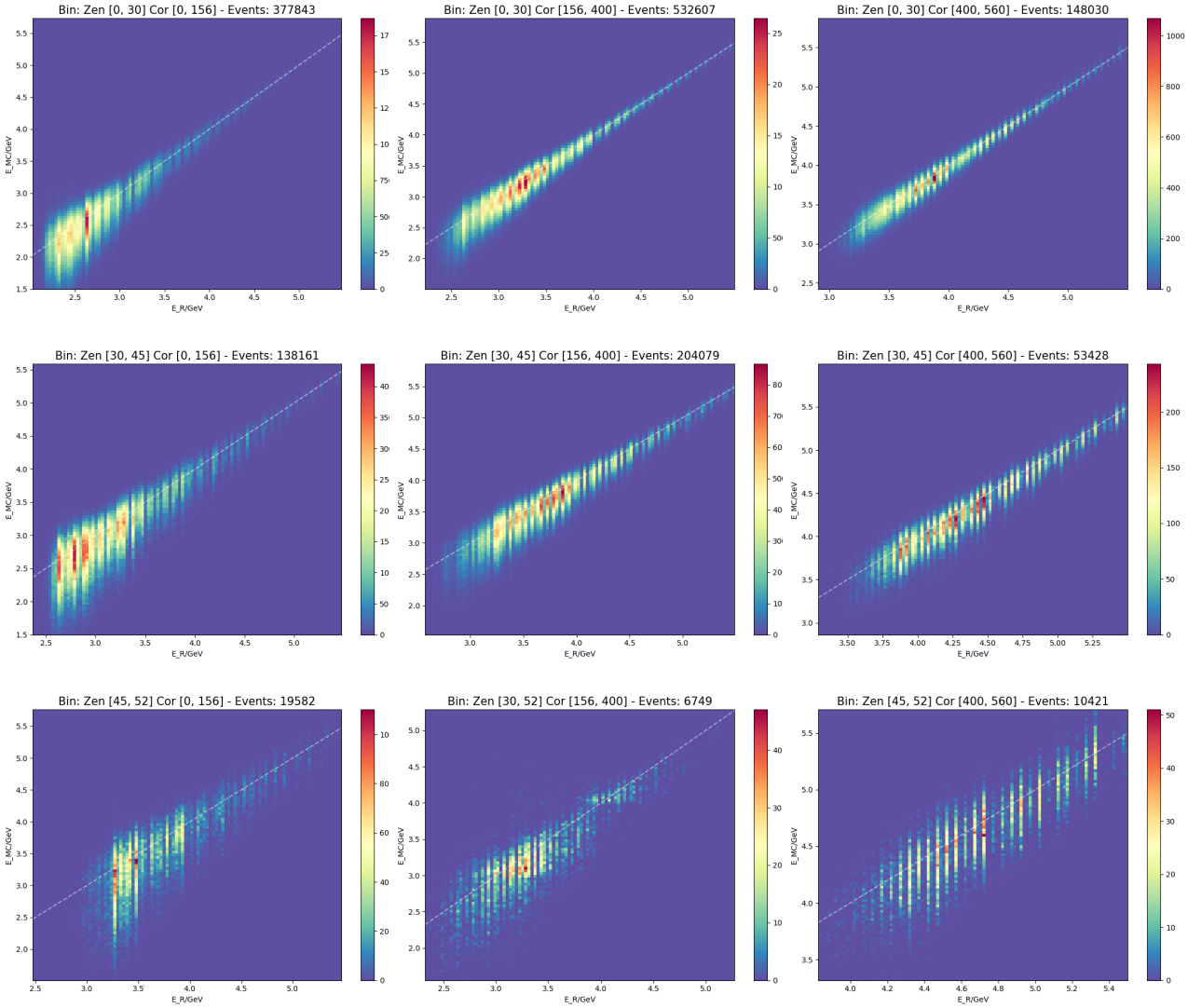

Figure 6.3 – Energy resolution for different zenith angle and core distance bins for the collaboration simulations `D8_SWGO`. The top row corresponds to zenith angles in the range 0-30°, the middle row is for the intermediate zenith bin at 30-45°, while the bottom row represents 45-52°. Each panel shows a different core distance bin, with the number of events indicated. The color scale represents event density, highlighting the distribution and deviations from the diagonal (ideal reconstruction).

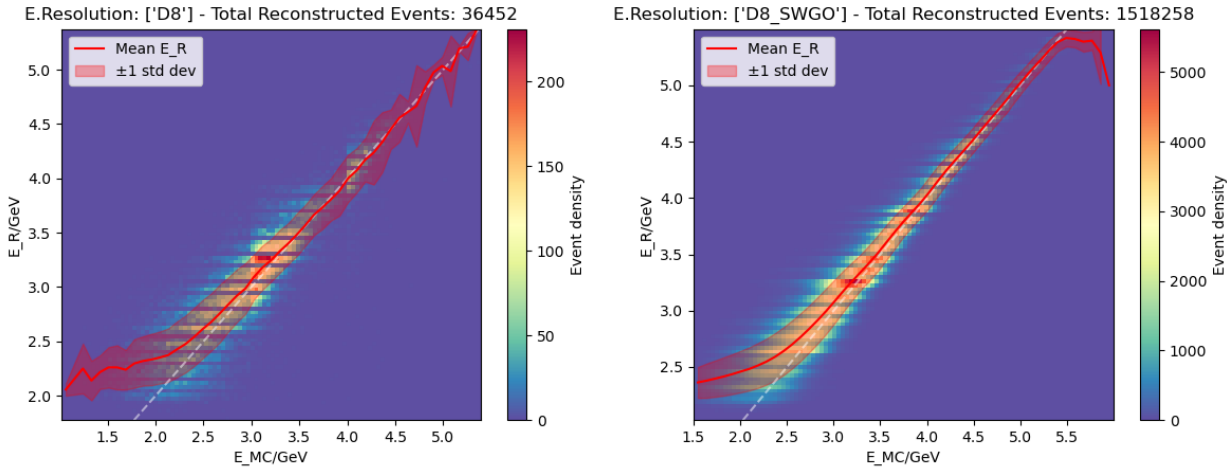

Figure 6.4 – Energy Resolution for both the `D8` (our simulations) and `D8_SWGO` (collaboration) datasets. Including the total reconstructed events in all bins. The red line corresponds to the mean reconstructed energy with respect to the corresponding true energy, intended to show a more clear representation of the deviation with respect to the ideal reconstruction white dashed line.

It is evident from Figure 6.4 that the number of reconstructed events remaining after selection cuts in our dataset is significantly lower than in the collaboration's dataset. This discrepancy is reflected in our limited statistics across most of the plots in this chapter. For SWGO, only $\sim 1{,}5\,\%$ of the reconstructed events survived after selection cuts, whereas in our case, the percentage is even lower, at $\sim 0{,}17\,\%$ due to the different initial sample of simulated events. This highlights the need to increase the number of gamma-ray simulations to obtain more robust statistics. Nonetheless, Figure 6.4 and the Energy Bias in Figure 6.5 exhibit nearly the same behavior for the reconstructed events with respect to the collaboration simulations.

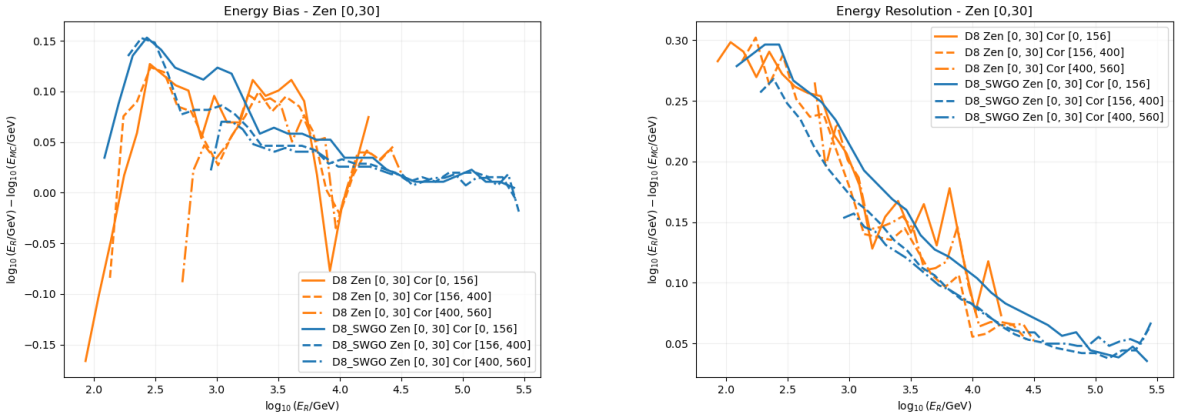

Figure 6.5 – Comparison of energy bias (left) and energy resolution (right) as a function of reconstructed energy (E_R) for both datasets. The energy bias plot (left) shows the systematic deviation between reconstructed and true energy, while the energy resolution plot (right) illustrates the statistical spread in energy reconstruction.

Angular Resolution

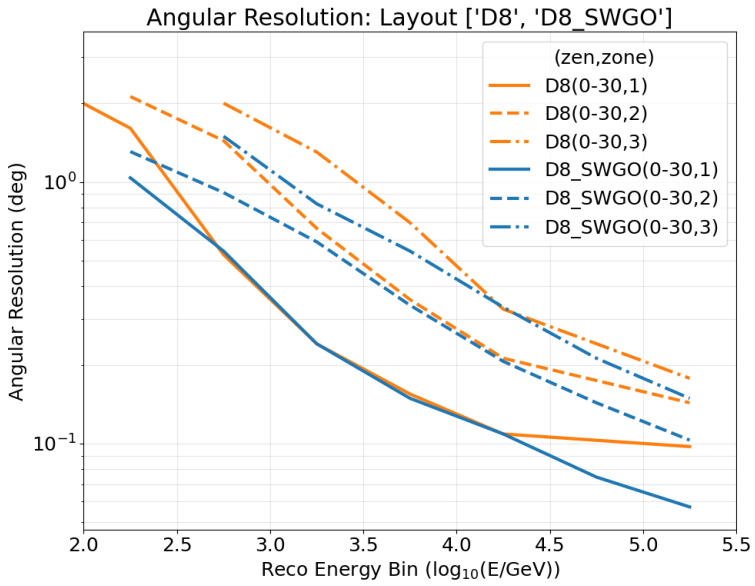

Figure 6.6 – Comparison of angular resolution between `D8` (orange) and `D8_SWGO` (blue) for each core location bin as a function of reconstructed energy. Comparison is performed only in the low zenith bin due to the difference in our binning scheme previously mentioned.

Direct comparison of angular resolution between the `D8` and `D8_SWGO` datasets reveals a consistent trend: `D8_SWGO` exhibits superior angular resolution across most of the energy ranges and core zones.

One of the most significant factors influencing the observed resolution differences is the number of simulated and successfully reconstructed events in each dataset. A higher number of reconstructed events in SWGO contributes to more robust statistical sampling, reducing fluctuations and biases in the angular resolution estimation. In contrast, the significantly lower number of reconstructed events in D8 can lead to larger statistical uncertainties, especially in energy ranges where event statistics are limited.

Another key difference between the two datasets is the energy distribution of the simulated gamma-ray showers. The fixed spectral index of -2 in the SWGO simulations ensures a higher proportion of high-energy events compared to our dataset, where the spectral index in the final energy segments is as steep as -3.67. Since angular resolution generally improves with increasing energy, behavior that replicates in both datasets, a dataset enriched in high-energy events (such as SWGO) is expected to exhibit better average angular resolution. If the spectral index in `D8` is steeper in certain energy ranges, this also implies a higher fraction of low-energy events, where shower development is weaker, leading to fewer detected signals in the Water Cherenkov Detectors. This naturally degrades the accuracy of the direction reconstruction, making it more difficult to achieve precise angular resolution, particularly in the outer core regions where detector density is lower.

Background Rejection

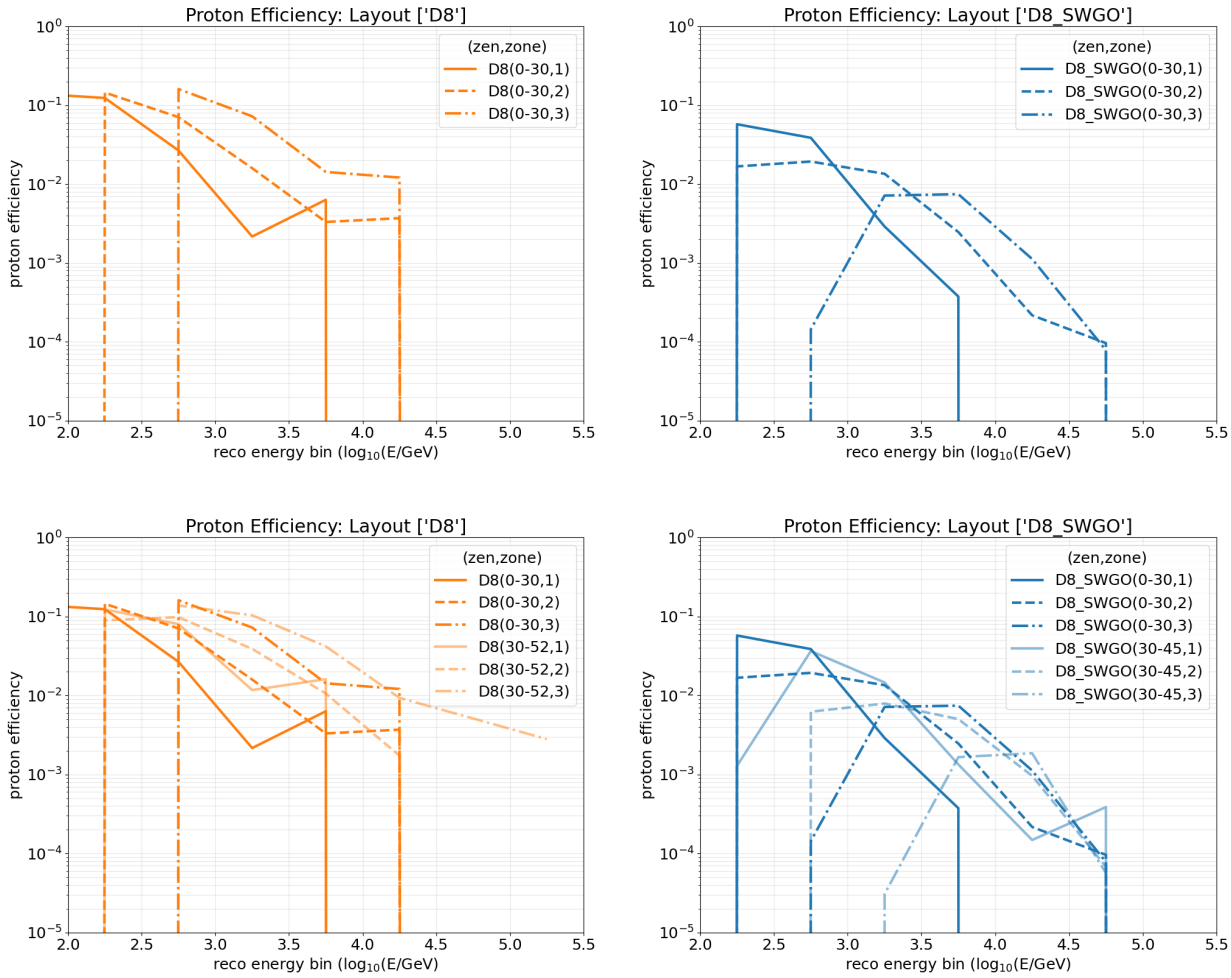

Figure 6.7 – Comparison of proton efficiency between `D8` and `D8_SWGO` as a function of reconstructed energy across different core regions of the detector. `D8` exhibits consistently higher values of proton efficiency, indicating weaker background rejection compared to the SWGO dataset.

Figure 6.7 compares the proton efficiency as a function of reconstructed energy between `D8` and `D8_SWGO` across different core regions of the detector. The results indicate a significant difference in proton rejection between the two datasets.

The general trend observed in both datasets is a decrease in proton efficiency with increasing energy, which aligns with expectations. At higher energies, gamma-ray showers exhibit more distinct electromagnetic characteristics, making it easier to separate them from hadronic backgrounds. However, there is a notable discrepancy between both datasets, with `D8` showing consistently higher proton efficiency (lower gamma efficiency), implying worse background rejection compared to the collaboration's results. This discrepancy is particularly pronounced at high energies.

The plots also highlight the impact of detector core regions on proton efficiency. In both datasets, proton efficiency increases from Zone 1 (the inner core with the highest density of WCDs) to Zone 3 (the outermost region with the lowest density). This behavior is expected, as a lower density of detectors results in reduced reconstruction accuracy, due to less detector activations per event, making it more challenging to differentiate gamma-ray showers from hadronic backgrounds. However, `D8_SWGO` maintains better background rejection across all core zones.

The lower set of plots extends the analysis to higher zenith angles (30-52° for our simulations and 30-45° for SWGO), showing that background rejection worsens at larger zenith angles in both scenarios. This is due to the increased path length through the atmosphere, which alters shower development and reduces the effectiveness of gamma/hadron separation. Despite this, `D8_SWGO` continues to demonstrate superior performance.

This result is sufficiently good, especially considering the significantly lower statistics in our simulations. This limitation becomes particularly evident at higher energies, where the presence of several empty bins makes the calculation of proton efficiency considerably more challenging. On average, our proton efficiency remains below 10 %.

Sensitivity

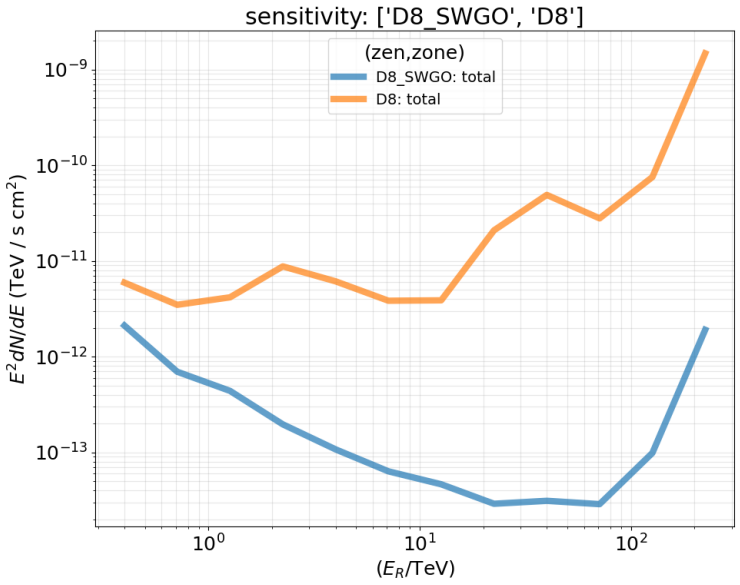

Figure 6.8 – Differential sensitivity as a function of reconstructed energy for the `D8` (orange) and `D8_SWGO` (blue) datasets. The `D8_SWGO` dataset, featuring a higher number of simulated events and a uniform spectral index (-2), achieves better sensitivity across all energy ranges, particularly at high energies.

The sensitivity was calculated assuming a steady point source at a declination of 20° with a flux of spectral index -2 at 1 TeV for both datasets. This setup shows a significant better sensitivity for the collaboration dataset across all energy ranges. This is evident from the systematically lower values of E^2dN/dE in the `D8_SWGO` curve. This difference can be attributed to the differences in energy reconstruction through the $PDF(E|\bar{E})$ and in the differences of the effective area.

The energy dependence of sensitivity further highlights the discrepancies between both datasets. At low energies (< 10 TeV), the sensitivity difference is moderate, suggesting that background rejection and reconstruction techniques are performing similarly in this regime. However, at higher energies, where the normalization issues on the effective area becomes more prominent (> 10 TeV), the gap between both configurations becomes more pronounced, with `D8` showing significantly worse sensitivity. This degradation can be also explained by a lower number of reconstructed high-energy events in our dataset due to the steep spectral indices chosen on this energy ranges.

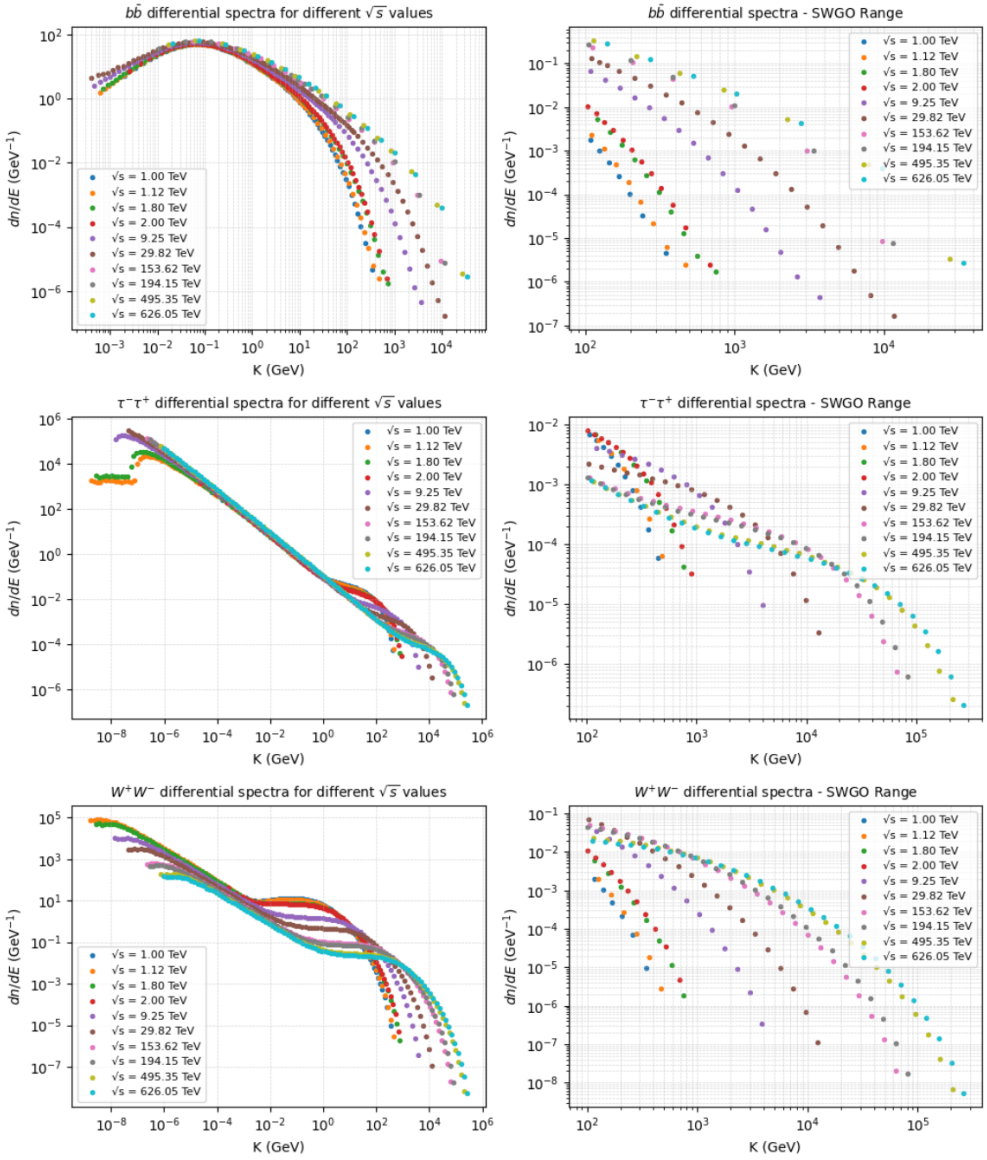

Figure 6.9 – Differential energy spectra (dn/dE) for dark matter annihilation into $b\bar{b}$, $\tau^-\tau^+$ and W^+W^- channels at different center-of-mass energies ($\sqrt{s}$). The left panels display the full spectra across multiple $\sqrt{s}$ values, illustrating the dependence of the spectral shape on the annihilation energy. The right panels focus on the energy range relevant to SWGO, highlighting the portion of the spectra that falls within the expected sensitivity range of the observatory.

Figure 6.9 shows a set of ten selected spectra, each with a different center-of-mass energy $\sqrt{s}$ for three annihilation channels. The left panels display the spectra over the full energy range simulated by Pythia, while the right panel shows the spectra restricted to the energy range observable by SWGO.

We aim to estimate the detector's sensitivity to these specific fluxes, so we need to obtain the annihilation flux function for these spectra with greater precision (equation 2.14). To achieve this, we apply a power-law fit with an exponential cutoff (equation 6.2) to account for the spectral drop at high energies. This fit is shown in Figure 6.10

$$y = AE^{-\gamma}e^{-E/\beta} \tag{6.2}$$

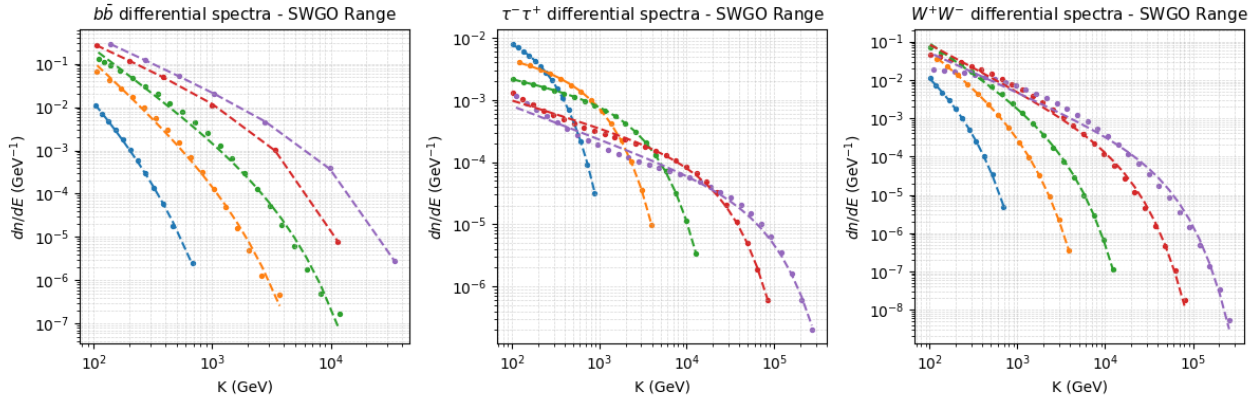

Figure 6.10 – Differential energy spectra (dn/dE) for dark matter annihilation into the three annihilation channels within the SWGO sensitivity range. Each curve corresponds to a different dark matter mass, with a power-law fit including an exponential cutoff (equation 6.2) overlaid as a dashed line. The fits capture the expected spectral shape, highlighting the suppression of high-energy components due to the cutoff behavior.

Next we use the fitted parameters A, γ and β (Table 6.1) to calculate the gamma-ray flux of these spectra using equation 2.14. In addition we need the astrophysical parameters *J-factor* and solid angle $\Delta\Omega$ for the inner 10° in the galactic center, values that are directly taken from Table **2.1** assuming an Einasto profile, while for the physical parameters we use the values of M_{DM} respective to the selected spectrum and the thermal relic cross-section $\langle\sigma v\rangle = 3 \times 10^{-26}\text{cm}^3/\text{s}$.

$b\bar{b}$			$\tau^-\tau^+$			W^+W^-		
A	γ	β	A	γ	β	A	γ	β
$1{,}47 \times 10^{5}$	-3.71	136.83	$8{,}77 \times 10^{-3}$	-0.29	64.99	$8{,}33 \times 10^{-1}$	-0.81	52.18
$8{,}11 \times 10^{3}$	-2.78	177.86	$1{,}95 \times 10^{-2}$	-0.05	146.16	$3{,}44 \times 10^{1}$	-1.58	129.85
$2{,}37 \times 10^{3}$	-2.00	2176.02	$8{,}73 \times 10^{-3}$	-0.30	2527.13	$9{,}80 \times 10^{1}$	-1.51	1921.02
$7{,}92 \times 10^{1}$	-1.23	2054.65	$6{,}77 \times 10^{-3}$	-0.41	14525.96	$2{,}91 \times 10^{1}$	-1.25	8505.45
$1{,}22 \times 10^{2}$	-1.24	5899.53	$8{,}46 \times 10^{-3}$	-0.51	69128.61	$8{,}48 \times 10^{0}$	-1.08	30458.83

Table 6.1 – Fit parameters for Figure 6.10. $M_{DM} =\sim 1, 5, 15, 100, 250$ TeV respectively.

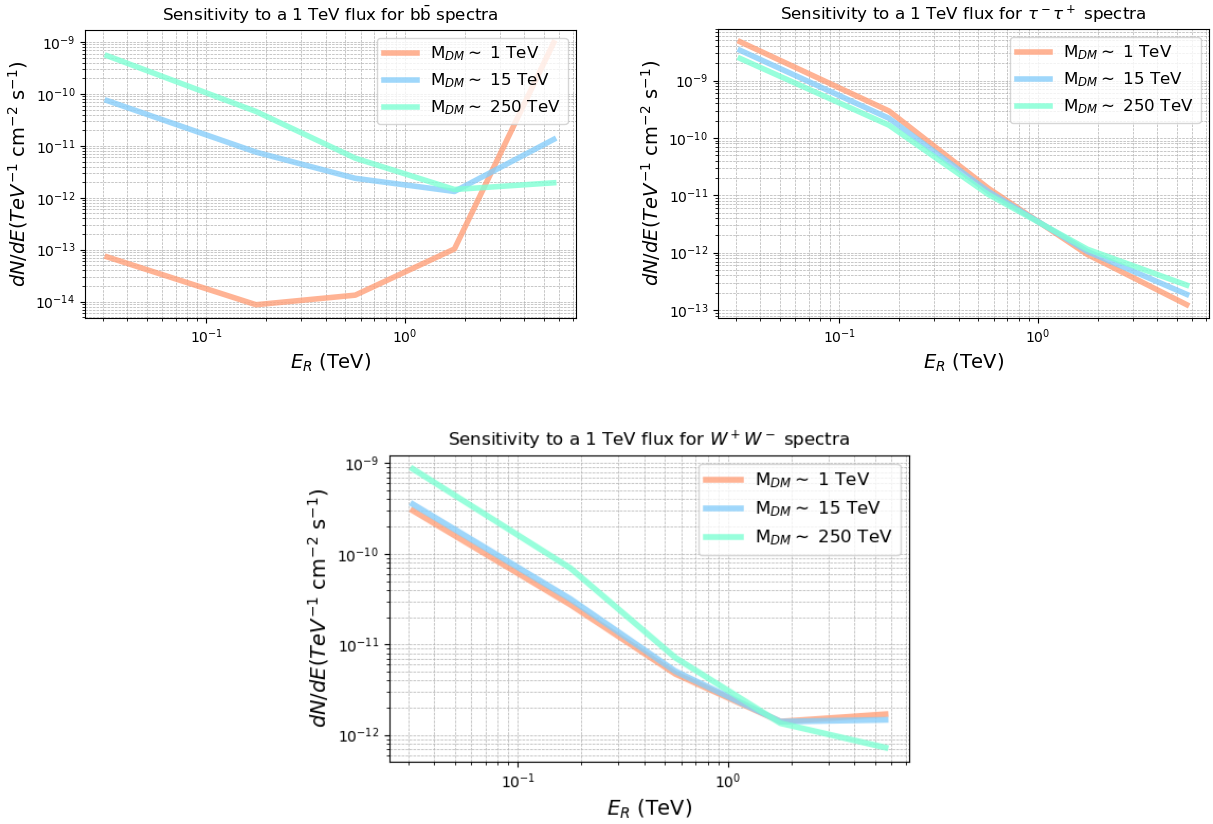

Figure 6.11 – Sensitivity estimates for detecting gamma-ray signals from dark matter annihilation into $b\bar{b}$, $\tau^-\tau^+$ and W^+W^- channels. The plots show the expected flux differential dN/dE as a function of the reconstructed energy E_R for different dark matter masses ($M_{DM} = 1, 15, 250$ TeV).

Figure 6.11 shows the sensitivity of our detector to gamma rays specifically produced by one of the DM spectra generated in the previous chapter. Each panel represents the sensitivity to the differential photon flux $\frac{dN}{dE}$ as a function of the reconstructed energy (E_R), considering a reference flux normalized to 1 TeV. We analyze the sensitivity specifically in three annihilation channels, each of these, representative of their particle type, and for different dark matter masses. The curves in different colors correspond to various values of dark matter mass M_{DM} (1 TeV, 15 TeV, 250 TeV). The shape of these curves illustrates how sensitivity varies depending on the dark matter particle mass and the annihilation channel. Each annihilation channel produces a distinct gamma-ray spectrum due to differences in secondary particle production.

The top left panel shows the sensitivity for the $b\bar{b}$ annihilation channel, where it is shown that at lower masses ($M_{DM} \sim 1$ TeV), the sensitivity decreases rapidly at high energies, indicating a weaker detection capability in this regime. As M_{DM} increases, the sensitivity improves at higher energies due to the harder photon spectrum produced by heavier DM particles. Notably, there is a spectral feature around 1 TeV for large dark matter masses, which may result from hadronization effects in the cascade decay of bottom quarks due the generations of a large number of mesons, which subsequently decay into photons through hadronic cascades.

For the $\tau^-\tau^+$ channel, the shape of the curves is relatively smooth, and sensitivity does not change drastically with M_{DM}. Unlike hadronic channels, the τ-lepton channel directly produces photons through electroweak interactions, leading to a more stable gamma-ray spectrum. The overlap of the sensitivity curves for different DM masses suggests that the detection capability remains similar across a broad mass range.

The W^+W^- channel exhibits a behavior similar to the $b\bar{b}$ channel, where sensitivity improves at high energies as M_{DM} increases. For low masses, sensitivity rapidly declines at high energies, whereas for $M_{DM} = 250$ TeV, the detector maintains better sensitivity across a broader energy range. This pattern reflects the increased energy of secondary photons produced in weak boson decays at higher DM masses.

Next we calculate the accumulated signal counts in each energy bin for the three selected annihilation channels, according to the event energy binning selected within `pyswgo` (Table **4.3**) and compare it with the photon background in order to get the adequate constraints for the calculation of our new cross-sections. This process is shown for the five selected DM masses in Figures 6.12, 6.13 and 6.14 for the three selected annihilation channels.

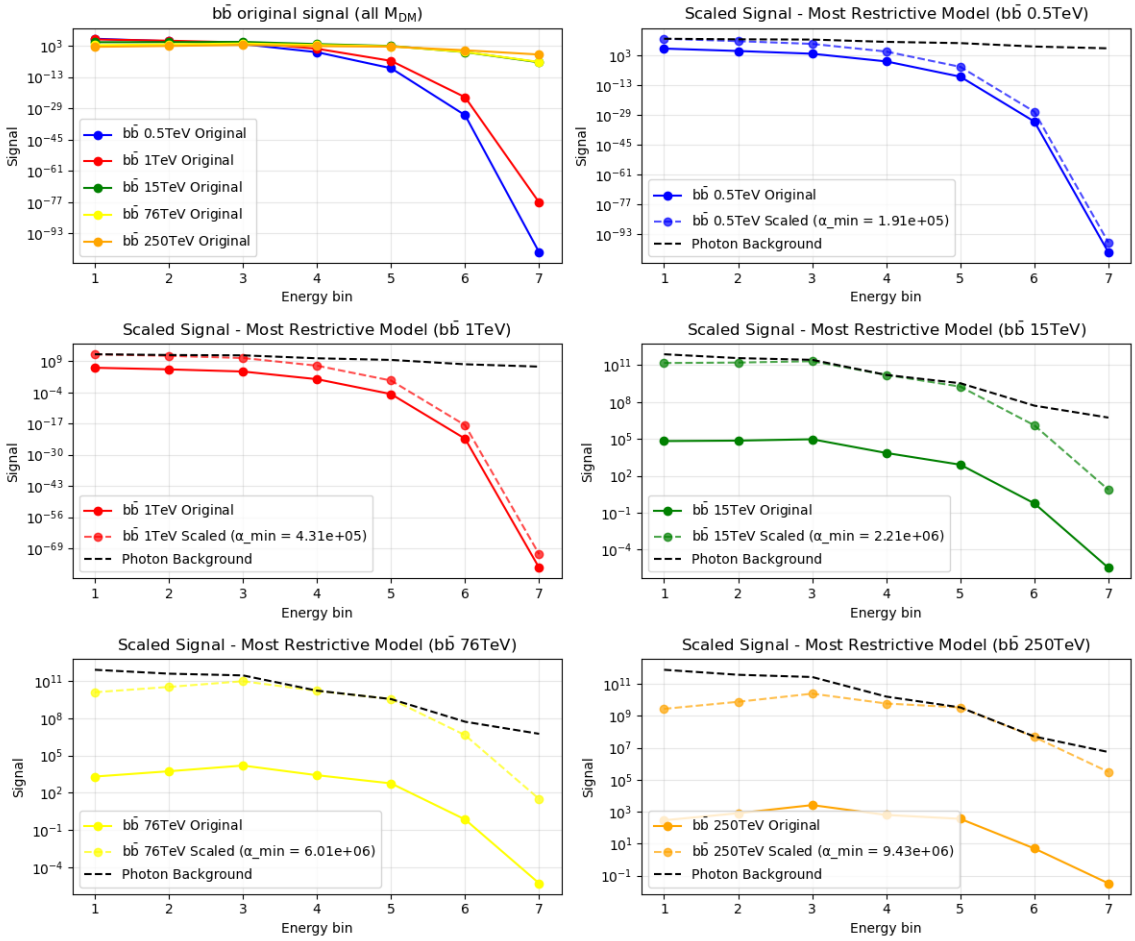

Figure 6.12 – Scaled signal counts for dark matter annihilation into $b\bar{b}$ for different dark matter masses (M_{DM} = 0.5, 1, 15, 76, 250 TeV). The first panel (top-left) presents the original signals, while the other five panels display the scaled signals under the most restrictive model for each of these masses. The photon background is shown as a dashed black line as the reference to scale.

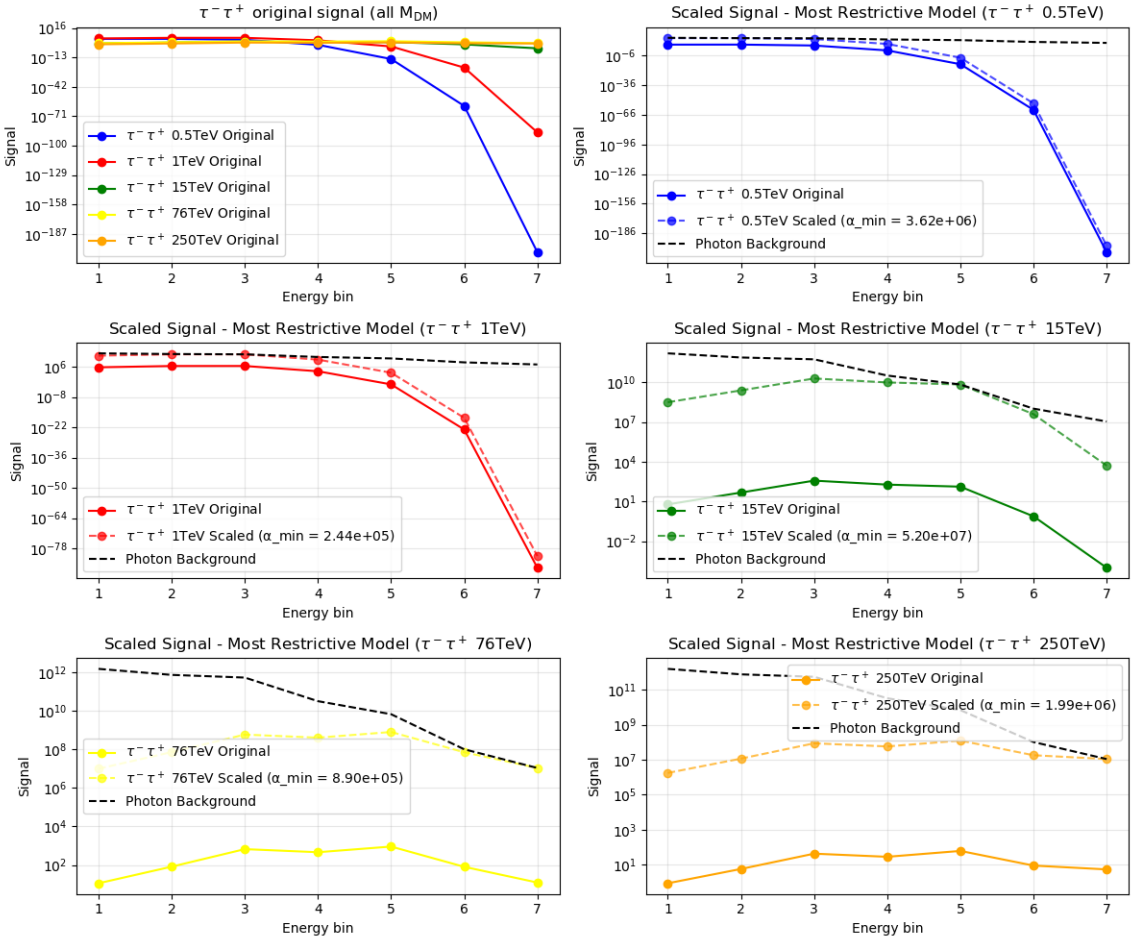

Figure 6.13 – Scaled signal counts for dark matter annihilation into $\tau^-\tau^+$ for different dark matter masses (M_{DM} = 0.5, 1, 15, 76, 250 TeV). The first panel (top-left) presents the original signals, while the other five panels display the scaled signals under the most restrictive model for each of these masses. The photon background is shown as a dashed black line as the reference to scale.

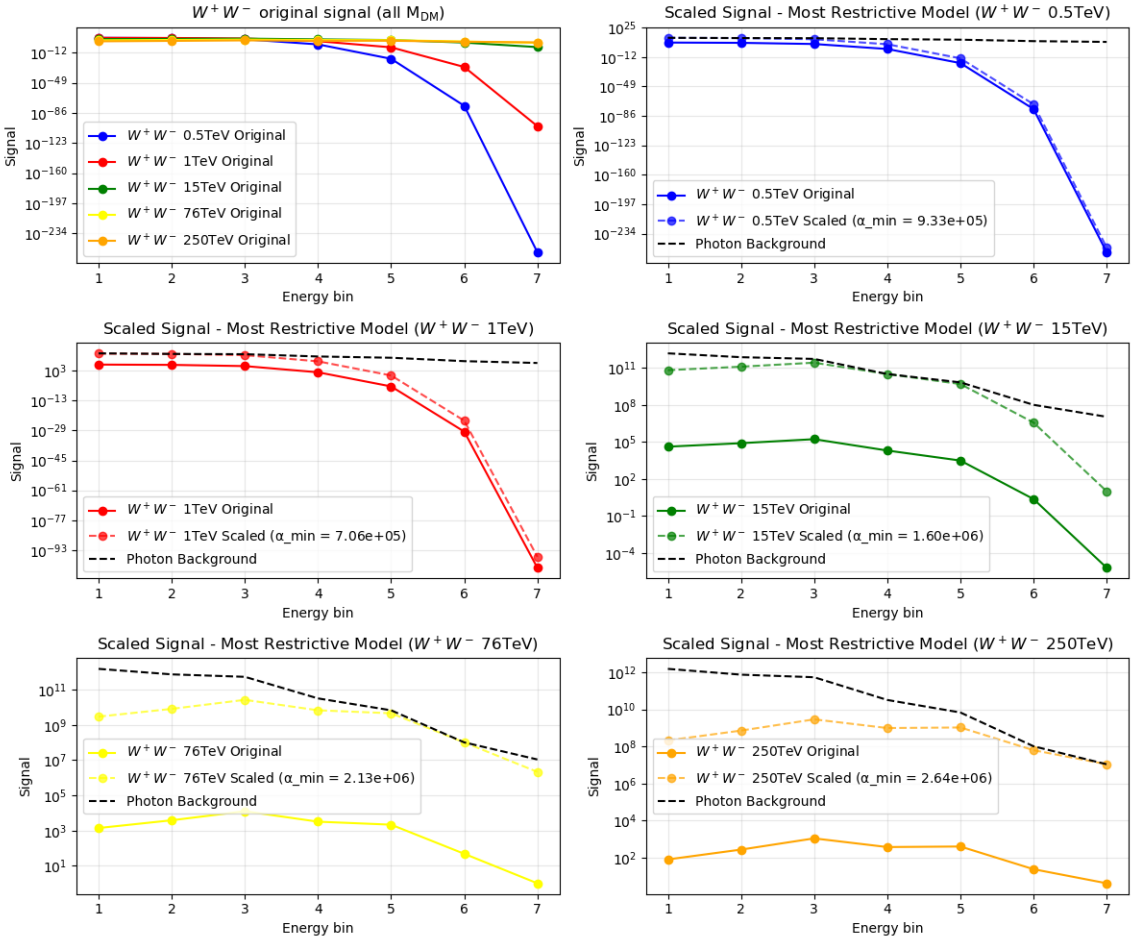

Figure 6.14 – Scaled signal counts for dark matter annihilation into W^+W^- for different dark matter masses (M_{DM} = 0.5, 1, 15, 76, 250 TeV). The first panel (top-left) presents the original signals, while the other five panels display the scaled signals under the most restrictive model for each of these masses. The photon background is shown as a dashed black line as the reference to scale.

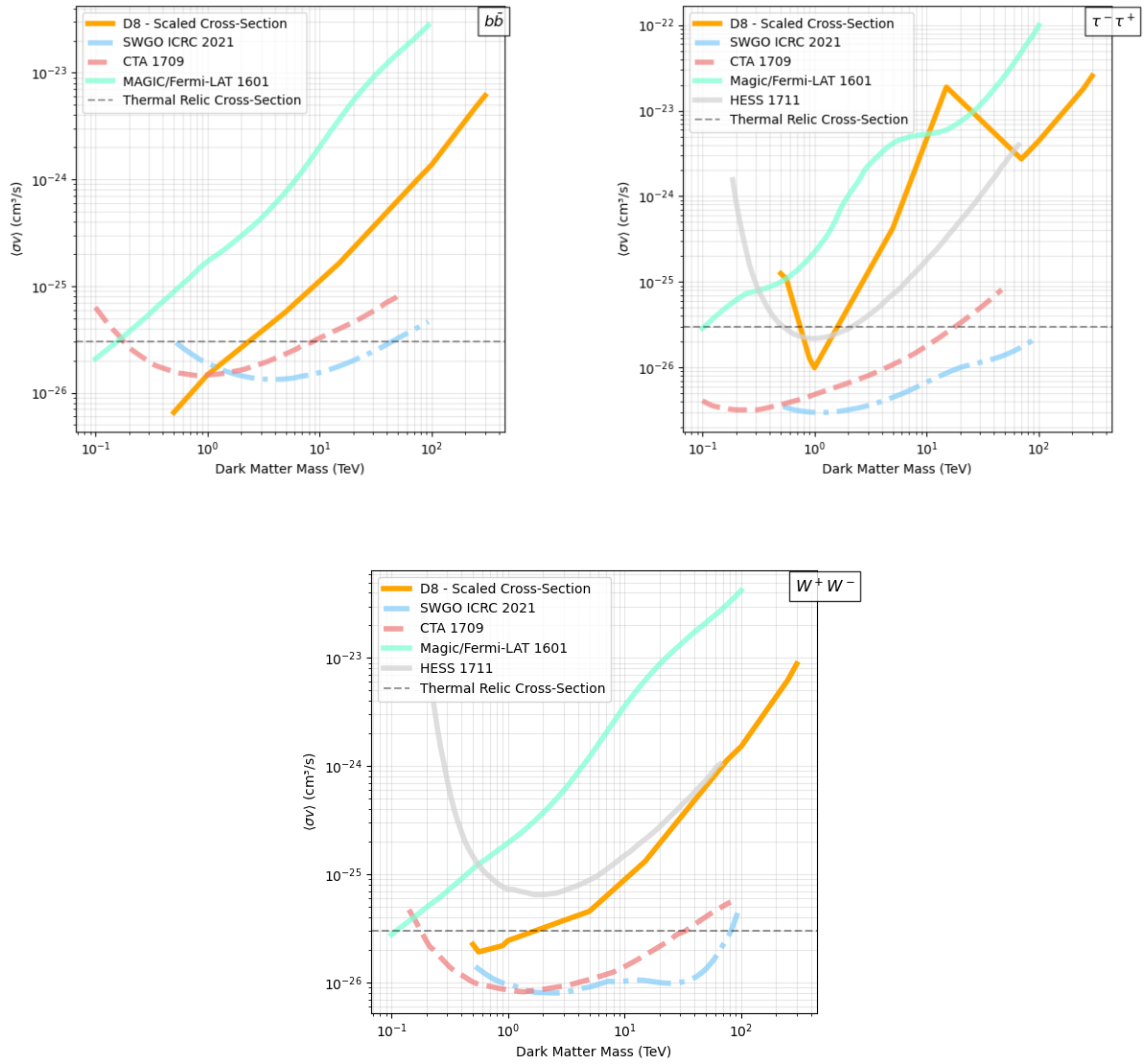

Figure 6.15 – Constraints on the annihilation cross-section $\langle\sigma v\rangle$ for the $b\bar{b}$, $\tau^-\tau^+$ and W^+W^- annihilation channels. The `D8` dataset (orange) is compared to existing and projected limits from MAGIC/Fermi-LAT, HESS, CTA, SWGO, and the thermal relic cross-section.

Figure 6.15 shows the cross-section versus dark matter mass (M_{DM}) and illustrates the projected upper limits on the velocity-weighted annihilation cross-section $\langle\sigma v\rangle$ for the different selected dark matter annihilation channels: $b\bar{b}$, $\tau^-\tau^+$, and W^+W^-. These limits are derived from the previous sensitivity studies and are compared to other existing and proposed experiments, including HESS, CTA, MAGIC/Fermi-LAT, previous SWGO investigations and current thermal relic cross-section constraints.

A key feature in all three plots is the position of our `D8` curve (orange) relative to the thermal relic cross-section (dashed black line). The thermal relic cross-section represents the benchmark value for a Weakly Interacting Massive Particle (WIMP) to be a thermal relic, meaning that if a WIMP candidate lies above this line, its annihilation cross-section is higher than required for standard thermal freeze-out. Conversely, if an experimental sensitivity curve is below this line, it means that the given experiment has the capability to probe cross-sections smaller than the thermal relic value, which is crucial for excluding or detecting sub-thermal relic dark matter candidates.

For the $b\bar{b}$ channel (top-left panel), the `D8` cross-section remains consistently above the thermal relic cross-section, particularly for $M_{DM} \geq 1$ TeV, indicating a higher expected annihilation rate than the standard WIMP relic assumption. Compared to SWGO and CTA, our data (`D8`) exhibits a steeper increase at higher masses, diverging significantly from the sensitivity curves beyond 10 TeV. We can see that our results improves the sensitivity to DM annihilation in almost an order of magnitude with respect to experimental data form MAGIC/Fermi-LAT [63] on the full DM mass range, and we see that below 1 TeV there is a tendency for improvement over previous simulations from CTA [64] and SWGO [65].

In the $\tau^-\tau^+$ channel (top-right panel) our `D8` cross-section shows fluctuations across different mass scales, remaining well above both the thermal relic cross-section and the sensitivity limits of CTA and SWGO. These rapid variations across different masses could arise from spectral modeling effects, which alter the predicted gamma-ray flux used to estimate the sensitivities previously illustrated.

For the W^-W^+ (bottom-panel) annihilation channel at masses below 1 TeV, our simulations are close to the thermal relic cross-section but rapidly increase with mass at around 10 TeV. We observe an improvement in DM sensitivity across the entire mass range compared to the MAGIC/Fermi-LAT [63] data and a similar performance to HESS [66] observations for masses around (~ 100) TeV. Below this point, our simulations yield consistently better limits.

Nonetheless, in the three selected channels, we were not able to reach the values from previous SWGO simulations, likely due to the differences in our initial simulated data, as we aimed to generate a more precise gamma-ray flux compared to the collaboration's simulations. This discrepancy affects how the reconstruction algorithms (previously trained by the collaboration) handle our dataset, particularly in the calculation of the effective area (key component of the sensitivity estimation). While this approach results in worse predictions compared to SWGO and CTA, it could improve the accuracy of these limit estimations.

7 Summary and Conclusions

We performed a sensitivity analysis for the detection of dark matter (DM) gamma-ray signals using the Southern Wide-field Gamma-ray Observatory (SWGO) detector model. The study was based on detailed Monte Carlo simulations of extensive air showers and detector response, aiming to evaluate SWGO ability to detect potential DM annihilation signals from the Galactic Center (GC). Our methodology included simulating particle showers using the CORSIKA package, where the initial conditions were defined by realistic DM gamma-ray spectra generated with PYTHIA for multiple annihilation channels. The detector response was modeled using Geant4-based software, allowing for the reconstruction of key observables such as the event's energy, direction, and primary particle type. From these simulations, we computed the Instrument Response Functions (IRFs), which characterize SWGO's detection capabilities in terms of effective area, angular resolution, energy resolution, background rejection, and sensitivity.

One of the key aspects of our study was the determination of the effective area of the detector, which defines the sensitivity of the array to incoming gamma-ray events.

Our results regarding the IRF estimations show overall agreement with previous SWGO estimates, particularly at lower energies. However, we identified a normalization discrepancy in the effective area, likely caused by our approach of using segmented spectral indices, and different number of events for different energy ranges. This deviation highlights the importance of correctly implementing energy-dependent event weighting in future analyses.

Regarding energy and angular resolution, we verified that the reconstruction of primary particle energy performed with likelihood-based methods yielded reliable results across all core and zenith bins. Our energy resolution closely follows the collaboration's current (preliminary) performance estimates, confirming the applicability of the reconstruction algorithms to our special simulations set. In the case of angular resolution, we observed the expected improvement at higher energies, as showers become more collimated and better reconstructed. However, our resolution was slightly worse than that of previous SWGO simulations, likely due to our extremely limited statistics.

The ability to distinguish gamma-ray signals from the hadronic background is crucial for indirect DM detection. The analysis of gamma/hadron separation and background rejection showed that, while proton rejection efficiency was slightly lower than in the preliminary SWGO studies, it remained within an acceptable range for our analysis. Nevertheless, our results indicate that false-positive rates remained below 10 %, meaning that a significant fraction of gamma-ray events can still be effectively distinguished from cosmic-ray backgrounds.

The sensitivity of SWGO to DM-induced gamma-ray fluxes was evaluated for different annihilation channels, including $b\bar{b}$, $\tau^-\tau^+$, and W^+W^-, across a wide mass range (0.5 – 250 TeV). Our study provides new upper limits on the DM annihilation cross-section $\langle\sigma v\rangle$, improving upon previous constraints set by MAGIC and Fermi-LAT, and in some ranges from HESS. However, we found that our constraints were not as positive as those projected previously for SWGO and CTA. This discrepancy is likely due to differences in event statistics, flux modeling, and the selection cuts applied to reconstructed events.

In conclusion, our results reinforce the potential of SWGO as a leading experiment for DM searches in the Southern Hemisphere in comparison to other experiments. The combination of a wide field of view, continuous all-sky coverage, and high-energy sensitivity positions SWGO as an essential observatory for detecting extended gamma-ray emissions from the GC.

Future studies should first focus on augmenting the number of simulations in order to improve statistics. A better initial fit could also be achieved in order to get a better set of spectral indices for the particle showers simulations. Finally, incorporating alternative DM density profiles, such as Navarro-Frenk-White (NFW) and cored models, would provide a more comprehensive understanding of astrophysical uncertainties in DM distribution.

A Apendix: Gamma-ray spectral index calculation

Here, we present the curves illustrating the complete process to obtain the average spectral index per energy segment, as described in Chapter 5, for all annihilation channels of the Standard Model.

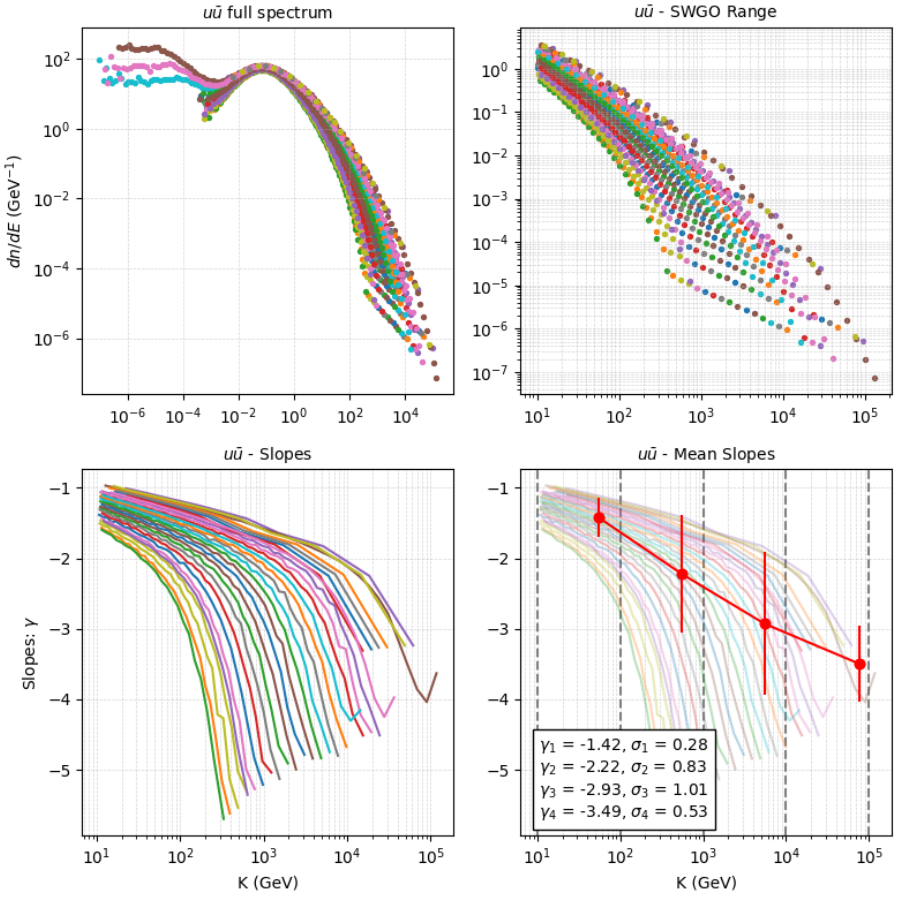

Figure A.1 – Gamma-ray differential spectrum from the $u\bar{u}$ annihilation channel. Full process of the mean slopes calculation.

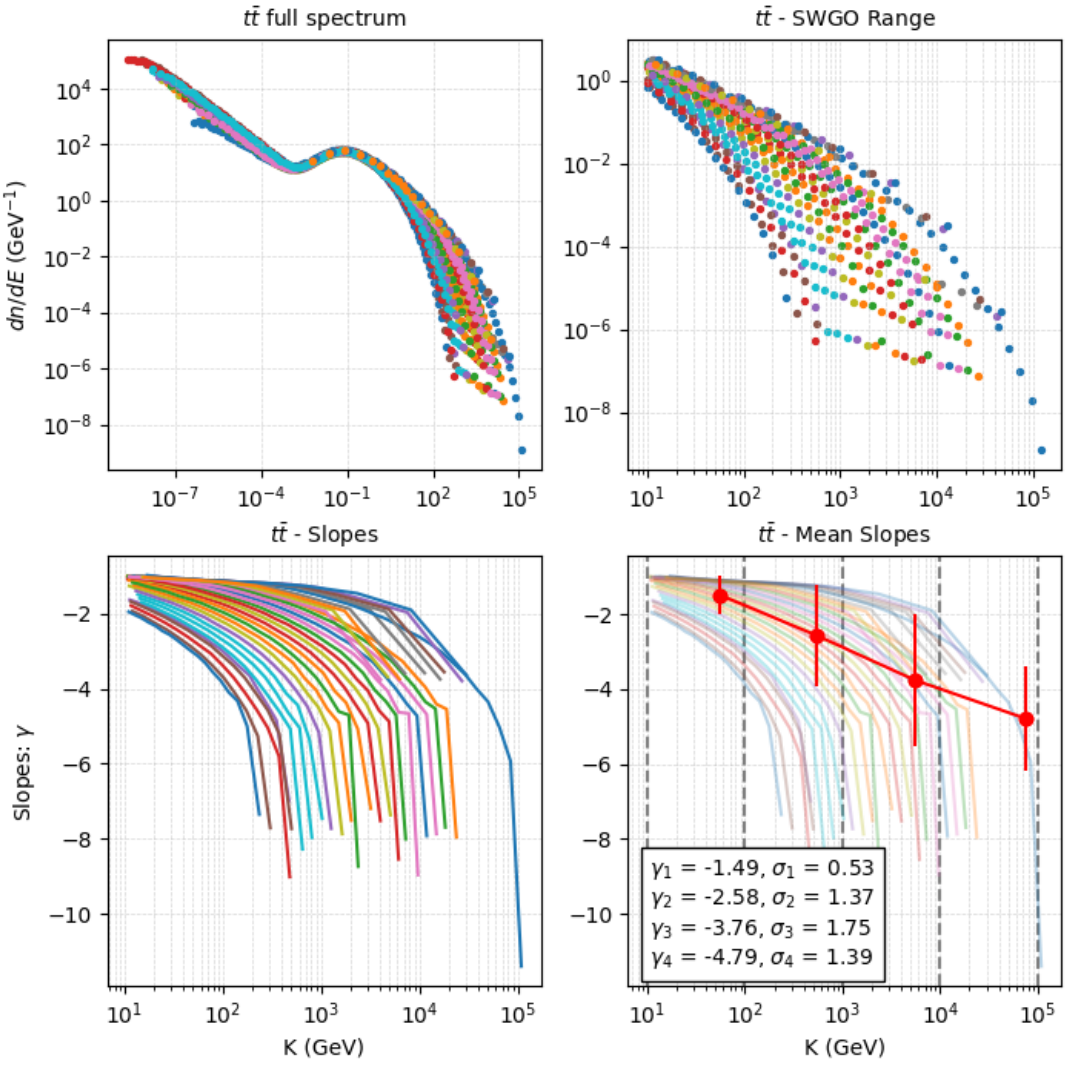

Figure A.2 – Gamma-ray differential spectrum from the $t\bar{t}$ annihilation channel. Full process of the mean slopes calculation.

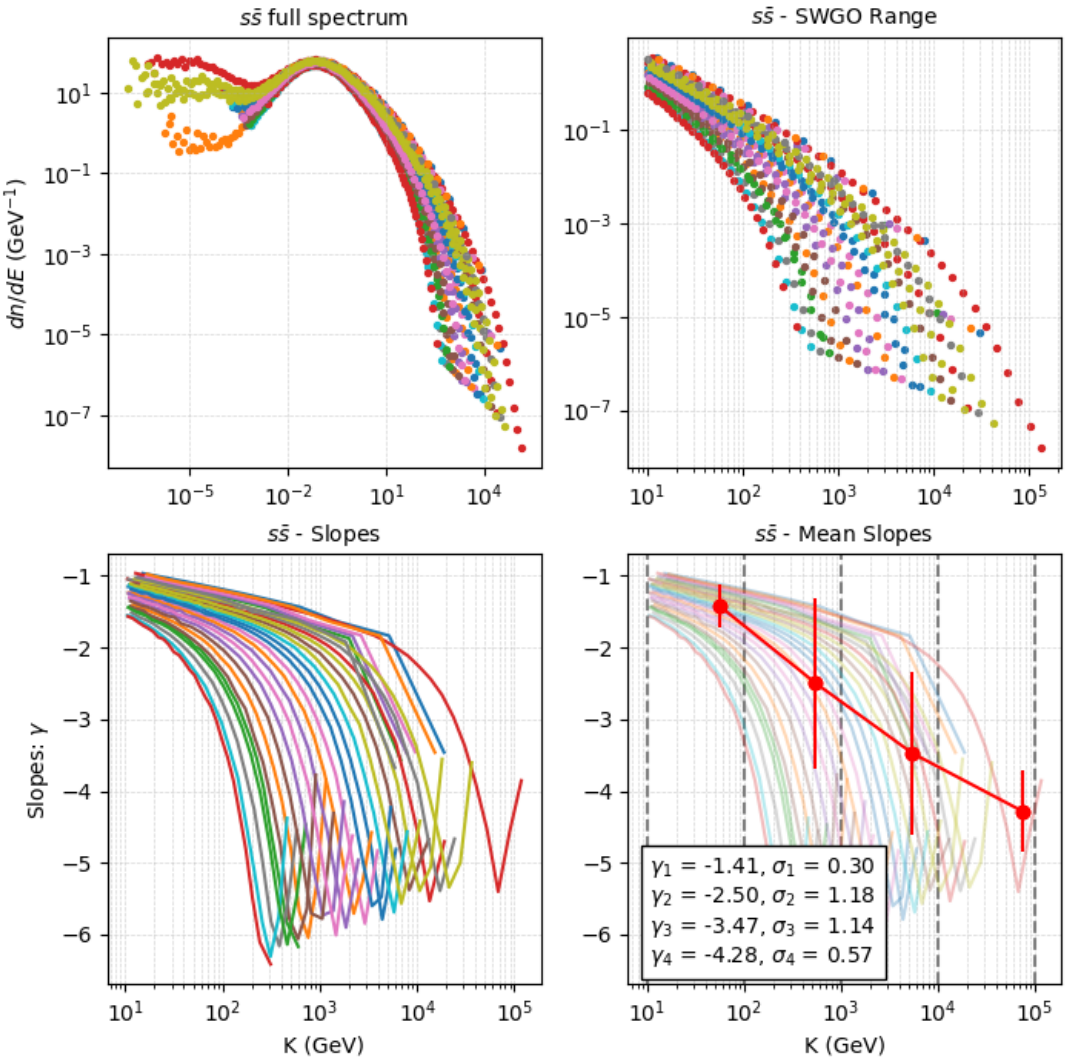

Figure A.3 – Gamma-ray differential spectrum from the $s\bar{s}$ annihilation channel. Full process of the mean slopes calculation.

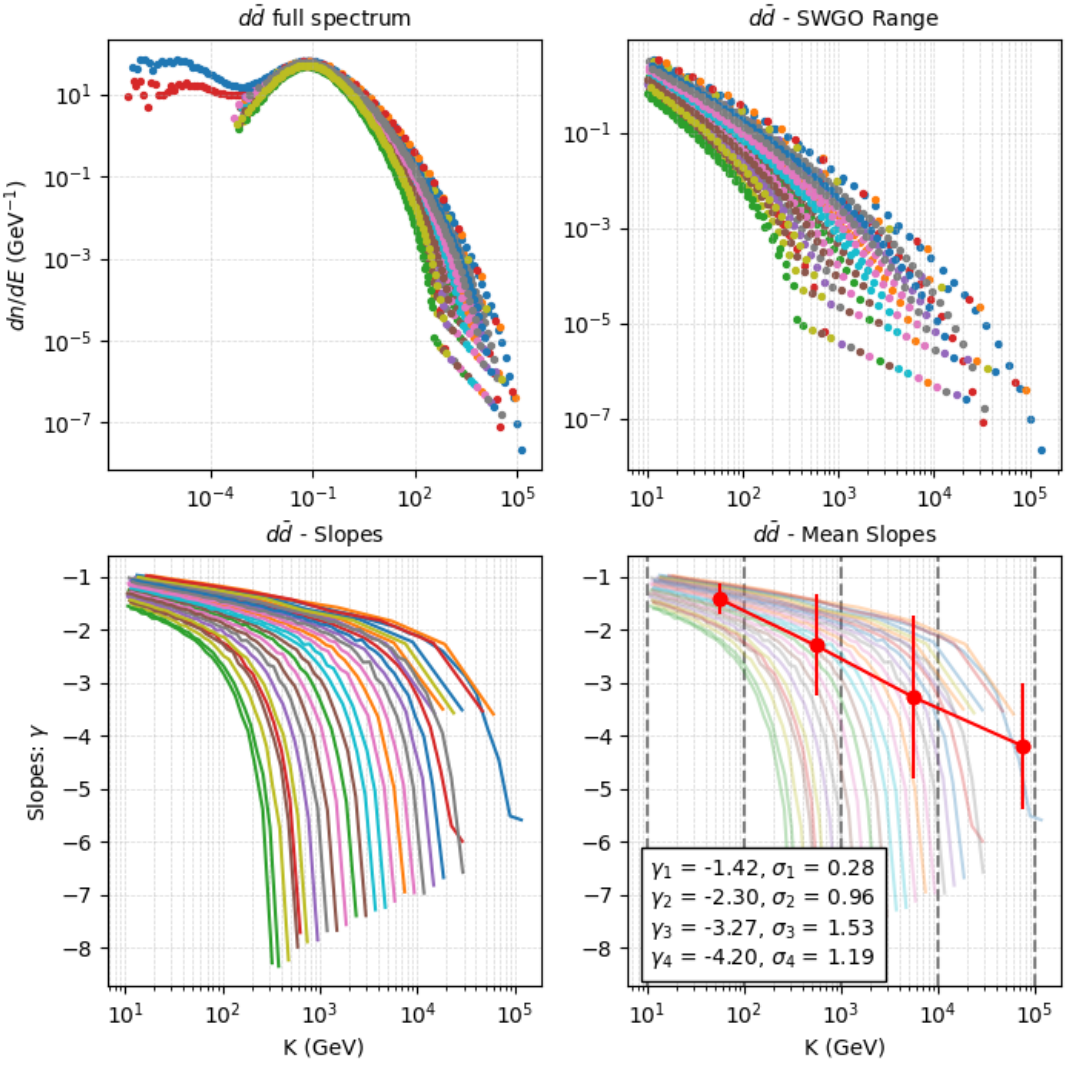

Figure A.4 – Gamma-ray differential spectrum from the $d\bar{d}$ annihilation channel. Full process of the mean slopes calculation.

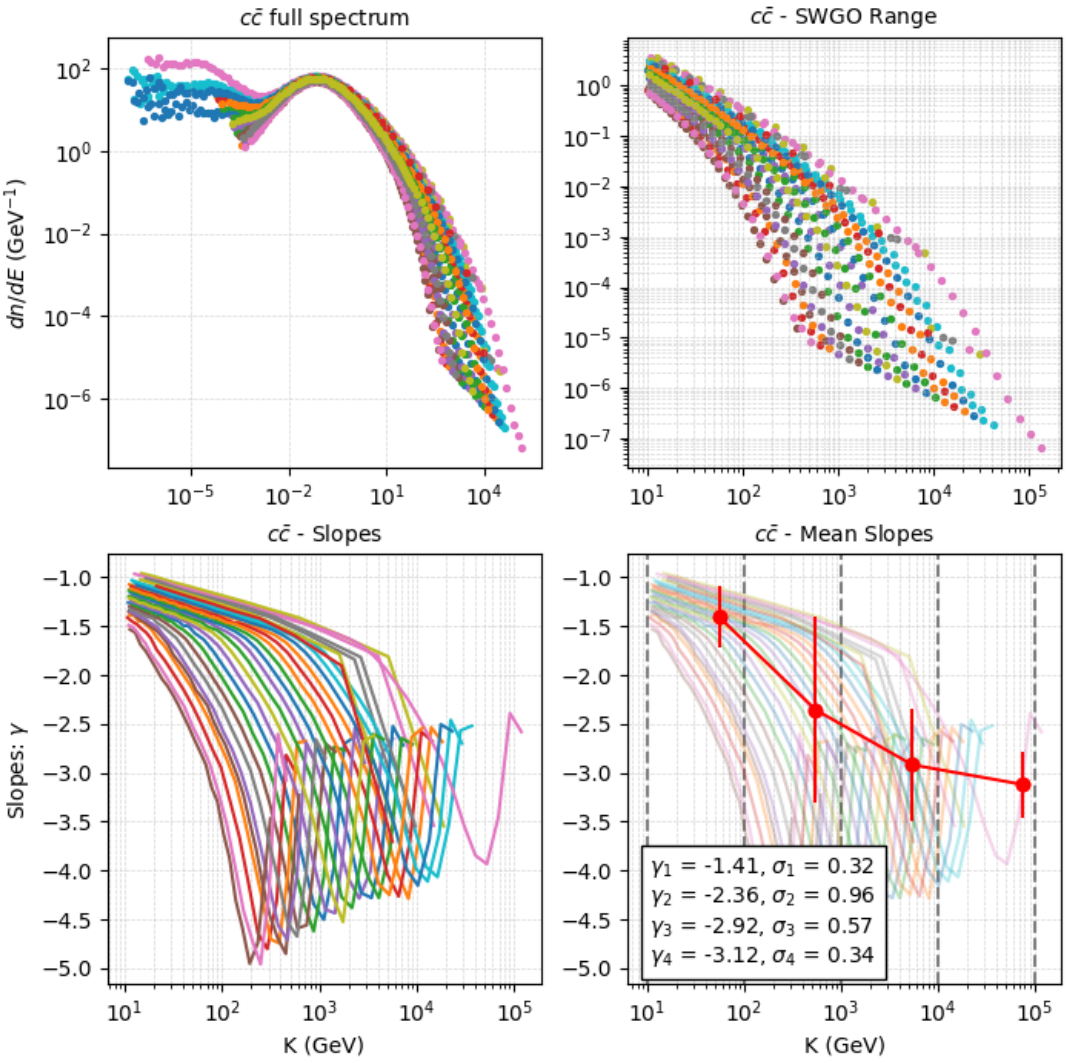

Figure A.5 – Gamma-ray differential spectrum from the $c\bar{c}$ annihilation channel. Full process of the mean slopes calculation.

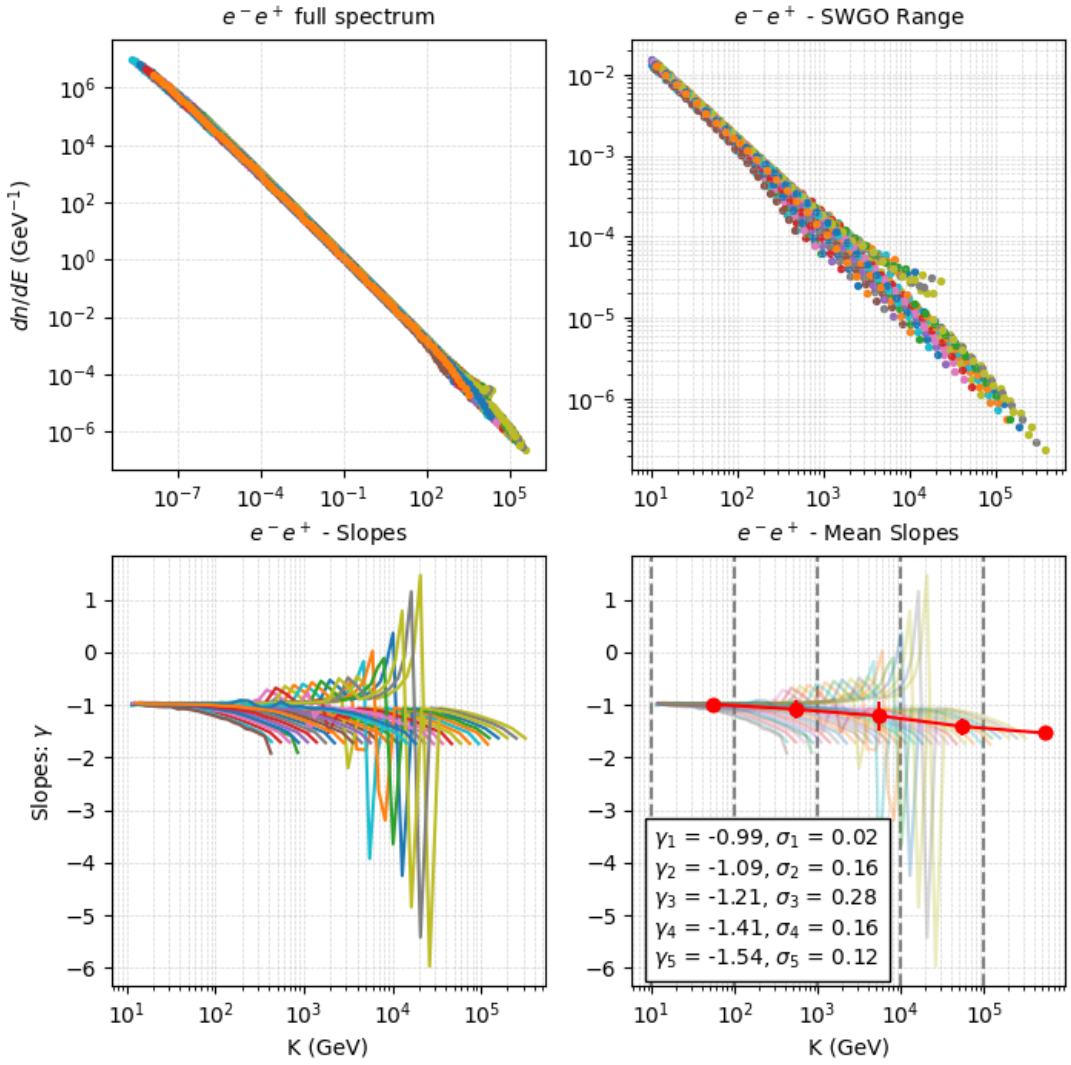

Figure A.6 – Gamma-ray differential spectrum from the e^-e^+ annihilation channel. Full process of the mean slopes calculation.

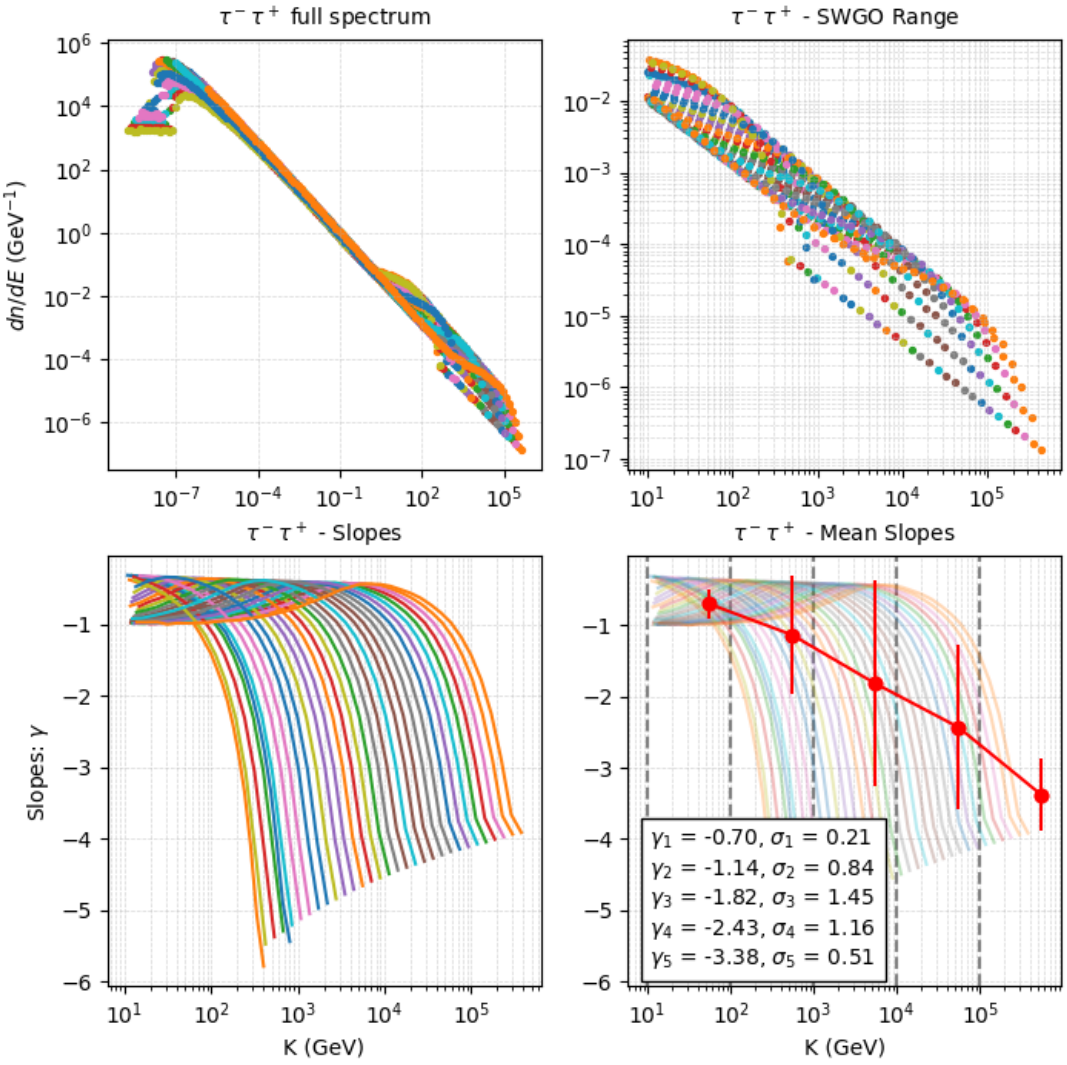

Figure A.7 – Gamma-ray differential spectrum from the $\tau^-\tau^+$ annihilation channel. Full process of the mean slopes calculation.

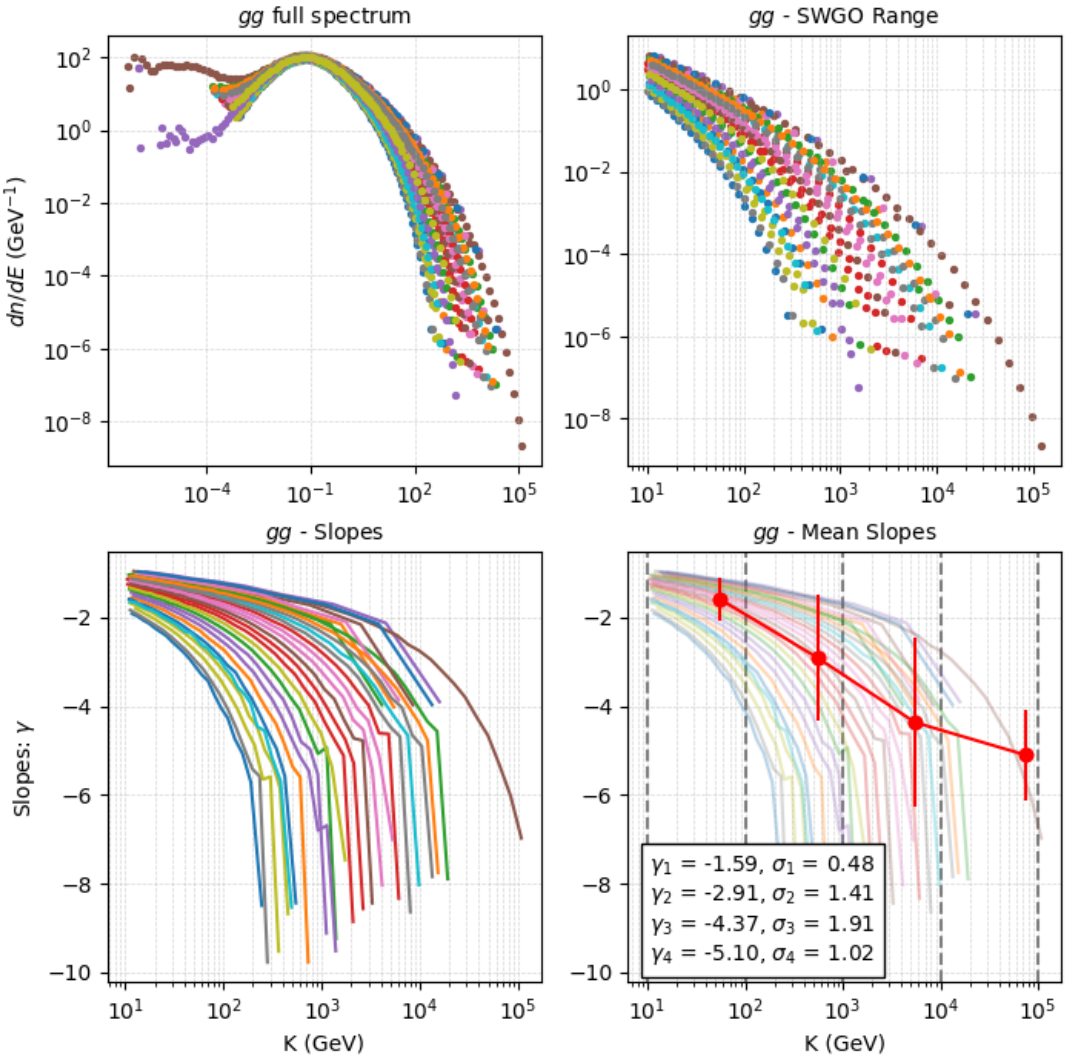

Figure A.8 – Gamma-ray differential spectrum from the $gluon - gluon$ annihilation channel. Full process of the mean slopes calculation.

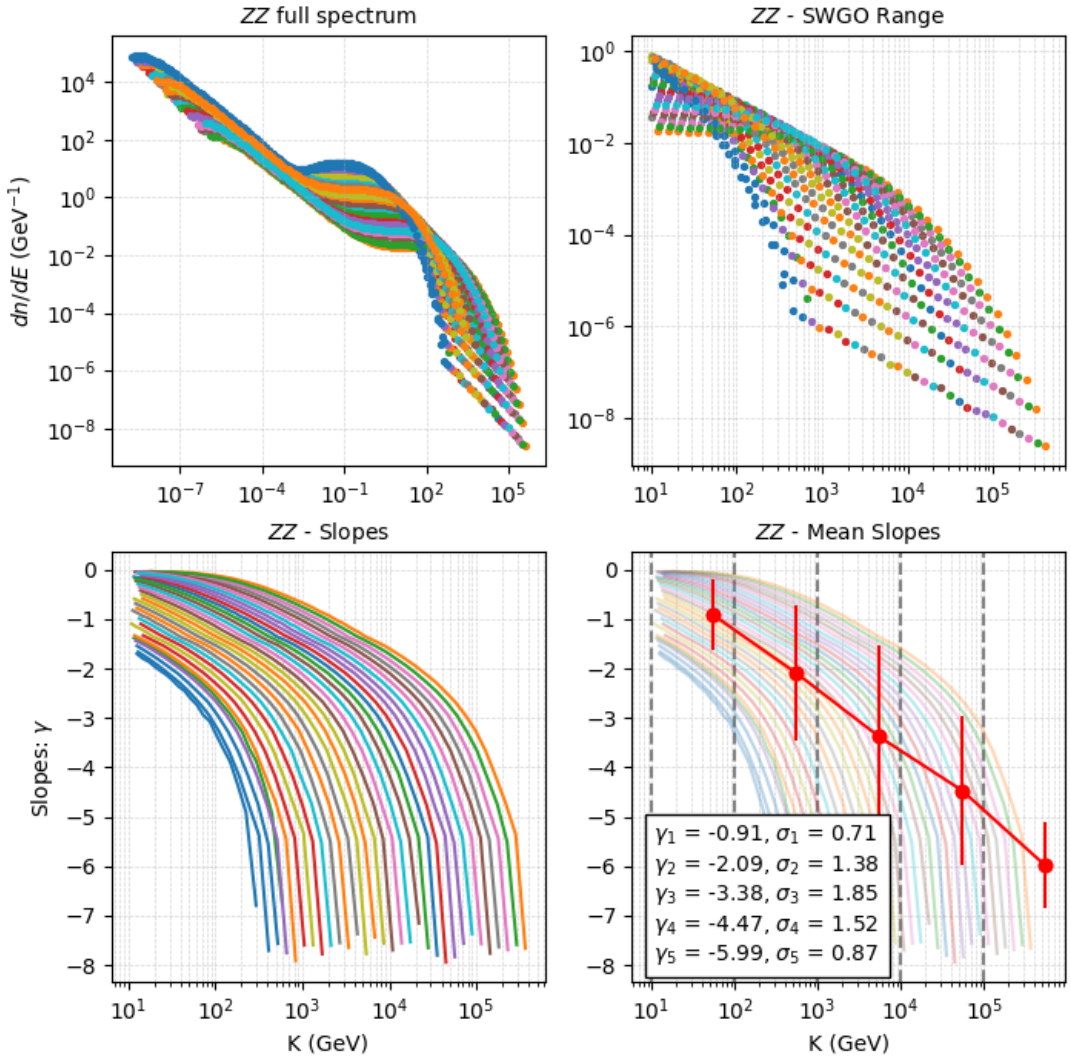

Figure A.9 – Gamma-ray differential spectrum from the ZZ annihilation channel. Full process of the mean slopes calculation.

References

[1] Yoshiaki Sofue and Vera Rubin. Rotation curves of spiral galaxies. *Annual Review of Astronomy and Astrophysics*, 39(1):137–174, September 2001.

[2] Jan Tauber, PAR Ade, N Aghanim, C Armitage Caplan, M Arnaud, M Ashdown, F Atrio Barandela, J Aumont, C Baccigalupi, AJ Banday, et al. Planck 2013 results. xvi. cosmological parameters. *Astronomy & Astrophysics*, 571:A16--A82, 2014.

[3] Jianglai Liu, Xun Chen, and Xiangdong Ji. Current status of direct dark matter detection experiments. *Nature Physics*, 13(3):212--216, 2017.

[4] J Aalbers, DS Akerib, AK Al Musalhi, F Alder, CS Amarasinghe, A Ames, TJ Anderson, N Angelides, HM Araújo, JE Armstrong, et al. First constraints on wimp-nucleon effective field theory couplings in an extended energy region from lux-zeplin. *Physical Review D*, 109(9):092003, 2024.

[5] E Aprile, K Abe, F Agostini, S Ahmed Maouloud, L Althueser, B Andrieu, E Angelino, JR Angevaare, VC Antochi, D Antón Martin, et al. First dark matter search with nuclear recoils from the xenonnt experiment. *Physical review letters*, 131(4):041003, 2023.

[6] ATLAS Collaboration. Status of searches for dark matter at the lhc. *ATL-PHYS-PROC-2022-003*, 2022. Accessed: 2025-02-06.

[7] Georges Aad, Erlend Aakvaag, B Abbott, Kira Abeling, SH Abidi, Asmaa Aboulhorma, Halina Abramowicz, Henso Abreu, Yiming Abulaiti, AC Abusleme Hoffman, et al. Search for dark matter produced in association with a higgs boson decaying to tau leptons at $\sqrt{s} = 13$ tev with the atlas detector. *Journal of High Energy Physics*, 2023(9):1--53, 2023.

[8] Rute Pedro. Searches for dark matter with the atlas detector. *SciPost Physics Proceedings*, (12):048, 2023.

[9] Andrea Albert, Brandon Anderson, Keith Bechtol, Alex Drlica-Wagner, Manuel Meyer, Miguel Sánchez-Conde, L Strigari, M Wood, TMC Abbott, Filipe B Abdalla, et al. Searching for dark matter annihilation in recently discovered milky way satellites with fermi-lat. *The Astrophysical Journal*, 834(2):110, 2017.

[10] A Albert, R Alfaro, C Alvarez, JC Arteaga-Velázquez, D Avila Rojas, HA Ayala Solares, E Belmont-Moreno, KS Caballero-Mora, T Capistrán, A Carramiñana, et al. An optimized search for dark matter in the galactic halo with hawc. *Journal of Cosmology and Astroparticle Physics*, 2023(12):038, 2023.

[11] R Abbasi, M Ackermann, J Adams, SK Agarwalla, JA Aguilar, M Ahlers, JM Alameddine, NM Amin, K Andeen, G Anton, et al. Search for neutrino lines from dark matter annihilation and decay with icecube. *Physical Review D*, 108(10):102004, 2023.

[12] Zhen Cao, D della Volpe, Siming Liu, Xiaojun Bi, Yang Chen, BD'Ettorre Piazzoli, Li Feng, Huanyu Jia, Zhuo Li, Xinhua Ma, et al. The large high altitude air shower observatory (lhaaso) science book (2021 edition). *arXiv preprint arXiv:1905.02773*, 2019.

[13] Francisco Salesa Greus, HAWC collaboration, et al. First results from the hawc gamma-ray observatory. *Nuclear and particle physics proceedings*, 273:289--294, 2016.

[14] Zhen Cao, F Aharonian, Q An, YX Bai, YW Bao, D Bastieri, XJ Bi, YJ Bi, JT Cai, Q Cao, et al. The first lhaaso catalog of gamma-ray sources. *The Astrophysical Journal Supplement Series*, 271(1):25, 2024.

[15] V. F. Hess. Concerning observations of penetrating radiation on seven free balloon flights. *A Source Book in Astronomy and Astrophysics*, 1900–1975:13--20, 1979.

[16] W. Hanlon. Updated cosmic ray spectrum. `https://web.physics.utah.edu/~whanlon/spectrum.html`. Consultado el 3 de diciembre de 2024.

[17] Thomas K Gaisser. Cosmic rays and particle physics. *Comments on Nuclear and Particle Physics*, 11(1):25--39, 1982.

[18] V. Schönfelder. *The Universe in Gamma Rays*. Springer Science & Business Media, March 2013.

[19] William L Kraushaar and George W Clark. Search for primary cosmic gamma rays with the satellite explorer xi. *Physical Review Letters*, 8(3):106, 1962.

[20] WB Atwood, Aous A Abdo, Markus Ackermann, W Althouse, B Anderson, M Axelsson, Luca Baldini, J Ballet, DL Band, Guido Barbiellini, et al. The large area telescope on the fermi gamma-ray space telescope mission. *The Astrophysical Journal*, 697(2):1071, 2009.

[21] Mangu VS Rao and Badanaval Venkata Sreekantan. *Extensive air showers*. World scientific, 1998.

[22] Walter Heitler. *The quantum theory of radiation*. Courier Corporation, 1984.

[23] Bruno Rossi and Kenneth Greisen. Cosmic-ray theory. *Rev. Mod. Phys.*, 13:240--309, Oct 1941.

[24] James Matthews. A heitler model of extensive air showers. *Astroparticle Physics*, 22(5-6):387--397, 2005.

[25] A Fraknoi. The openstax free astronomy textbook and its open education resources hub. In *Astronomical Society of the Pacific Conference Series*, volume 533, page 1, 2022.

[26] Rolf Bühler and Roger Blandford. The surprising crab pulsar and its nebula: a review. *Reports on Progress in Physics*, 77(6):066901, 2014.

[27] AU Abeysekara, A Albert, Romulo Alfaro, C Alvarez, JD Álvarez, JR Angeles Camacho, Roberto Arceo, JC Arteaga-Velázquez, KP Arunbabu, D Avila Rojas, et al. Measurement of the crab nebula spectrum past 100 tev with hawc. *The Astrophysical Journal*, 881(2):134, 2019.

[28] NRAO/AUI/NSF NASA, ESA and G. Dubner (University of Buenos Aires). Crab nebula in multiple wavelengths, 2021. Accessed: 2024-12-11.

[29] Rene A Ong. Very high-energy gamma-ray astronomy. *Physics Reports*, 305(3-4):93--202, 1998.

[30] Claus Grupen, Glen Cowan, Simon Eidelman, and Tilo Stroh. *Astroparticle physics*, volume 50. Springer, 2005.

[31] P.A. Zyla et al. (Particle Data Group). Review of particle physics. *Prog. Theor. Exp. Phys.*, 2020:083C01, 2020.

[32] Antonio Boveia and Caterina Doglioni. Dark matter searches at colliders. *Annual Review of Nuclear and Particle Science*, 68(1):429--459, 2018.

[33] Lidia Pieri, Julien Lavalle, Gianfranco Bertone, and Enzo Branchini. Implications of high-resolution simulations on indirect dark matter searches. *Physical Review D—Particles, Fields, Gravitation, and Cosmology*, 83(2):023518, 2011.

[34] Andreas Burkert. The structure of dark matter halos in dwarf galaxies. *The Astrophysical Journal*, 447(1):L25, 1995.

[35] Marco Cirelli, Gennaro Corcella, Andi Hektor, Gert Hütsi, Mario Kadastik, Paolo Panci, Martti Raidal, Filippo Sala, and Alessandro Strumia. Pppc 4 dm id: a poor particle physicist cookbook for dark matter indirect detection. *Journal of Cosmology and Astroparticle Physics*, 2011(03):051, 2011.

[36] Aea Abramowski, Fabio Acero, F Aharonian, AG Akhperjanian, G Anton, Anna Barnacka, U Barres de Almeida, AR Bazer-Bachi, Yvonne Becherini, J Becker, et al. Search for a dark matter annihilation signal from the galactic center halo with hess. *Physical Review Letters*, 106(16):161301, 2011.

[37] Riccardo Catena and Piero Ullio. A novel determination of the local dark matter density. *Journal of Cosmology and Astroparticle Physics*, 2010(08):004, 2010.

[38] Aion Viana, Harm Schoorlemmer, Andrea Albert, Vitor De Souza, J Patrick Harding, and Jim Hinton. Searching for dark matter in the galactic halo with a wide field of view tev gamma-ray observatory in the southern hemisphere. *Journal of Cosmology and Astroparticle Physics*, 2019(12):061, 2019.

[39] Vikas Joshi. *Reconstruction and analysis of highest energy γ-rays and its application to pulsar wind nebulae*. PhD thesis, 2019.

[40] James Anthony Hinton, Hess Collaboration, et al. The status of the hess project. *New Astronomy Reviews*, 48(5-6):331--337, 2004.

[41] Jamie Holder, RW Atkins, HM Badran, G Blaylock, SM Bradbury, JH Buckley, KL Byrum, DA Carter-Lewis, O Celik, YCK Chow, et al. The first veritas telescope. *Astroparticle Physics*, 25(6):391--401, 2006.

[42] Juan Cortina. Status and first results of the magic telescope. *Astrophysics and Space Science*, 297:245--255, 2005.

[43] Cta Consortium et al. *Science with the Cherenkov Telescope Array*. World Scientific, 2018.

[44] Harm Schoorlemmer. A next-generation ground-based wide field-of-view gamma-ray observatory in the southern hemisphere. *arXiv preprint arXiv:1908.08858*, 2019.

[45] G Aielli, Cesare Bacci, Fabrizio Barone, Bruno Bartoli, Paolo Bernardini, XJ Bi, Carla Bleve, P Branchini, A Budano, S Bussino, et al. Search for gamma ray bursts with the argo-ybj detector in scaler mode. *The Astrophysical Journal*, 699(2):1281, 2009.

[46] SWGO Collaboration. SWGO Wiki, 2024. Accessed: 2024-02-04.

[47] Zigfried Hampel-Arias. *Cosmic Ray Observations at the TeV Scale with the HAWC Observatory*. The University of Wisconsin-Madison, 2017.

[48] Vikas Joshi, Jim Hinton, Harm Schoorlemmer, Rubén López-Coto, and Robert Parsons. A template-based γ-ray reconstruction method for air shower arrays. *Journal of Cosmology and Astroparticle Physics*, 2019(01):012, 2019.

[49] SWGO Collaboration et al. Status of the swgo air shower reconstruction using a template-based likelihood method. *Proceedings of Science*, 444:593, 2024.

[50] R Conceição, L Gibilisco, M Pimenta, and B Tomé. Gamma/hadron discrimination at high energies through the azimuthal fluctuations of air shower particle distributions at the ground. *Journal of Cosmology and Astroparticle Physics*, 2022(10):086, 2022.

[51] Kenneth Greisen. Cosmic ray showers. *Ann. Rev. Nuclear Sci.*, 10, 1960.

[52] CORSIKA Collaboration. CORSIKA: A Monte Carlo Code to Simulate Extensive Air Showers, 2024. Accessed: 2024-02-04.

[53] Sea Agostinelli, John Allison, K al Amako, John Apostolakis, Henrique Araujo, Pedro Arce, Makoto Asai, D Axen, Swagato Banerjee, GJNI Barrand, et al. Geant4—a simulation toolkit. *Nuclear instruments and methods in physics research section A: Accelerators, Spectrometers, Detectors and Associated Equipment*, 506(3):250--303, 2003.

[54] Dieter Heck, Johannes Knapp, JN Capdevielle, G Schatz, T Thouw, et al. Corsika: A monte carlo code to simulate extensive air showers. 1998.

[55] HO Klages, WD Apel, K Bekk, E Bollmann, H Bozdog, IM Brancus, M Brendle, A Chilingarian, K Daumiller, P Doll, et al. The kascade experiment. *Nuclear Physics B-Proceedings Supplements*, 52(3):92--102, 1997.

[56] Sergey Ostapchenko. Monte carlo treatment of hadronic interactions in enhanced pomeron scheme: Qgsjet-ii model. *Physical Review D—Particles, Fields, Gravitation, and Cosmology*, 83(1):014018, 2011.

[57] M Bleicher, E Zabrodin, C Spieles, S A Bass, C Ernst, S Soff, L Bravina, M Belkacem, H Weber, H Stöcker, and W Greiner. Relativistic hadron-hadron collisions in the ultra-relativistic quantum molecular dynamics model. *Journal of Physics G: Nuclear and Particle Physics*, 25(9):1859, sep 1999.

[58] Ian James Watson, A Albert, R Alfaro, C Alvarez, A Andrés, JC Arteaga-Velázquez, D Avila Rojas, HA Ayala Solares, R Babu, E Belmont-Moreno, et al. Deep learning for the hawc observatory. *Proceedings of Science*, 444, 2024.

[59] Andrea Albert, R Alfaro, H Ashkar, C Alvarez, J Álvarez, JC Arteaga-Velázquez, HA Solares, R Arceo, JA Bellido, S BenZvi, et al. Science case for a wide field-of-view very-high-energy gamma-ray observatory in the southern hemisphere. *arXiv preprint arXiv:1902.08429*, 2019.

[60] Torbjörn Sjöstrand, Stephen Mrenna, and Peter Skands. A brief introduction to pythia 8.1. *Computer Physics Communications*, 178(11):852--867, 2008.

[61] Jean-Francois Fortin, Jessie Shelton, Scott Thomas, and Yue Zhao. Gamma Ray Spectra from Dark Matter Annihilation and Decay. 8 2009.

[62] SWGO Collaboration. SWGO Internal Document 2235_07, 2024. Internal document, accessed: 2024-02-04.

[63] Max Ludwig Ahnen, Stefano Ansoldi, LA Antonelli, P Antoranz, A Babic, B Banerjee, P Bangale, U Barres De Almeida, JA Barrio, J Becerra Gonzalez, et al. Limits to dark matter annihilation cross-section from a combined analysis of magic and fermi-lat observations of dwarf satellite galaxies. *arXiv preprint arXiv:1601.06590*, 2016.

[64] B. S. Acharya et al. *Science with the Cherenkov Telescope Array*. WSP, 11 2018.

[65] Jim Hinton. The southern wide-field gamma-ray observatory: Status and prospects, 2021.

[66] Lucia Rinchiuso and E. Moulin. Dark matter searches toward the Galactic Centre halo with H.E.S.S. In *52nd Rencontres de Moriond on Very High Energy Phenomena in the Universe*, pages 255--262, 2017.